The Dissertation Committee for In Tai Kim
certifies that this is the approved version of the following dissertation:

Hydrodynamic Instabilities of Radiative Blast Waves

Committee:

Todd Ditmire, Supervisor

Roger Bengtson

Bjorn Manuel Hegelich

Mike Downer

J. Craig Wheeler

Hydrodynamic Instabilities of Radiative Blast Waves

by

In Tai Kim, B.A.

DISSERTATION

Presented to the Faculty of the Graduate School of

The University of Texas at Austin

in Partial Fulfillment

of the Requirements

for the Degree of

DOCTOR OF PHILOSOPHY

THE UNIVERSITY OF TEXAS AT AUSTIN

December 2013

Dedicated to my parents.

Acknowledgments

I wish to thank all the people who have helped me through the years of graduate school.

I am grateful to all the colleagues whom I've had the previlege of working with. Hernan Quevedo, Woosuk Bang, Matt McCormick, Sam Feldman, Kristina Serratto, Joel Blakeney, Franki Aymond, Aaron Bernstein, and Gilliss Dyer were all instrumental in my work. I also thank Professor Roger Bengtson who have mentored me at times.

I am grateful to my parents whose love and support helped me endure the many years of my education. I thank my brother for all the encouragement he has given me throughout these years. My friends in Austin have made these years memorable and I am grateful for them: Isaac, Hao, Sunny, Linda, C. J., James, Kevin, and Gieun.

Finally, I owe a debt of gratitude to my graduate adviser Todd Ditmire without whom this work would not have been possible.

Hydrodynamic Instabilities of Radiative Blast Waves

Publication No. _____

In Tai Kim, Ph.D.
The University of Texas at Austin, 2013

Supervisor: Todd Ditmire

We present the results from a series of experimental investigations into the hydrodynamic instabilities that occur in radiative blast waves. In particular, we examine the Vishniac instability in which the perturbation modes oscillate in time and, for certain mode numbers and polytropic index of the medium, can exhibit a growth in their amplitudes. Experiments were conducted on the GHOST laser laboratory in which a source of atomic clusters was irradiated by a 1J-2J, 115fs laser pulse to produce cylindrical blast waves. The thrust of this thesis falls into two categories. First, we analyze the effects radiative cooling has on the evolution of blast waves such as the lowering of the effective polytropic index and consequently the lowering of their deceleration parameter. Radiation from the blast wave surface results in a preheated ionization precursor in the upstream material and is indicated by a gradual decline in the electron density profile of the blast wave rather than a sharp jump. This mechanism, if strong enough, can also create a secondary shock wave to form ahead of the main blast wave. The second set of experiments

investigates the temporal evolution of longitudinal perturbations induced on the blast waves by use of a transverse interferometric beam that modifies the cluster medium prior to the onset of the main pump beam. These perturbations are analyzed and compared to theory set forth in Vishniac's mechanism for oscillatory instabilities and their growth rate.

Table of Contents

List of Tables

List of Figures

Chapter 1

Introduction

1.1 Laboratory Astrophysics

Astronomical observations by land or space-based telescopes have been the primary methods by which man was able to study the stars. These telescopes have greatly improved in the last century. Some utilize different regions of the electromagnetic spectrum like the Very Large Array in New Mexico which detects radio waves, and others have reduced or eliminated the atmospheric effects that plague so many land-based ones such as the Hubble Space Telescope. Improvements are still being made and the precision of these instruments continue to grow. Computer-aided simulations have also added to our understanding, providing more insight into observations and theory. However, these methods still have their limits. Telescopes rely on light that reach the earth from billions of light-years away. The applicability of such observations are limited to the conditions that were present at the source billions of years ago. Despite the precision and sophistication of these instruments the observations are often very faint to begin with because of the great distances involved. Computer simulations suffer from the need to validate and verify the results from these observations.

High intensity lasers bridged the gap between astrophysical observations and theoretical models. These lasers can be used to produce high energy density plasmas in the laboratory that resemble astrophysical objects such as the interior of stars. Takabe et al.[1] conducted a survey of the science that can be achieved with high intensity lasers and its applicability in astrophysical research. He proposed that high energy density and high temperature plasmas produced using these lasers can be of interest to astrophysics provided that the following criteria are met: sameness of physics, similarity of physics, and resemblance of physics. The first requires that the physical states produced in the laboratory are the same as astrophysical objects such as the same temperature and density. The second requires that the physics, mainly the hydrodynamics, of the astrophysical phenomena can be scaled down to the laboratory. Ryutov et al.[2] elaborated on this condition an showed that hydrodynamic parameters in astrophysical objects can be scaled down to laboratory regimes to simulate certain astrophysical phenomenon, notably radiative supernova remnants (SNRs). The last criteria states that in the case a scaling law is not found, the physics resemble each other.

High intensity lasers can produce high Mach number shock waves in the laboratory and many experiments in this field have been concentrated on the overall evolution of radiative blast waves. Shocks from SNR's are subject to various hydrodynamic instabilities in the initial stages, such as Rayleigh-Taylor and Richtmeyer-Meshkov instabilities. Vishniac et al.[23] developed a theory that models the behavior of late time instabilities as the shock from an

exploding star propagates into the interstellar medium. In this mechanism, Vishniac showed that the amplitude for certain wavelengths of a perturbed shock propagating in a polytropic gas can exhibit growth. Known as the Vishniac overstability, it is this particular instability that forms the crux of this thesis.

1.2 High Intensity Lasers

Advancements in laser science offered a new set of experimental conditions that can be explored in the laboratory. The development of chirped pulse amplification (CPA) [3] allowed for high intensities and femtosecond-range pulses to be achieved (10^{17} W/m^2) and made accessible extreme and exotic states of matter that are only present in such conditions. Indeed, the field of high energy density science (energy densities (pressures) on the order of Mbars) was built in large part to lasers and CPA technology [4].

With the ability to achieve such high intensities and energy densities, these lasers were now capable of experiments relevant to astrophysics, namely simulating supernova remnant studies. Some of the early experimental investigations of radiative blast waves were performed by Grun et al. [25]. In these experiments, a high intensity laser pulse was fired on to a solid target immersed in a gas of a given polytropic index to produce spherical blast waves. The time evolution of the resulting blast wave instabilities that occurred in more radiative high Z gases were investigated. Edens et al.[27, 28] conducted similar experiments at Sandia National Laboratories and expanded further on

the evolution of instabilities in a controlled manner by inducing specific perturbations on the blast wave. This was achieved by use of a wire array placed in the path of the propagating blast wave. The array spacing and it's location respective to the blast wave origin determined the mode number (perturbation wavelength).

This thesis describes experiments conducted at the University of Texas at Austin to quantitatively investigate the hydrodynamic instabilities associated with the Vishniac mechanism in cylindrical blast waves using a gas of atomic clusters. The laser system used in our investigation of radiative blast waves are terawatt CPA systems with $\sim$1-2 J of energy on target.

Chapter 2

Shock Waves

2.1 Fluid Equations and Sound Waves

A fluid in motion can be described in terms of its velocity, density, and pressure as a function of position and time [5]. The total time rate of change of any quantity of a fluid parcel with velocity $\mathbf{u}$ is [6]

$$\frac{d}{dt} = \frac{\partial}{\partial t} + \mathbf{u} \cdot \nabla, \tag{2.1}$$

and is often called the convective time derivative. We can express the conservation of mass of a given volume element by the net change in the density resulting from the flow of fluid into or out of that given element as

$$\frac{d\rho}{dt} + \rho \nabla \cdot \mathbf{u} = 0, \tag{2.2}$$

where ρ is the fluid density and $\mathbf{u}$ is the fluid velocity. Any change in the momentum of the fluid parcel is due to a pressure gradient (absent other external forces) and is

$$\rho \frac{d\mathbf{u}}{dt} = -\nabla P. \tag{2.3}$$

Using Eqn. (2.1), these can be rewritten as

$$\frac{\partial \rho}{\partial t} + \nabla \cdot (\rho \mathbf{u}) = 0, \tag{2.4}$$

and

$$\frac{\partial \mathbf{u}}{\partial t} + \mathbf{u} \cdot \nabla \mathbf{u} = -\frac{1}{\rho} \nabla P. \tag{2.5}$$

Eq.(2.4) and Eq.(2.5) are referred to as the continuity equation and Euler's equation, respectively. From these equations, we can derive the velocity of small disturbances in a fluid medium. Consider small fluctuations in the thermodynamic variables density $\Delta\rho$, pressure ΔP, temperature ΔT, and entropy Δs from their average equilibrium values ρ_0, P_0, T_0, and s_0 of a fluid at rest (or one in which the average equilibrium velocity is zero):

$$\begin{aligned} \rho(\mathbf{r}, t) &= \rho_0 + \Delta\rho(\mathbf{r}, t) \\ P(\mathbf{r}, t) &= P_0 + \Delta P(\mathbf{r}, t) \\ T(\mathbf{r}, t) &= T_0 + \Delta T(\mathbf{r}, t) \\ s(\mathbf{r}, t) &= s_0 + \Delta s(\mathbf{r}, t) \\ \mathbf{u}(\mathbf{r}, \mathbf{t}) &= \Delta\mathbf{u}(\mathbf{r}, \mathbf{t}). \end{aligned} \tag{2.6}$$

Inserting these into the fluid equations and keeping only the linear terms yields

$$\frac{\partial \Delta\rho}{\partial t} = -\rho_0 \nabla \cdot \mathbf{u} \tag{2.7}$$

from the continuity equation and

$$\rho_0 \frac{\partial \mathbf{u}}{\partial t} = -\nabla(\Delta P) \tag{2.8}$$

from Euler's equation. Note that in Eq.(2.8) $\nabla P = \nabla(P_0 + \Delta P(\mathbf{r}, t)) = \nabla(\Delta P(\mathbf{r}, t))$. Lastly, we have an expression for the entropy current as

$$\rho_0 \frac{\partial \Delta s}{\partial t} = \frac{K}{T_0} \nabla^2 \Delta T \tag{2.9}$$

where K is the coefficient of thermal conductivity [6]. Together, Equations (2.7)-(2.9) are collectively known as the Navier-Stokes equations. Lets consider Equations (2.7) to (2.9) in the simple one dimensional planar case for an ideal fluid in which $K = 0$. Then these become

$$\frac{\partial \Delta\rho}{\partial t} + \rho_0 \frac{\partial u}{\partial x} = 0, \tag{2.10}$$

$$\rho_0 \frac{\partial u}{\partial t} + \frac{\partial \Delta P}{\partial x} = 0, \tag{2.11}$$

and

$$\rho_0 \frac{\partial \Delta s}{\partial t} = 0. \tag{2.12}$$

Since $\Delta\rho$, ΔP, ΔT, and Δs are related to each other by thermodynamic equations, we can treat them as exact differentials and choose two of them to be independent allowing us to expand the other two in terms of them (see Ref. [6]). Let us choose $\Delta\rho$ and ΔT to be independent and expand ΔP and Δs in terms of these two(reichl):

$$\Delta P(\mathbf{r}, t) = \left(\frac{\partial P}{\partial \rho}\right)_T \Delta\rho(\mathbf{r}, t) + \left(\frac{\partial P}{\partial T}\right)_\rho \Delta T(\mathbf{r}, t) \tag{2.13}$$

and

$$\Delta s(\mathbf{r}, t) = \left(\frac{\partial s}{\partial \rho}\right)_T \Delta\rho(\mathbf{r}, t) + \left(\frac{\partial s}{\partial T}\right)_\rho \Delta T(\mathbf{r}, t). \tag{2.14}$$

We can insert equations (2.13) and (2.14) into equations (2.11) and (2.12), respectively, to obtain

$$\rho_0 \frac{\partial u}{\partial t} = -\left(\frac{\partial P}{\partial \rho}\right)_T \frac{\partial \Delta\rho}{\partial x} - \left(\frac{\partial P}{\partial T}\right)_\rho \frac{\partial \Delta T}{\partial x} \tag{2.15}$$

and

$$\rho_0 \left(\frac{\partial s}{\partial \rho}\right)_T \frac{\partial \Delta\rho}{\partial t} + \rho_0 \left(\frac{\partial s}{\partial T}\right)_\rho \frac{\partial \Delta T}{\partial t} = 0. \tag{2.16}$$

It is more useful to rearrange Eq. (2.16) with ΔT on one side to obtain

$$\begin{aligned} \frac{\partial \Delta T}{\partial t} &= -\left(\frac{\partial T}{\partial s}\right)_\rho \left(\frac{\partial s}{\partial \rho}\right)_T \frac{\partial \Delta\rho}{\partial t} \\ &= \left(\frac{\partial T}{\partial \rho}\right)_s \frac{\partial \Delta\rho}{\partial t}, \end{aligned} \tag{2.17}$$

where we use the relations

$$\left(\frac{\partial x}{\partial y}\right)_z = \frac{1}{\left(\frac{\partial y}{\partial x}\right)_z} \tag{2.18}$$

and

$$\left(\frac{\partial x}{\partial y}\right)_z \left(\frac{\partial y}{\partial z}\right)_x \left(\frac{\partial z}{\partial x}\right)_y = -1. \tag{2.19}$$

Next, we take the time derivative of Eq. (2.15) and substitute in Eq. (2.10) and Eq. (2.17) to obtain

$$\begin{aligned} \rho_0 \frac{\partial^2 u}{\partial t^2} &= -\left(\frac{\partial P}{\partial \rho}\right)_T \frac{\partial}{\partial x}\frac{\partial \Delta\rho}{\partial t} - \left(\frac{\partial P}{\partial T}\right)_\rho \frac{\partial}{\partial x}\frac{\partial \Delta T}{\partial t} \\ &= -\left(\frac{\partial P}{\partial \rho}\right)_T \frac{\partial}{\partial x}\left[-\rho_0 \frac{\partial u}{\partial x}\right] - \left(\frac{\partial P}{\partial T}\right)_\rho \left(\frac{\partial T}{\partial \rho}\right)_s \frac{\partial}{\partial x}\left[-\rho_0 \frac{\partial u}{\partial x}\right] \\ &= \rho_0 \left[\left(\frac{\partial P}{\partial \rho}\right)_T + \left(\frac{\partial P}{\partial T}\right)_\rho \left(\frac{\partial T}{\partial \rho}\right)_s\right] \frac{\partial^2 u}{\partial x^2} \end{aligned} \tag{2.20}$$

Lastly, we use the relation

$$\left(\frac{\partial x}{\partial y}\right)_z = \left(\frac{\partial x}{\partial y}\right)_w + \left(\frac{\partial x}{\partial w}\right)_y \left(\frac{\partial w}{\partial y}\right)_z \tag{2.21}$$

to express the terms inside the brackets in Eq. (2.20) as $(\partial P/\partial \rho)_s$ and arrive at our final result of

$$\frac{\partial^2 u}{\partial t^2} - \left(\frac{\partial P}{\partial \rho}\right)_s \frac{\partial^2 u}{\partial x^2} = 0 \tag{2.22}$$

which is the standard wave equation for longitudinal velocity variations with sound speed

$$c = \sqrt{\left(\frac{\partial P}{\partial \rho}\right)_s}. \tag{2.23}$$

If we are not restricted to considering small variations in the thermodyanamic variables but finite amplitude disturbances, the gasdynamic equations will admit solutions that are not single-valued. Consider again the one dimensional planar case. Eq. (2.4) and (2.5) can be rewritten as

$$\frac{\partial \rho}{\partial t} + \frac{\partial(\rho u)}{\partial x} = 0 \tag{2.24}$$

and

$$\frac{\partial u}{\partial t} + u\frac{\partial u}{\partial x} + \frac{1}{\rho}\frac{\partial P}{\partial x} = 0, \tag{2.25}$$

respectively. We can rewrite Eq. (2.24) as

$$\frac{\partial \rho}{\partial t} + \frac{d(\rho u)}{d\rho}\frac{\partial \rho}{\partial x} = 0 \tag{2.26}$$

and Eq. (2.25) as

$$\begin{aligned} \frac{\partial u}{\partial t} + u\frac{\partial u}{\partial x} + \frac{1}{\rho}\frac{\partial P}{\partial x} &= \frac{\partial u}{\partial t} + u\frac{\partial u}{\partial x} + \frac{1}{\rho}\frac{dP}{du}\frac{\partial u}{\partial x} \\ &= \frac{\partial u}{\partial t} + \left(u + \frac{1}{\rho}\frac{dP}{du}\right)\frac{\partial u}{\partial x} = 0. \end{aligned} \tag{2.27}$$

Rearranging Eq. (2.26), we have

$$\frac{\partial \rho/\partial t}{\partial \rho/\partial x} = -\frac{d(\rho u)}{d\rho} \tag{2.28}$$

which at constant density becomes

$$\left(\frac{\partial x}{\partial t}\right)_{\rho} = -\frac{d(\rho u)}{d\rho} = -\left(u + \rho\frac{du}{d\rho}\right). \tag{2.29}$$

Eq. (2.29) is the velocity of the wave at constant density. Similary, we rearrange Eq. (2.27),

$$\left(\frac{\partial x}{\partial t}\right)_{u} = -\left(u + \frac{1}{\rho}\frac{dP}{du}\right), \tag{2.30}$$

to obtain the wave velocity at constant fluid velocity. We know that the velocity of the wave is only a function of the fluid density. This mean that the wave velocity at constant density ρ is equal to the wave velocity at constant fluid velocity u and permits us to equate Eq. (2.29) and Eq. (2.30) and arrive at

$$\rho\frac{du}{d\rho} = \frac{1}{\rho}\frac{dP}{du}. \tag{2.31}$$

We can rewrite this equation using Eq. (2.23) as

$$\rho\frac{du}{d\rho} = \frac{1}{\rho}\frac{dP}{du} = \frac{1}{\rho}\frac{dP}{d\rho}\frac{d\rho}{du} = \frac{c^2}{\rho}\frac{d\rho}{du} \tag{2.32}$$

and reaarange as

$$\frac{du}{d\rho} = \pm\frac{c}{\rho}. \tag{2.33}$$

Integrating both sides of Eq. (2.33) yields an expression for the fluid velocity:

$$\int du = u = \pm\int \frac{c^2}{\rho c}d\rho = \pm\int \frac{dP}{\rho c}. \tag{2.34}$$

Differentiating this, we arrive at an expression for the speed of sound as a function of the fluid velocity

$$c(u) = \frac{1}{\rho}\frac{dP}{du} \tag{2.35}$$

and insert into Eq. (2.30) to obtain

$$\left(\frac{\partial x}{\partial t}\right)_u = (u + c(u)) + f(u) \tag{2.36}$$

where $f(u)$ is some arbitrary function of the fluid velocity. Eq. (2.36) describes a wave traveling with velocity $v = u + c(u)$. Since the sound speed c varies with the density, different parts of the wave front will have different velocities. It can be shown (Ref. [7]) that $d(u + c)/d\rho > 0$ which implies that the wave velocity increases with density. As a consequence, the velocity profile of a finite amplitude wave will steepen with increasing time eventually leading to an unphysical multivalued solution. It is at this point a shock discontinuity forms.

2.2 Shock Physics

When the flow variables no longer provide single-valued continuous solutions to the gasdynamic equations, it may admit discontinuous ones. This discontinuity is known as a shock front. The solutions, in this case, can be found by examining the flow variables across the discontinuity and applying the conservation laws.

Consider the simple case of a piston with cross-sectional area A moving from the left with speed u into a gas with initial density ρ_0 and pressure P_0.

This piston will form a region of compressed gas with density ρ_1 and pressure P_1 immediately in front of it that is bounded to the right by a discontinuity propagating with speed D. At some arbitrary time, the mass of the uncompressed gas contained in the volume ADt is set in motion by the piston. The compressed region has volume $A(D-u)t$ and conservation of mass requires the condition

$$\rho_1 A(D-u)t = \rho_0 ADt. \tag{2.37}$$

This mass from the motion of the piston acquires momentum $\rho_0 ADt \cdot u$ and is equal, by Newton's law, to the impulse generated by the pressure difference across the discontinuity. Thus, conservation of momentum requires that

$$\rho_0 ADtu = (P_1 - P_0)At. \tag{2.38}$$

Lastly, we have conservation of energy. The uncompressed gas will experience a gain in both kinetic and internal energies which is equal to the work performed by the piston,

$$\rho_0 ADt\left(\varepsilon_1 - \varepsilon_0 + \frac{u^2}{2}\right) = P_1 Aut. \tag{2.39}$$

Eqns. (2.37) to (2.39) represent conservation laws in the stationary laboratory frame. It is more convenient, however, to express these equations in the rest frame of the moving shock discontinuity, allowing us to use only quantities pertaining to the region in front and behind the shock. Note that if D is the propagation speed of the discontinuity into the undisturbed gas, then $u_0 = -D$ is the velocity at which the uncompressed gas flows into discontinuity in the rest frame of the shock. Likewise, since the piston velocity u is equal to the

gas velocity in the compressed region, $u_1 = -(D - u)$ represents the gas velocity flowing out of the shock discontinuity. With these definitions, our mass, momentum, and energy conservation laws become, in the rest frame of the shock,

$$\rho_1 u_1 = \rho_0 u_0, \tag{2.40}$$

$$P_1 + \rho_1 u_1^2 = P_0 + \rho_0 u_0^2, \tag{2.41}$$

and

$$\varepsilon_1 + \frac{P_1}{\rho_1} + \frac{u_1^2}{2} = \varepsilon_0 + \frac{P_0}{\rho_0} + \frac{u_0^2}{2}, \tag{2.42}$$

respectively. The properties of the preschocked gas, ρ_0 and P_0, and a parameter that describes the strength of the shock, e.g. P_1, is assumed to be known in Eqns. (2.40)-(2.42). From these conservation laws, we can derive some general relationships that will be of use later. Eliminating one of the velocity terms from Eqn. (2.41) using Eqn. (2.40) leaves us with

$$u_0^2 = V_0^2 \frac{P_1 - P_0}{V_0 - V_1} \tag{2.43}$$

and

$$u_1^2 = V_1^2 \frac{P_1 - P_0}{V_0 - V_1}, \tag{2.44}$$

where we have introduced the specific volume, or volume per unit mass $V = 1/\rho$. What we have in Eqns. (2.43) and (2.44) is an expression for the square of the respective gas velocities in terms of pressure and specific volume. Substituting these into our energy conversation equation (Eqn. (2.42)), we obtain

$$\varepsilon_1 - \varepsilon_0 = \frac{1}{2}(P_1 + P_0)(V_0 - V_1). \tag{2.45}$$

Eqn. (2.45)is referred to as the Hugoniot relation. In simple terms, it is the curve represented by the function

$$P_1 = H(V_1, P_0, V_0), \tag{2.46}$$

where the initial pressure and specific volume are parameters characterizing the curve. A gas that undergoes a shock will have initial and final values of P and V fall on this curve.

For a perfect ideal gas, one in which the specific heats are constant, we can derive more explicit forms of the Hugoniot curve. The equation of state governing an ideal gas is

$$\varepsilon = c_v T = \frac{1}{\gamma - 1} PV, \tag{2.47}$$

where c_v is the specific heat at constant volume and γ is the adiabatic index, or polytropic index, of the gas. The adiabatic index is equal to the ratio of the specific heats at constant pressure and constant volume and is a measure of the number of degrees of freedom of the gas f, given by

$$\gamma = 1 + \frac{2}{f}, \tag{2.48}$$

Immediately from Eqn.(2.47), we have the temperature ratios across the shock front given by

$$\frac{T_1}{T_0} = \frac{P_1 V_1}{P_0 V_0}. \tag{2.49}$$

Substituing Eqn. (2.47) into Eqn. (2.45), we have a more explicit form of the Hugoniot relation

$$\frac{P_1}{P_0} = \frac{(\gamma + 1)V_0 - (\gamma - 1)V_1}{(\gamma + 1)V_1 - (\gamma - 1)V_0}, \tag{2.50}$$

from which we can rearrange to get the specific volume ratios as well

$$\frac{V_1}{V_0} = \frac{(\gamma-1)P_1 + (\gamma+1)P_0}{(\gamma+1)P_1 + (\gamma-1)P_0}. \tag{2.51}$$

Figure 2.1 shows a sample Hugoniot curve that passes through the initial state P_0 and V_0. A gas that undergoes a shock compression will have both their initial and final states on the Hugoniot curve, as inidicated by the points A and B. The transition to the final state is discontinuous and does not follow a path along the curve for shocks. Geometrically, the shock velocity can be calculated from the Hugoniot curve by considering the slope of the line passing through the initial and final states A and B in Figure 2.1. The slope of this line is $m = (P_1 - P_0)/(V_1 - V_0)$ and from Eqn.(2.43), the shock velocity is given by

$$D^2 = u_0^2 = V_0^2 \frac{P_1 - P_0}{V_0 - V_1} = -mV_0^2 \tag{2.52}$$

Let us now consider the special case of a strong shock, i.e., one in which $P_1/P_0 \gg 1$. The specific volume ratio simplifies to

$$\frac{\rho_1}{\rho_0} = \frac{V_0}{V_1} = \frac{\gamma+1}{\gamma-1}, \tag{2.53}$$

from which the temperature ratios also simplify to

$$\frac{T_1}{T_0} = \frac{\gamma-1}{\gamma+1}\frac{P_1}{P_0}. \tag{2.54}$$

The gas velocities in this limit become

$$u_0 = \left(\frac{\gamma+1}{2} P_1 V_0\right)^{1/2} \tag{2.55}$$

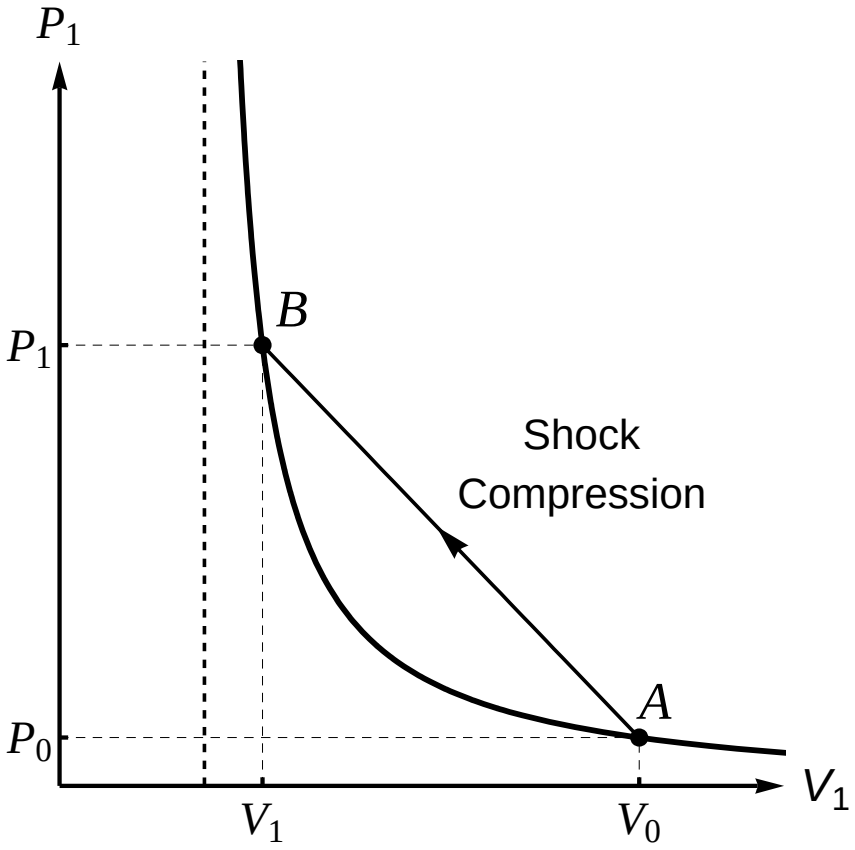

Figure 2.1: Hugoniot curve of a gas with initial state $A(V_0, P_0)$. The gas will transition to final state $B(V_1, P_1)$ after shock compression. The shock velocity is given by the slope of the straight line connecting points A and B.

and

$$u_1 = \left(\frac{(\gamma-1)^2}{2(\gamma+1)} P_1 V_0\right)^{1/2} = \left(\frac{\gamma-1}{\gamma+1}\right) u_0. \tag{2.56}$$

From these last two equations, we have

$$u = D + u_1 = \frac{2D}{\gamma+1} \tag{2.57}$$

Equations (2.53) to (2.57) are collectively known as the strong shock jump

conditions which relates the quantities on either sides of the shock front in terms of the adiabatic index γ. Note that for a monatomic gas, the density ratio is 4 accross a purely adiabatic shock.

2.3 Blast Waves

For a shock driven by a supersonically moving piston the trajectory is constant and ahead of the piston, traveling faster than the piston itself. Much of this analysis assumed a constant driving mechanism (i.e. the moving piston) and a homogenous preshocked medium. If, however, the drive source is not constant in time, then the shock properties are also altered. Let us now consider the extreme case of a point explosion in which a large amount of energy is released instantaneously. What results is a blast wave: a shock wave that decays in strength over time as it propagates into the medium.

Qualitatively, the release of energy heats the surrounding medium and pushes the gas radially outward exerting a subtantial amount of pressure. The material is unable to sufficiently react to the explosion and what results is a peak in the density and pressure of the material culminating in a shock front discontinuity. The pressure is a maximum at the shock front and decreases as we move radially in towards the origin until it settles to a constant value. The temperature, on the other hand, increases slowly as we move inward from the shock. In the vicinity of the shock front, this increase is rather slow at first but rises more rapidly in the region where the pressure has settled to its constant value. The temperature is much higher close to the origin due to the fact that

the gas was heated by a very strong shock wave. As the subsequent volume of the blast wave becomes larger, the initial energy of the blast is spread out more resulting in a cooler temperature. The density profile drops abruptly in the constant-pressure region because of this sharp rise in temperature. Figure (2.2) shows a general illustration of the radial profiles of these quantities.

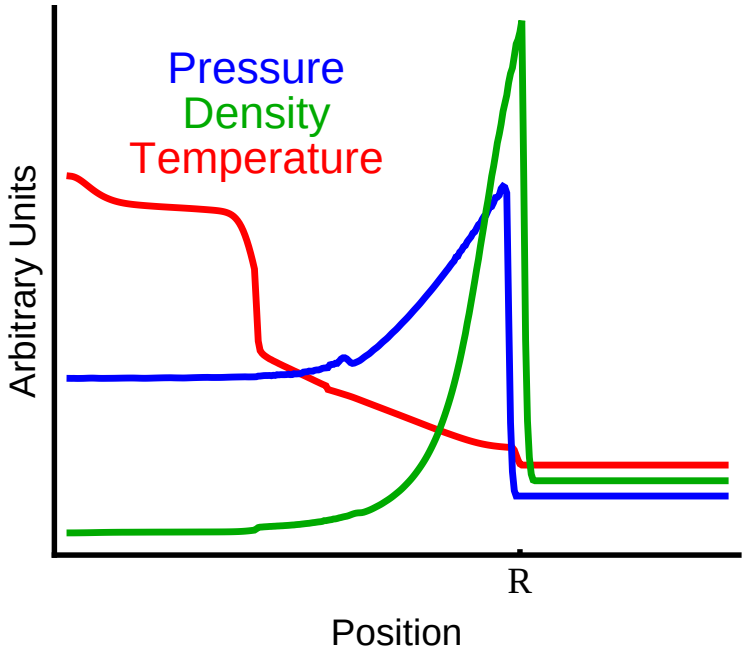

Figure 2.2: Radial profiles of pressure, density, and temperature of a blast wave from HYADES numerical simulation. The values were scaled in the vertical and offset slightly in the horizontal to each other so that the shock discontinuity from all three can be displayed. R is the position of the shock front.

In the ideal case of an energy-conserving strong explosion in a homogeneous atmosphere without viscosity, Sedov and Taylor [5] developed a self-similar solution to the blast wave propagation. The fundamental quantities

of this problem are the initial energy of the explosion E_0 and density ρ_0. For the solution to be self-similar, i.e., the coordinate variable r varies similarly in time, a dimensionless similarity parameter must be employed. For spherical geometry, the only combination of these variables that yield a dimensionless quantity is

$$\xi_0 = r\left(\frac{\rho_0}{E_0 t^2}\right)^{1/5}. \tag{2.58}$$

In general, the dimensionless similarity parameter for spherical, cylindrical, and planar blast waves are

$$\begin{aligned}
\xi_0 &= r\left(\frac{\rho_0}{E_0 t^2}\right)^{1/5} && \text{for spherical,} \\
\xi_0 &= r\left(\frac{\rho_0}{\varepsilon_0 t^2}\right)^{1/4} && \text{for cylindrical,} \\
\xi_0 &= r\left(\frac{\rho_0}{\varepsilon_0 t^2}\right)^{1/3} && \text{for planar.}
\end{aligned} \tag{2.59}$$

Here, ε_0 is the energy per unit length or energy per unit area for cylindrical and planar blast waves, respectively. The motion of the shock front will propagate as

$$\begin{aligned}
R(t) &= \xi_0\left(\frac{E_0}{\rho_0}\right)^{1/5} t^{2/5} && \text{for spherical,} \\
R(t) &= \xi_0\left(\frac{\varepsilon_0}{\rho_0}\right)^{1/4} t^{1/2} && \text{for cylindrical,} \\
R(t) &= \xi_0\left(\frac{\varepsilon_0}{\rho_0}\right)^{1/3} t^{2/3} && \text{for planar.}
\end{aligned} \tag{2.60}$$

The exponent of the variable t is referred to as the deceleration parameter and will be lower for the case when the blast wave is not energy-conserving.

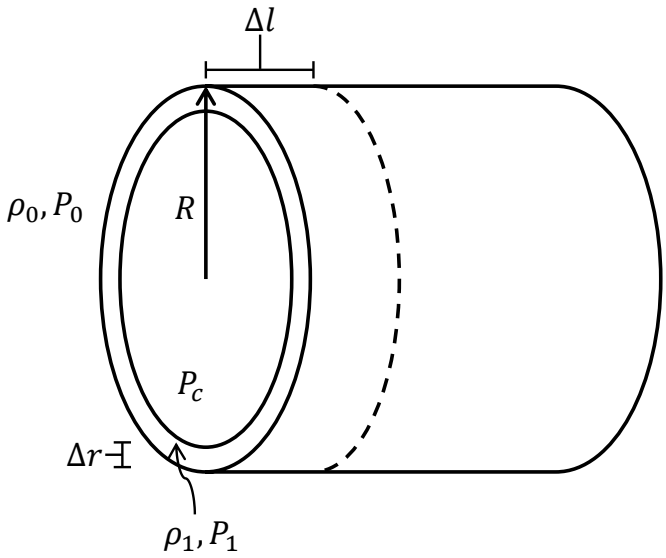

Figure 2.3: Schematic diagram of cylindrical blast wave. The density and pressure along with geometric quantities are labeled.

We can derive more explicit forms of the similarity parameter ξ_0 in the case of an adiabatic blast wave. Following the analysis for the spherical case presented in Zeldovich and Raizer [5], we can formulate an approximate expression for an adiabatic cylindrical blast wave created by a strong 'line-explosion' in a homogenous medium. The main assumption to be made in this simple case is that the entire mass of gas compressed by the explosion resides in a very thin shell just behind the shock front. Lets state the conservation of mass for an arbitrary length segment for the cylinder. The mass within a slice of the cylinder before the explosion is equal to the mass that is swept up and

concentrated in a thin-shelled ring,

$$\pi R^2 \Delta l \rho_0 = \Delta l 2\pi R \Delta r \rho_1 \tag{2.61}$$

where Δr is the thickness of this ring and P_c is the pressure within the inner boundary of the shell. The quantities with subscript 0 are the usual quantities in the ambient medium and quantities inside the the thin shell is denoted with subscript 1. Δl is the length of the cylinder in consideration. Fig.(2.3) shows a schematic diagram of a cylindrical blast wave with the relevant gas-dynamic quantities. Using the strong shock jump conditions for density, the shell thickness becomes

$$\Delta r = \frac{R(\gamma - 1)}{2(\gamma + 1)}. \tag{2.62}$$

Assume that the pressure P_c within the inner shell boundary is some fraction α of the pressure P_1 inside the shell that is driving the blast wave:

$$P_c = \alpha P_1. \tag{2.63}$$

Now we invoke Newton's Law on our ring equating the change in momentum of the ring to the pressure within the inner boundary:

$$\begin{aligned} \frac{d}{dt}(Mu) &= \frac{d}{dt}\left(\pi R^2 \Delta l \rho_0 u\right) \\ &= 2\pi R P_c \Delta l = 2\pi R \alpha P_1 \Delta l, \end{aligned} \tag{2.64}$$

and substitute in Eqns. (2.57) and (2.55) for the gas velocity and pressure in terms of the shock velocity, respectively:

$$\frac{d}{dt}\left(\pi R^2 \rho_0 \frac{2}{\gamma + 1} D\right) = 2\pi R \alpha \frac{2}{\gamma + 1} \rho_0 D^2. \tag{2.65}$$

Simplifying, our equation is now

$$\frac{d}{dt}\left(R^2 D\right) = 2R\alpha D^2. \tag{2.66}$$

The time derivative can be rewritten as

$$\frac{d}{dt} = \frac{dR}{dt}\frac{d}{dR} = D\frac{d}{dR} \tag{2.67}$$

and is substituted in our equation:

$$R^2\frac{dD}{dR} = 2RD(\alpha - 1). \tag{2.68}$$

Separating variables and integrating, we have

$$D = aR^{2(\alpha-1)} \tag{2.69}$$

where a is a constant of integration. Of course, since $D = dR/dt$, we further reduce Eqn. 2.69 and integrate again giving us

$$R = [(3 - 2\alpha)at]^{1/(3-2\alpha)}. \tag{2.70}$$

The constants a and α are determined by using conservation of energy. Since most of the mass is concentrated in the ring, the kinetic energy of the gas is

$$E_K = \frac{Mu^2}{2} = \frac{\pi R^2}{2}\Delta l \rho_0 u^2 \tag{2.71}$$

while the internal cavity bounded by the inner boundary of the ring contains most of the internal energy

$$E_T = \frac{1}{\gamma - 1}PV = \frac{1}{\gamma - 1}\pi R^2 \Delta l P_c. \tag{2.72}$$

The total energy per unit length is

$$\varepsilon \equiv \frac{E}{\Delta l} = \frac{E_K + E_T}{\Delta l} = \frac{1}{\gamma - 1}\pi R^2 P_c + \frac{\pi R^2}{2}\rho_0 u^2$$
$$= \pi \rho_0 a^2 \left[\frac{2\alpha R^{2+4(\alpha-1)}}{(\gamma^2 - 1)} + \frac{2R^{2+4(\alpha-1)}}{(\gamma+1)^2} \right], \tag{2.73}$$

where we have substituted in Eqns.(2.57), (2.55), and (2.69) in the last step. Since this analysis is for an adiabatic, i.e., energy conserving, blast wave, ε must not have any dependence on the variable R requiring its exponent to be zero:

$$\alpha = 1/2. \tag{2.74}$$

Lastly, inserting this value for α back into Eqn. (2.73) to solve for a gives us

$$a = \left(\frac{\varepsilon}{\rho_0} \right)^{1/2} \left[\frac{(\gamma+1)^2(\gamma-1)}{\pi(3\gamma-1)} \right]^{1/2}, \tag{2.75}$$

and an explicit form of the blast wave trajectory

$$R(t) = \left(\frac{\varepsilon_0}{\rho_0} \right)^{1/4} \left[\frac{4(\gamma+1)^2(\gamma-1)}{\pi(3\gamma-1)} \right]^{1/4} t^{1/2}. \tag{2.76}$$

2.4 Radiative Blast Waves

In Section 2.3, we analyzed the motion of a blast wave with the condition that energy is conserved throughout its propagation. If, however, energy loss mechanisms are present, we must modify our equations. Blast waves can lose energy, for example by radiative processes at the shock front, which will result in a greater deceleration than that for the energy-conserving case. There are two cases in which analytic solutions exist for the blast wave motion in

which radiative cooling is present. The first is what is known as the Pressure Driven Snowplow (PDS) regime [8]. In this regime, only the outer layer of the shocked material cools by radiation, driven by the high pressure of the hot interior. This interior region does not experience any radiative cooling and the density is assumed to be small enough to be negligible. The thin cool layer "snowplows" through the outside medium [9] and for cylindrical blast waves, the deceleration parameter drops down to $n = 3/8$. When a blast wave enters the PDS regime, it is referred to as being fully radiative. Derivation of the deceleration parameter in the PDS regime is quite involved and will not be covered in this thesis. The second case is known as the Momentum Conserving Snowplow (MCS) regime. This occurs when radiative losses behind the shock front (the interior region) are significant and sufficiently large enough that both the pressure and density are negligible. Only momentum, but not energy, is conserved and the shock is simply "coasting." A derivation for the deceleration parameter is straightforward and relies simply on momentum conservation. We start with the mass of a cylindrical section of gas

$$M = \pi R^2 \Delta l \rho_0 \tag{2.77}$$

which again is swept up and concentrated in a thin outer shell or ring. Its momentum is given by

$$p = Mu = \frac{2MD}{\gamma + 1}, \tag{2.78}$$

and since it is conserved, its time derivative must be zero:

$$\dot{p} = \frac{2}{\gamma + 1}(\dot{M}D + M\dot{D}) = 0. \tag{2.79}$$

The time derivate of M is

$$\dot{M} = 2\pi\Delta l\rho_0 R\dot{R}, \tag{2.80}$$

and inserting into Eqn. (2.79), we have

$$\dot{p} = \frac{2\pi\Delta l\rho_0 R}{\gamma+1}(2\dot{R}D + R\dot{D}) = 0. \tag{2.81}$$

The only nontrivial solution to this is

$$2D^2 = -R\dot{D}. \tag{2.82}$$

Next, we separate variables and integrate to solve for D:

$$\ln D = -2\ln R + c, \tag{2.83}$$

where c is an integration constant. Rewritten, we have

$$D = bR^{-2} = \frac{dR}{dt}, \tag{2.84}$$

where $b \equiv e^c$. We again separate variables and integrate to solve for R

$$R(t) = 3bt^{1/3}. \tag{2.85}$$

We see that when radiation or other energy loss mechanisms are present, the blast wave trajectory propagates with a lower deceleration parameter. Indeed, one way to experimentally determine if a blast wave experiences any energy loss is to observe its trajectory and compare the deceleration parameter to the Sedov-Taylor value of $n = 1/2$.

If the blast wave is not fully radiative, i.e., in the PDS regime, but still has energy loss through radiation, an analytic approximation can be used to solve for its motion. Liang and Keilty [10, 11] derived a simple model by employing a radiative loss parameter and an effective adiabatic index in the radiating region to account for any energy loss. In this analysis we separate the blast wave into three regions: the unshocked outside medium, the thin shocked layer, the outer boundary of which all radiative losses occur, and the postshocked rarefied internal cavity. In the last region, no radiative losses are assumed to take place. Here, the adiabatic index in the postshocked region and outside medium are assumed to be known. Fig. (2.4) shows a schematic diagram of the blast wave profile. In this analysis, we denote quantities in the ambient medium with a subscript 0 and the rarefied internal cavity with a subscript c. Quantities in the shocked layer are denoted with subscript f. We begin with an assumption that the energy loss rate is a constant fraction of the energy flux across the shock [10]. Following Cohen et al., [12], we define this fraction as

$$\epsilon = \frac{4(\gamma - \gamma_1)}{(\gamma - 1)(\gamma_1 + 1)^2}, \tag{2.86}$$

where γ_1 is the effective adiabatic index in the shocked layer. The energy loss rate for a cylindrical blast wave is then

$$\frac{dE}{dt} = -\pi \rho_0 D^3 R \, \epsilon. \tag{2.87}$$

Note that in the fully radiative case, $\epsilon = 1$ and $\gamma_1 = 1$ while in the energy conserving case, $\epsilon = 0$ and $\gamma_1 = \gamma$. Fig. (2.4) shows a sample plot of ϵ for a

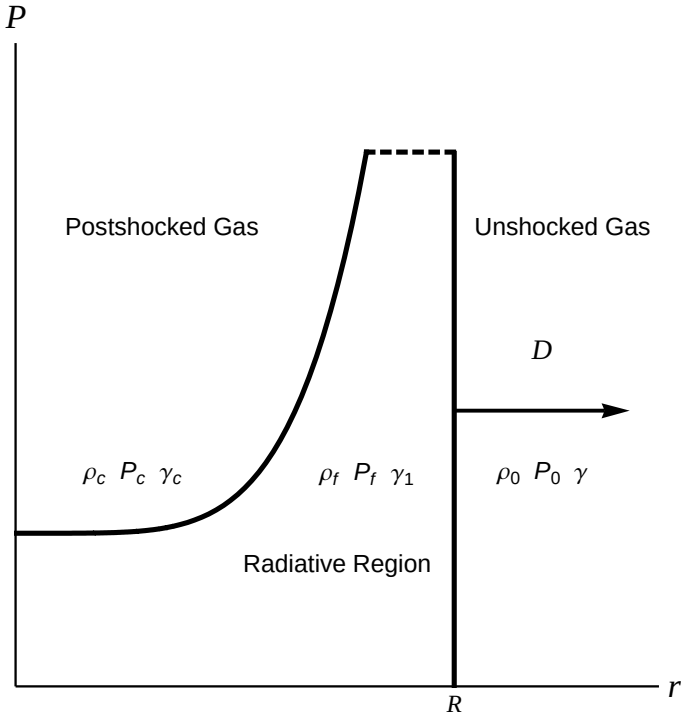

Figure 2.4: Diagram of the semiradiative shock profile with the different regions. Radiative losses only occur in the thin layer just behind the shock dicontinuity

monatomic gas. The internal energy is again

$$E_T = \frac{P_c V}{\gamma_c - 1} \tag{2.88}$$

but with a more precise formulation for the volume as

$$V = \pi(R - \Delta r)^2 \Delta l. \tag{2.89}$$

The total energy per unit length is

$$E = E_T + E_K = \frac{P_c \pi (R - \Delta r)^2}{\gamma_c - 1} + \frac{1}{2} M u^2, \tag{2.90}$$

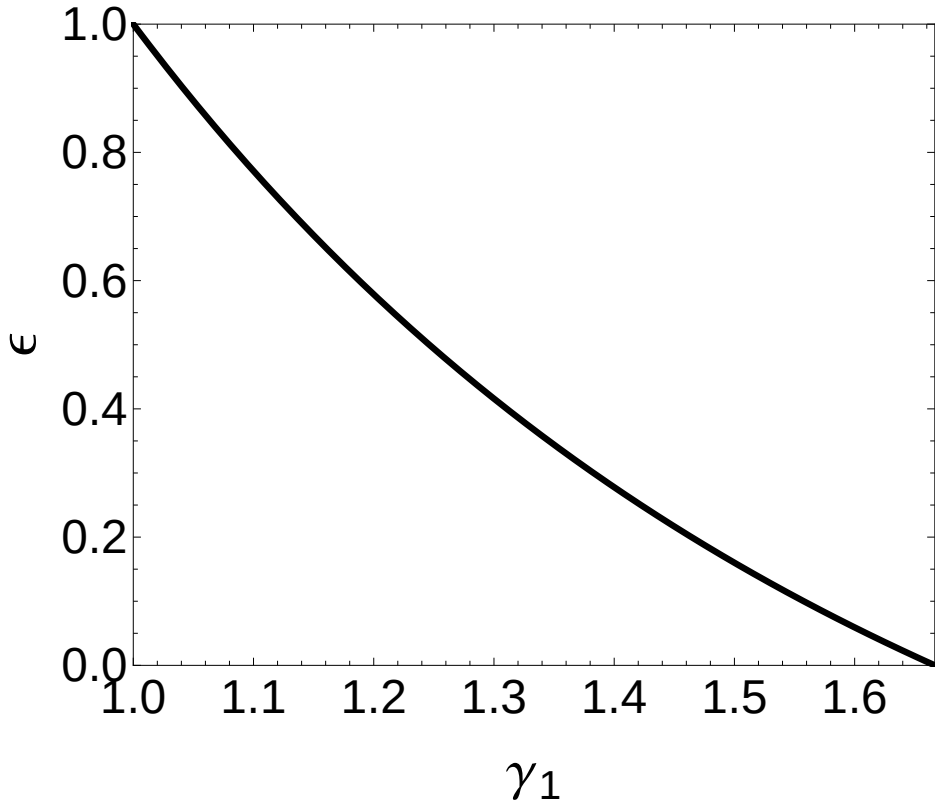

Figure 2.5: Plot of the energy loss fraction ϵ as a function of γ_1 for a monatomic gas. ϵ parametrizes the fraction of energy lost to radiation with the conditions $\epsilon = 0$ for $\gamma_1 = \gamma = 5/3$ (purely adiabatic) and $\epsilon = 1$ for $\gamma_1 = 1$ (fully radiative).

where $M = \pi R^2 \rho_0$. Now we Taylor-expand the quantity $(R - \Delta r)^2$ about Δr:

$$\begin{aligned}(R - \Delta r)^2 &= R^2 \left[1 + 2\left(\frac{-\Delta r}{R}\right) + \frac{2}{2!}\left(\frac{-\Delta r}{R}\right)^2 + ...\right] \\ &\simeq R^2 - 2\Delta r R,\end{aligned} \tag{2.91}$$

and retain only the first-order terms. We know from the previous section that

$$\Delta r = \frac{R}{2}\frac{(\gamma_1 - 1)}{(\gamma_1 + 1)}. \tag{2.92}$$

Inserting Eqn. (2.92) into Eqn. (2.91) gives us

$$(R-\Delta r)^2 \simeq R^2 - \frac{2R}{2}\frac{(\gamma_1-1)}{(\gamma_1+1)}R = R^2 - R^2\frac{(\gamma_1-1)}{(\gamma_1+1)}$$
$$= R^2\left[1-\frac{(\gamma_1-1)}{(\gamma_1+1)}\right]$$
$$= \frac{2R^2}{\gamma_1+1}, \tag{2.93}$$

and inserting this into our total energy yields

$$E = \frac{P_c\pi}{\gamma_c-1}\frac{2R^2}{\gamma_1+1} + \frac{1}{2}\frac{\pi R^2\rho_0 u^2}{(\gamma_1+1)^2}$$
$$= \frac{2\pi\rho_0 a^2}{(\gamma_1+1)^2}\left[\frac{2\alpha}{(\gamma_c-1)}+1\right]R^{4\alpha-2}. \tag{2.94}$$

In Eqn. (2.94), we use our usual shock jump conditions for u and P_1 and Eqn. (2.69) for D. Next we differentiate the total energy with respect to time

$$\frac{dE}{dt} = \frac{2\pi\rho_0 a^2}{(\gamma_1+1)^2}\left[\frac{2\alpha}{\gamma_c-1}+1\right](4\alpha-2)R^{4\alpha-3}\frac{dR}{dt}$$
$$= \frac{2\pi\rho_0 a^2}{(\gamma_1+1)^2}\left[\frac{2\alpha}{\gamma_c-1}+1\right](4\alpha-2)R^{4\alpha-3}D$$
$$= \frac{2\pi\rho_0 a^2}{(\gamma_1+1)^2}\left[\frac{2\alpha}{\gamma_c-1}+1\right](4\alpha-2)R^{4\alpha-3}aR^{2\alpha-2} \tag{2.95}$$

and equate this to Eqn. (2.4) giving us

$$\frac{2}{(\gamma_1+1)^2}\left[\frac{2\alpha}{\gamma_c-1}+1\right](4\alpha-2) = \frac{-4(\gamma-\gamma_1)}{(\gamma-1)(\gamma_1+1)^2}. \tag{2.96}$$

Eqn. (2.96) is a quadratic equation for α with the solution

$$\alpha = \frac{2-\gamma_c+\sqrt{(2-\gamma_c)^2+4(\gamma_c-1)(\gamma_1-1)/(\gamma-1)}}{4} \tag{2.97}$$

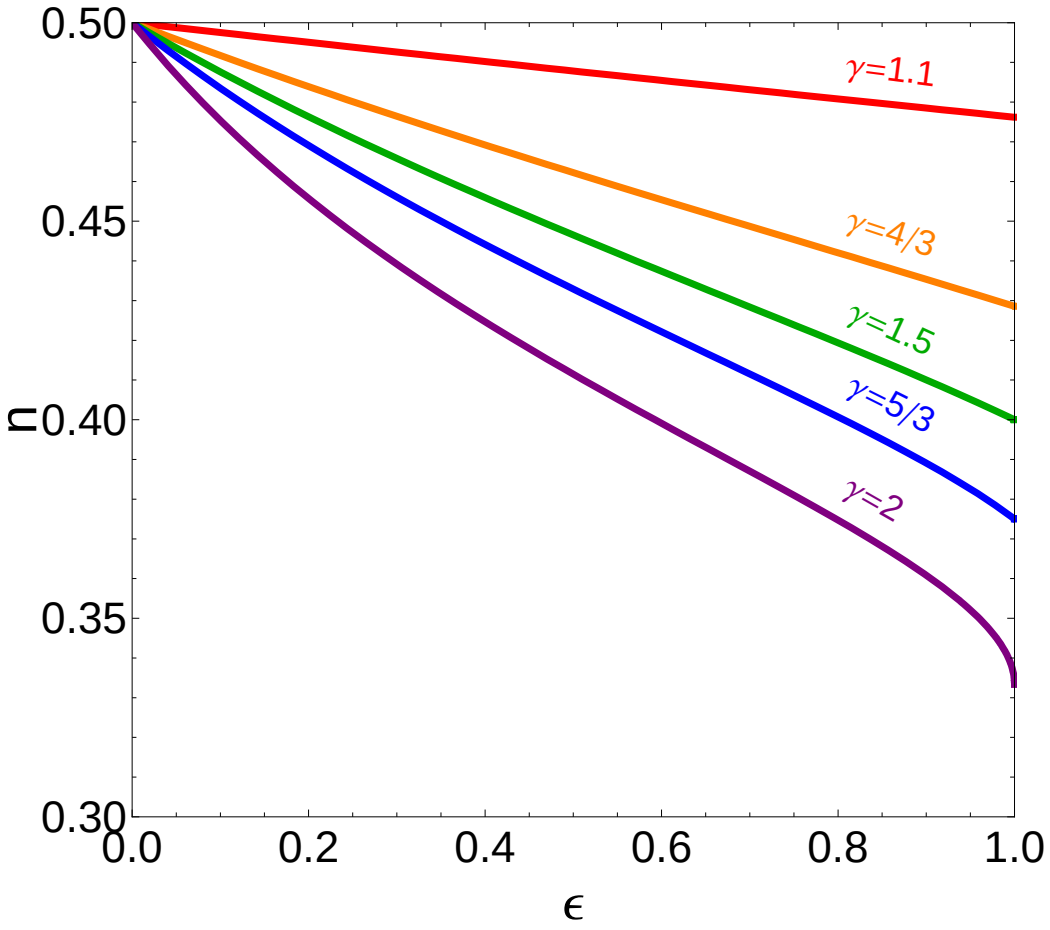

Figure 2.6: Plot of power law index n vs. ϵ for various values of $\gamma = \gamma_c$. Note that for all γ's s converges to the Sedov-Taylor value of $s = 1/2$ when $\epsilon = 0$.

and is related to the deceleration parameter

$$n = \frac{1}{3 - 2\alpha} \tag{2.98}$$

via Eqn. (2.70). Figure (2.6) are plots of the deceleration parameter n for various values of γ. We see that for all nonzero values of ϵ, the power law index is lower than the Sedov-Taylor value: when radiative losses are present,

the blast slows down faster. This analysis treats radiative losses indirectly by decreasing the value of γ in the shocked layer by use of an effective adiabatic index γ_1 rather than including energy loss terms explicitly in the equations of motion. The adiabatic index is a measure of the degrees of freedom that a gas possesses,

$$\gamma = 1 + \frac{2}{f}, \tag{2.99}$$

where f is the number of degrees of freedom. For a nonradiating monatomic gas, $f = 3$ and $\gamma = 5/3$. When energy is coupled to the system by means other than just translational motion, such as when radiative losses are present, more degrees of freedom exist thereby lowering the adiabatic index. We can see this explicitly in our analysis by using Eqn. (2.70) and inserting the result for α derived in Eqn. (2.97):

$$\begin{aligned} 3 - \frac{1}{n} =& 2\alpha \\ & \left[\frac{2 - \gamma_c + \sqrt{(2-\gamma_c)^2 + 4(\gamma_c - 1)(\gamma_1 - 1)/(\gamma - 1)}}{2}\right]. \end{aligned} \tag{2.100}$$

Rearranging, we have

$$\gamma_1 = \frac{\gamma - 1}{4(\gamma_c - 1)}\left[\left(4 + \gamma_c - \frac{2}{n}\right)^2 - (2 - \gamma_c)^2\right] + 1. \tag{2.101}$$

Eqn. (2.101) is the effective adiabatic index γ_1 as a function of the power-law index n. Figure (2.7) are plots of γ_1 vs. n for several values of γ_c. Several features of Fig. (2.7) should be pointed out. First, note that for all γ_c values, the curve first intersects the $\gamma_1 = 1$ line when $n = 1/3$. This is expected for a fully radiative ($\gamma_1 = 1$) blast wave and the problem reduces to the momentum

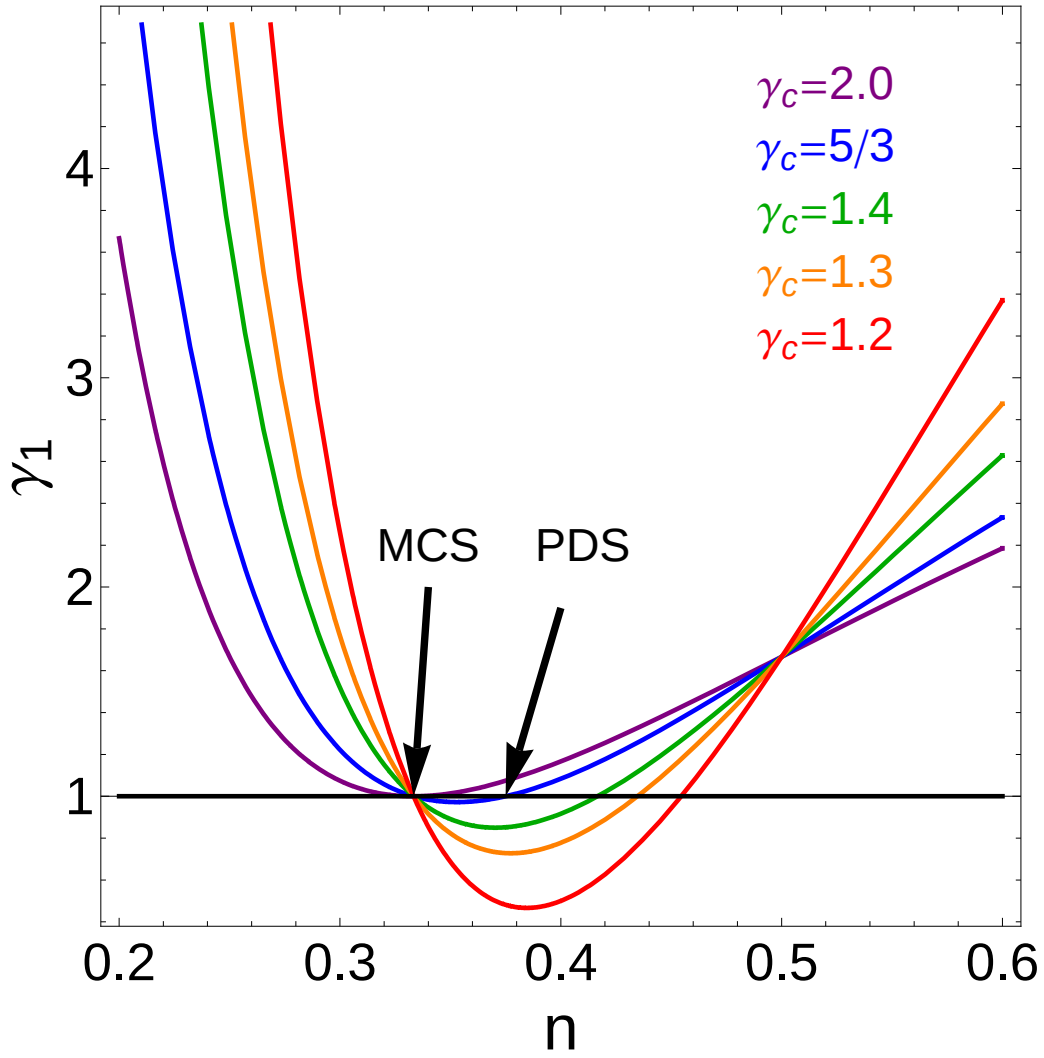

Figure 2.7: Plot of γ_1 vs. n for a monatomic gas ($\gamma = 5/3$) for several values of the cavity adiabatic index γ_c. Note that the curves intersect the $\gamma_1 = 1$ line at $n = 1/3$ and for the γ_c case, the second intercept occurs at $n = 3/8$.

conserving snowplow regime as discussed in the previous section. Furthermore, we see for that for the case of $\gamma_c = \gamma = 5/3$, the second intercept occurs when

$n = 3/8$, the value for the power-law index in the pressure driven snowplow regime. Lastly, we see that all curves converge on the value $\gamma_1 = 5/3$ as n approaches $1/2$ which would be the case for a purely adiabatic blast wave propagating in the Sedov-Taylor regime. For $\gamma_1 = 5/3$ this problem no longer treats the radiating layer as having a separate adiabatic index and the blast wave is purely adiabatic. This analysis does, however, have its drawbacks. We see that there is a range of values for n when the curve drops below the $\gamma_1 = 1$ line which would be an unphysical result and the model is simply inadequate. Nevertheless, this analysis, when applicable, is useful in diagnosing the degree to which radiative losses affect the blast wave motion by analyzing the trajectory and solving for the effective adiabatic index.

Further evidence of radiative cooling is the ionization/radiative precursor that accompanies the classic blast wave with a sharp density front [14]. This ionization precursor forms from the radiation that escapes the shock front and pre-ionizes the upstream medium. Experimentally, this effect is observed by measuring the radial distribution of the electron density and is manifested as a gradual gradient that forms radially outward from the shock front.

A consequence of radiative losses is that the temperature in the blast front is lowered and becomes more compressible leading to a thinner shock shell. A thinner shell is important in the astrophysical context because of its increased susceptibility to instabilities. Large scale structure are observed in many radiative SNR's that are due to these instabilities and may be a possible explanation for galactic and stellar formation.

2.5 Radiative Processes

In the previous sections, we discussed the effects radiative losses has on the overall temporal evolution of blast waves. There are three main physical processes by which which a blast wave loses energy through radiation. These are: Bremsstrahlung or free-free radiation, bound-free transitions, and lastly bound-bound transitions or line radiation [5].

2.5.1 Free-Free Transitions and Bremsstrahlung Emission

From classical electrodynamics, a charged particle moving in an external Coulomb field will emit radiation and subsequently slow down. This mechanism is referred to as bremsstrahlung which translated from German means "braking radiation." Consider a freely moving charged particle, for example an electron, moving in an external field due to a positive ion of charge Ze, where Z is the ionization state and e is the charge of an electron. This electron will experience an acceleration and emit energy

$$S(t) = \frac{2}{3}\frac{e^2}{c^3}\mathbf{w}^2(t) \tag{2.102}$$

per unit time. Here, $\mathbf{w}(t)$ is the acceleration vector. The total energy during the duration of travel past the ion is then

$$\Delta E = \int_{-\infty}^{\infty} S(t)\,dt = \frac{2}{3}\frac{e^2}{c^3}\int_{-\infty}^{\infty} \mathbf{w}^2(t)\,dt. \tag{2.103}$$

Since the electron is freely moving with transitions occurring in the continuum of ion levels, the radiation emitted will have some continuous spectra. This

allows us to Fourier expand the acceleration vector in terms of frequency to obtain a similar expression for the the total energy:

$$\Delta E = \int_0^\infty S(\nu)\, d\nu = \frac{16\pi^2}{3}\frac{e^2}{c^3}\int_0^\infty \mathbf{w}^2(\nu)\, d\nu, \tag{2.104}$$

where

$$\mathbf{w}(\nu) = \frac{1}{2\pi}\int_{-\infty}^{\infty} \mathbf{w}(t) e^{-i2\pi\nu t}\, dt. \tag{2.105}$$

Here,

$$S(\nu) = \frac{16\pi^2}{3}\frac{e^2}{c^3}\mathbf{w}^2(\nu), \tag{2.106}$$

represents the energy emitted per unit frequency interval at frequency ν. Now, instead of a single electron passing an ion, lets consider a beam of electrons at constant number density N_e with initial velocity v passing an ion. The number of electrons with impact parameter ρ passing by an ion per unit time will be $N_e v \cdot 2\pi\rho d\rho$. Since each electron emits an amount of energy ΔE derived earlier, this ring of electrons will emit energy $\Delta E N_e v \cdot 2\pi\rho d\rho$ per unit time. The total power emitted by these electrons passing by an ion is found by integrating the previous quantity for all possible impact parameters, i.e., integrating with respect to ρ from 0 to ∞, or

$$q = \int_0^\infty \Delta E N_e 2\pi\rho\, d\rho. \tag{2.107}$$

Similarly, the power emitted in the frequency interval ν to $\nu + d\nu$ is

$$dq_\nu = d\nu \int_0^\infty S_\nu N_e v 2\pi\rho d\rho. \tag{2.108}$$

Integrating Eqn.(2.108) over all frequencies gives the total power:

$$q = \int_0^\infty dq_\nu = \int_0^\infty d\nu \int_0^\infty S_\nu N_e v 2\pi\rho d\rho. \tag{2.109}$$

Let us return to Eqn. (2.103) and derive an approximate expression for ΔE. An electron at a distance r from the ion experiences a force

$$\mathbf{F} = -\frac{Ze^2}{r^2}\hat{\mathbf{r}}. \tag{2.110}$$

The acceleration experienced by this electron is

$$\mathbf{w}(t) = -\frac{Ze^2}{mr^2}\hat{\mathbf{r}}. \tag{2.111}$$

If again the electron has an impact parameter ρ and is incident upon the ion with velocity v, then the time with which the electron experiences the Coulombic force is $t \simeq \rho/v$. Each of these electrons emits energy

$$\Delta E \simeq \frac{2}{3}\frac{e^2}{c^3}\mathbf{w}^2(t)\cdot t = \frac{2}{3}\frac{Z^2e^6}{m^2c^3\rho^3v}. \tag{2.112}$$

The frequency emitted by an electron with impact parameter ρ is of the order $\nu \sim 1/2\pi t = v/2\pi\rho$. After rearranging and some algebraic manipulations, we have $d\rho \sim 2\pi(\rho^2/v)d\nu$. A beam of electrons in an infinitesimal ring of area $2\pi\rho d\rho$ will emit radiant power

$$dq_\nu \simeq \Delta E N_e v 2\pi\rho d\rho \simeq \frac{8\pi^2}{3}\frac{N_e Z^2 e^6}{m^2c^3v}d\nu \tag{2.113}$$

at the frequency interval ν to $\nu + d\nu$. This is an approximate analysis of the problem at hand. An exact calculation of dq_ν can be found in Ref. [13]:

$$dq_\nu = \frac{32\pi^2}{3\sqrt{3}}\frac{Z^2e^6}{m^2c^3v^2}d\nu \qquad \text{for } \nu \gg \frac{mv^3}{2\pi Ze^2}, \tag{2.114}$$

$$dq_\nu = \frac{32\pi}{3}\frac{Z^2e^6}{m^2c^3v^2}\ln\frac{mv^3}{1.78\pi\nu Ze^2}d\nu \qquad \text{for } \nu \ll \frac{mv^3}{2\pi Ze^2}. \tag{2.115}$$

The above result is for a unit electron flux $N_e v = 1$ cm^{-2} sec^{-1}. The higher frequency result given by Eqn. (2.114) only differs from the simple model (Eqn. (2.113)) by a numerical factor of $4/\sqrt{3}$. The lower one, however, differs by a numerical factor and a logarithmic one that is a function of ν. This is because the lower frequency radiation comes from those electrons whose impact parameters are large: $\nu \to 0$ as $\rho \to \infty$. Evidently, electrons with impact parameters $\rho > v/2\pi\nu$ give a relatively larger contribution to the radiant energy at frequency ν than those with $\rho \sim v/2\pi\nu$. For comparison to later results, we compute the total energy emitted by an electron beam of unit flux in the high frequency limit:

$$q_{\nu\,\mathrm{brems}} = \int dq_\nu = \int_0^\infty \frac{32\pi^2}{3\sqrt{3}} \frac{Z^2 e^6}{m^2 c^3 v^2} d\nu = \frac{32\pi^2}{3\sqrt{3}} \frac{Z^2 e^6}{m^2 c^3 v} = \frac{dq_\nu}{d\nu} \frac{E}{h} \tag{2.116}$$

As an example, let us consider a high Z plasma and calculate its emission properties. We know from Eqn. (2.114) the power emitted per ion for a unit flux of electrons. If the electron velocities are in a Maxwell-Boltzmann distribution,

$$f(v) = \left(\frac{m_e}{2\pi k_B T} \right)^{3/2} 4\pi v^2 e^{-\frac{m_e v^2}{2k_B T}}, \tag{2.117}$$

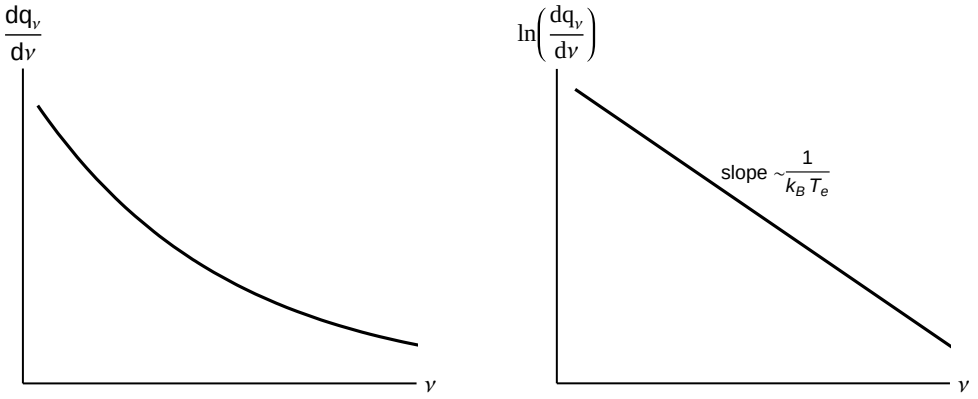

Figure 2.8: Plots of Energy emitted per unit time, per unit frequency interval. The vertical axis on the second plot is logarithmic and the temperature is calculated from the slope of this line: $m \sim 1/k_B T$.

then the total power emitted is

$$\begin{aligned} q &= \int_0^\infty d\nu \int_v^\infty \frac{32\pi^2}{3\sqrt{3}} \frac{Z^2 e^6}{m_e^2 c^3 v^2} N_e N_i \, v \, f(v) \, dv \\ &= \int_0^\infty d\nu \int_v^\infty \frac{32\pi^2}{3\sqrt{3}} \frac{Z^2 e^6}{m_e^2 c^3} N_e N_i \left[\left(\frac{m_e}{2\pi k_B T} \right)^{3/2} 4\pi v e^{-\frac{m_e v^2}{2k_B T}} \right] dv \\ &= \int_0^\infty \frac{32\pi^{3/2}}{3\sqrt{6}} \frac{Z^2 e^6}{m_e^{3/2} c^3} \frac{N_e N_i}{(k_B T)^{1/2}} e^{-\frac{h\nu}{k_B T}} \, d\nu \\ &= \frac{32\pi^{3/2}}{3\sqrt{6}} \frac{Z^2 e^6}{m_e^{3/2} h c^3} N_e N_i (k_B T)^{1/2}. \end{aligned} \tag{2.118}$$

In a high Z plasma, the temperature can be calculated from $dq_\nu/d\nu$ measurements as Fig.(2.8) shows. Using values from a 100 eV aluminum plasma ($Z = 13$) with densities $N_e = 8 \times 10^{23}$ cm^{-3} and $N_i = 6 \times 10^{22}$ cm^{-3}, the total radiated power from bremsstrahlung emission is $q = 3 \times 10^{10}$ eV/s.

2.5.2 Bound-Free Transitions and Electron Capture Emission

A free electron can be captured by a hydrogen-like ion emitting a photon in the process. Since the electron is transitioning from a continuum of free states to a bound state, the emitted radiation takes on a continuous spectrum. For a hydrogen-like atom, the energy levels are given by

$$E_n = -\frac{I_H Z^2}{n^2} = -\frac{I}{n^2} \tag{2.119}$$

where $I = I_H Z^2 = |E_1|$ is the absolute value of the ground-state energy, or ionization potential: it is the energy required to remove a ground-state electron into the continuum of free states. $I_H = 2\pi^2 me^4/h^2$ is the ground state energy for a hydrogen atom ($Z = 1$) and can be derived from elementary quantum mechanics. n is the principle quantum number of the atom. To calculate the energy emitted by a capture event, we must consider the cross section of a free electron into any of the bound states with principle number n. Using Eqn.(2.116), the effective radiation in some frequency interval $\Delta\nu$ is $\Delta q_\nu = (dq_\nu/d\nu)\Delta\nu$, which from quantum mechanics is equal to $h\nu\Delta\sigma_\nu$, where $\Delta\sigma_\nu$ represents the cross section of photoemission in the frequency interval $\Delta\nu$. In other words, $\Delta\sigma_\nu$ represents the cross section of photoemission with energies in the range $h\nu$ to $h\nu + h\Delta\nu$. Since we are considering not just any photoemission event, but specifically one in which a free electron recombines with an ion into some state n, we can represent $\Delta\sigma_\nu$ as the product $\sigma_{cn}\Delta n$ where σ_{cn} is the cross section of an electron captured into level n. Then, we

have

$$\sigma_{cn} = \frac{\Delta\sigma_\nu}{\Delta n} = \frac{1}{h\nu}\frac{\Delta q_\nu}{\Delta n} = \frac{1}{h\nu}\left(\frac{dq_\nu}{d\nu}\right)\frac{\Delta\nu}{\Delta n} \tag{2.120}$$

For large n, we have from Eqn.(2.119) $|dE_n/dn| = h\Delta\nu/\Delta n = 2I_H Z^2/n^3$ which represents the energy spacings. Inserting this value and our expression for the energy spacing into Eqn.(2.120) gives us

$$\sigma_{cn} = \frac{128\pi^4}{3\sqrt{3}}\frac{Z^4 e^{10}}{mc^3 h^4 v^2 \nu}\frac{1}{n^3} = \frac{32\pi^2}{3\sqrt{3}}\frac{Z^2 e^6}{hmc^3}\frac{I_H Z^2}{Eh\nu n^3}, \tag{2.121}$$

the cross section of photorecombination to the bound state n for an electron with initial energy $E = mv^2/2$. The photon energy emitted during this capture is

$$h\nu = E + |E_n| = \frac{mv^2}{2} + \frac{I_H Z^2}{n^2}. \tag{2.122}$$

The total cross section for photorecombination into any hydrogen-like ion can be calculated by summing over all n Eqn.(2.121):

$$\begin{aligned}\sigma_{c\,\mathrm{tot}} &= \frac{32\pi^2}{3\sqrt{3}}\frac{Z^2 e^6}{hmc^3}\sum_{n=1}^{\infty}\frac{I_H Z^2}{Eh\nu n^3} \\ &= \frac{32\pi^2}{3\sqrt{3}}\frac{Z^2 e^6}{hmc^3}\sum_{n=1}^{\infty}\left[\frac{1}{n^3}\frac{1}{(E/I_H Z^2 + 1/n^2)}\right].\end{aligned} \tag{2.123}$$

Let us return to Eqn.(2.120) and calculate the relative contribution of bremsstrahlung emission to electron capture emission. The total energy emitted by photorecombination processes is

$$q_{cap} = \sum_{n=1}^{\infty} h\nu\sigma_{cn} = \sum_{n=1}^{\infty} h\nu\left[\frac{1}{h\nu}\left(\frac{dq_\nu}{d\nu}\right)\frac{\Delta\nu}{\Delta n}\right]. \tag{2.124}$$

The quantity $(dq_\nu/d\nu)$ is given by Eqn.(2.116) since photorecombination involves an electron initially in the continuum of free states. Then, the ratio of

energies from electron capture to bremsstrahlung emission is

$$\frac{q_{cap}}{q_{brems}} = \frac{I_H Z^2}{E} \sum_{n=1}^{\infty} \left(\frac{2}{n^3} \right) \simeq I_H Z^2 / E, \tag{2.125}$$

where the summation is of order unity. This implies that the total emittance ratio is proportional to the ratio of energies involved in each of these processes. Consider again a high Z plasma with electron velocities in a Maxwell-Boltzmann distribution. Since σ_{cn} goes as $\sim 1/n^3$, free electrons will have an affinity for the lower states. If we assume that electrons recombine into the $n = 1$ ground state, the total power emitted is then

$$\begin{aligned} q &= \int_0^{\infty} \sigma_{cn}\, v\, f(v)\, h\nu N_e N_i dv \\ &= \int_0^{\infty} \frac{128\pi^4}{3\sqrt{3}} \frac{Z^4 e^{10}}{m_e c^3 h^4 v^2 \nu} \frac{1}{n^3} h\nu N_e N_i v\, f(v) dv \\ &= \int_0^{\infty} \frac{128\pi^4}{3\sqrt{3}} \frac{Z^4 e^{10}}{m_e c^3 h^3} \frac{1}{n^3} N_e N_i \left[\left(\frac{m_e}{2\pi k_B T} \right)^{3/2} 4\pi v\, e^{-\frac{mv^2}{k_B T}} \right] dv \\ &= \frac{256\pi^{7/2}}{3\sqrt{6}} \frac{Z^4 e^{10}}{m^{1/2} c^3 h^3} \frac{N_e N_i}{(k_B T)^{1/2}} \end{aligned} \tag{2.126}$$

The ratio of power emitted by photon capture and bremstrahlung emission is

$$\begin{aligned} \frac{q_{cap}}{q_{brems}} &= \frac{256\pi^{7/2}}{3\sqrt{6}} \frac{Z^4 e^{10}}{m^{1/2} c^3 h^3} \frac{N_e N_i}{(k_B T)^{1/2}} \frac{3\sqrt{6}}{32\pi^{3/2}} \frac{m_e^{3/2} h c^3}{Z^2 e^6} \frac{1}{N_e N_i (k_B T)^{1/2}} \\ &= 8\pi^2 \frac{Z^2 e^4 m_e}{h^2} \frac{1}{(k_B T)} \end{aligned} \tag{2.127}$$

At low temperature, say around 10 eV and below, recombination radiation is higher than from bremsstrahlung emission. At high temperatures, recombination is negligible compared to bremsstrahlung emission. Intuitively, this is consistent with the $q_{cap} \sim 1/(k_B T)^{1/2}$ behavior as it is more difficult for hotter electrons to recombine.

2.5.3 Bound-Bound Transitions and Line Emission

An excited electron bound to an atom can decay into a lower quantum state and emit a photon in the process. Since the energy levels of an atom are discrete, the emitted spectra will also exhibit discrete peaks, or lines. From quantum theory, the radiation rate is given by

$$q = h\nu_{nn'}A_{nn'} = \frac{64\pi^4}{3}\frac{\nu_{nn'}^4}{c^3}|\mathbf{d}|^2, \tag{2.128}$$

where $A_{nn'}$ is the decay rate of the spontaneous transition from state n to n', $\nu_{nn'}$ is the frequency of the emitted photon, and $|\mathbf{d}|$ is the matrix element of the dipole moment. $|\mathbf{d}|$ is calculated for transitions that occur between states n and n'. If we denote the nth state with quantum number α and the n'th state with quantum number α', then the decay rate is given by

$$A_{nn'} = \frac{64\pi^4}{3}\frac{\nu_{nn'}}{hc^3}\left[\frac{1}{g_n}\sum_{\alpha}\sum_{\alpha'}\langle n', \alpha'|\mathbf{d}|n, \alpha\rangle^2\right], \tag{2.129}$$

where g_n is the degeneracy of the nth level. If we assume that a gas of hydrogen-like atoms is exposed to light of a continuous spectrum, we can calculate the emission resulting from transitions between levels n and n'. From principles of detailed balance, a relationship exists between light absorption resulting in an excitation of an electron and light emission when an excited electron decays. The energy absorption rate per unit volume is

$$\int U_\nu c\, d\nu\, \sigma_{\nu n'n}N_{n'} = N_{n'}U_\nu c\int \sigma_{\nu nn'}d\nu = N_{n'}U_\nu\, c\, h\, \nu_{nn'}B_{n'n}, \tag{2.130}$$

where U_ν is the radiant energy density and $\sigma_{\nu n'n}$ is the absorption cross section. Here, $B_{n'n}$ is the absorption coefficient for the n to n' transition and is given

by

$$B_{n'n} = \frac{1}{h\nu_{nn'}} \int \sigma_{\nu n'n} d\nu. \tag{2.131}$$

Note that in analyzing absorption, we have interchanged the states such that n' represents the lower state. The emissivity of an atom for these transitions is related to the absorption coefficient by

$$f_{abs_{n'n}} = \frac{mc}{\pi e^2} h\nu_{nn'} B_{n'n}, \tag{2.132}$$

which is known as the oscillator strength for absorption. For emission, the oscillator strength is simply

$$f_{emiss_{nn'}} = -\frac{g_{n'}}{g_n} f_{abs_{n'n}} = -\frac{A_{nn'}}{3\gamma}. \tag{2.133}$$

γ represents the inverse of the time during which the oscillator energy decreases by a factor of e. For hydrogen-like atoms, the frequency of transitions is given by the Balmer series formula (we revert to the conventional notation of representing n as the lower state)

$$\nu_{nn'} = \frac{I_H Z^2}{h} \left(\frac{1}{n^2} - \frac{1}{n'^2} \right). \tag{2.134}$$

With this, the oscillator strength is now

$$f_{nn'} = \frac{32}{3\pi\sqrt{3}} \frac{1}{n^5} \frac{1}{n'^3} \frac{1}{(1/n^2 - 1/n'^2)^3}. \tag{2.135}$$

Let us now calculate the emission for our hydrogen-like atoms excited by collisions with hot electrons instead of absorption of light and further assume that most transitions are from $n = 1$ to $n' = 2$. The radiation rate is now

$$q \simeq (\text{exc. rate}) \cdot h\nu = \sum_{n=2}^{\infty} \int \sigma_{nn'} v f(v) n_e n_{i,1}^{Z-1} \cdot \Delta E_{nn'}, \tag{2.136}$$

where

$$\sigma_{nn'} \simeq \frac{2\pi}{m_e}\left(\frac{\hbar^2}{m_e a_0}\right)^2 \frac{1}{v^2}\frac{f_{nn'}}{\Delta E}. \tag{2.137}$$

$f(v)$ is the Maxwell-Boltzmann distribution as before and ΔE is the energy difference between states n' and n. Of course, only those electrons with velocities $v \geq (2\Delta E/m_e)^{1/2}$ can excite the atoms which sets the lower limit in the integral:

$$\begin{aligned} q &= \sum_{n'=2}^{\infty} \int_{\left(\frac{2\Delta E}{m_e}\right)}^{\infty} \frac{2\pi}{m_e}\left(\frac{\hbar^2}{m_e}\right)\frac{f_{nn'}}{\Delta E} v\, 4\pi \left(\frac{m_e}{2\pi k_B T_e}\right)^{3/2} \exp^{-mv^2/2k_B T_e} \Delta E n_c n_i^{Z-1}\, dv \\ &\simeq \frac{6\sqrt{2}}{5}\pi^{1/2}\frac{\hbar^4}{m_e^{5/2}a_0^2}\frac{1}{(k_B T_e)^{1/2}} \exp^{(-\Delta E/k_B T_e)} n_e n_i^{Z-1}, \end{aligned} \tag{2.138}$$

where

$$a_0 = \frac{h^2}{4\pi^2 m e^2}, \tag{2.139}$$

is the Bohr radius. In Eqn.(2.9), the second equality makes use of the assumption that most transitions occur between states $1 \rightleftharpoons 2$. Emission spectra from a high Z plasma will have recombination radiation and line emission "sitting" on top of a bremsstrahlung background. Figure (2.9) shows qualitatively emission spectra from a high Z plasma.

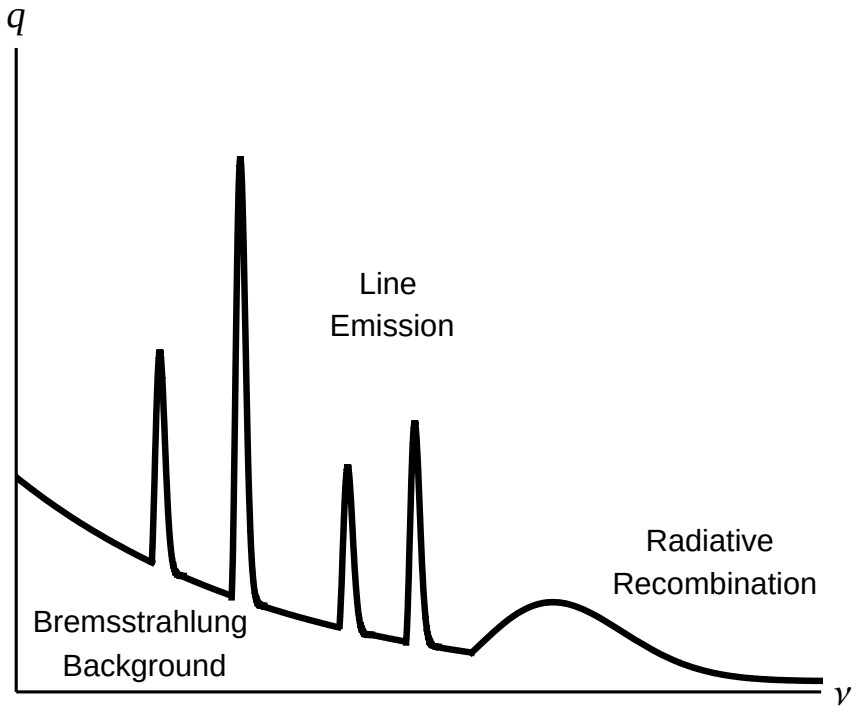

Figure 2.9: Example of an emission spectra from a high Z plasma showing the various sources of radiation.

Chapter 3

Hydrodynamic Instabilities

3.1 Supernova Remnants and Hydrodynamic Scaling

Once a star exhausts most or all of the nuclear fuel in its core, fusion reactions are no longer able to sustain the pressure necessary to prevent the core against its own gravitational collapse. If the gravitational potential energy is not sufficient enough, the star can collapse into a black hole or end up as a neutron star. Otherwise, the star can ejects most of the mass in its outer layers through a violent explosion resulting in a supernova. In general, supernova explosions undergo three phases in its evolution [15]. First is the explosion phase in which the core explosion results in a shock wave that propagates inside the progenitor star causing it to expand. The second phase occurs when the resulting ejecta drive a blast wave through the interstellar medium (ISM). Within this phase, the blast wave eventually propagates with the Sedov-Taylor solution provided the conditions discussed in Chapter 2 are satisfied. After the Sedov-Taylor expansion ends, the blast wave will propagate with a smaller power law index due to radiative cooling. Lastly, once the blast wave has expanded enough such that the intial energy of explosion is distributed in a sufficiently large volume, it enters a decay phase and eventually becomes an acoustic wave in the ISM.

The ejected material is initially heated to many keV's and is fully ionized. At these high temperatures, most of the radiative emission is due to bremsstrahlung processes. As the temperature decreases below the keV range, radiative recombination and line emission become more significant in the emission spectra such as the example in Fig.(2.9). Fig.(3.1) is the emission spectrum from supernova remnant W49B. Note the emission lines on top of the smoother bremsstrahlung continuum. Only bremsstrahlung emission is present below $\sim$ 2keV.

Ryutov et al. [2] developed a theorectical framework for scaling the hydrodynamic properties of supernovae to laboratory experiments. The conditions under which the two systems behave indentically requires the assumption that they behave as ideal, compressible hydrodynamic fluids with zero viscosity and thermal conductivity. The continuity and Euler's equations remain invariant under the scaling transformations

$$\begin{aligned} \mathbf{r} =& a\mathbf{r_1}\,; \quad \rho = b\rho_1\,; \quad P = cP_1\,; \\ t = a\sqrt{\frac{b}{c}}t_1\,; & \quad \mathbf{v} = \sqrt{\frac{c}{b}}\mathbf{v_1}, \end{aligned} \tag{3.1}$$

where a, b,and c are arbitrary positive numbers. Accordingly, the two systems will behave identically if their Euler numbers are the same, i.e., if

$$v\sqrt{\frac{\rho}{P}} = v_1\sqrt{\frac{\rho_1}{P_1}} \tag{3.2}$$

holds. The timescales of the two systems are also related by Eqn.(3.1) if

$$\tau_1 = \tau\frac{h_1}{h}\sqrt{\frac{P/\rho}{P_1/\rho_1}} \tag{3.3}$$

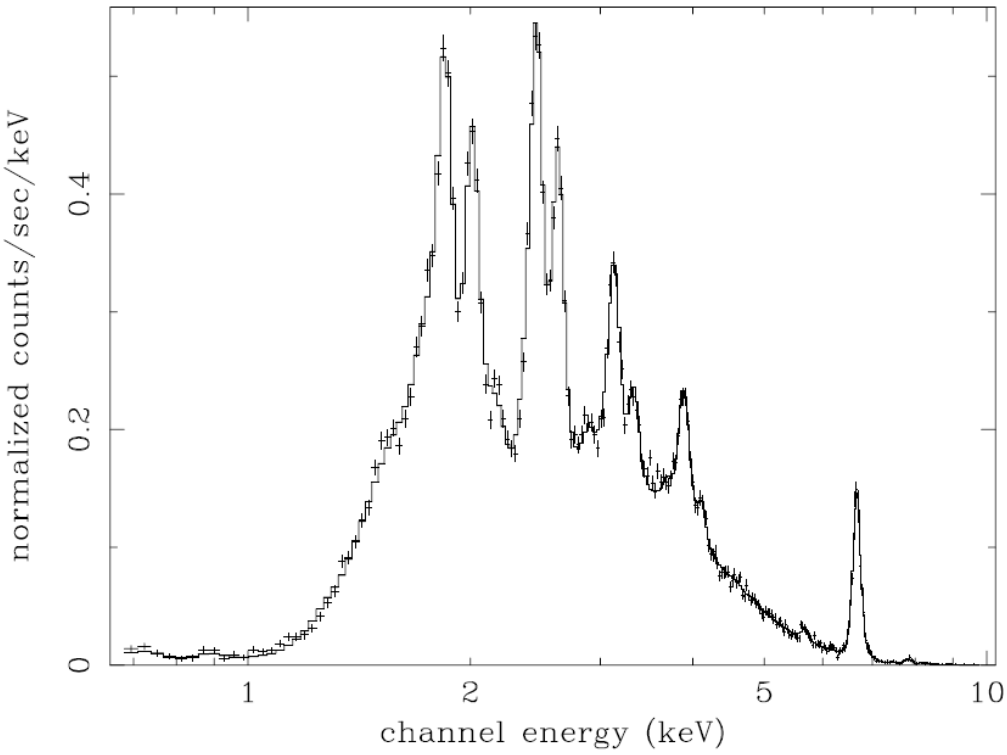

Figure 3.1: Spectrum from supernova remnant W49B. The line emissions are from Si, S, Ar, Ca, and Fe overlaid on the bremsstrahlung continuum. This figure is taken from Ref. [17]

holds. In Eqn.(3.2), h is the scale lengths of the system. The timescales can be for any physically significant process such as when h is of a certain value or the time when instabilities start to grow. The timescale of interest for our purposes is when radiative effects are important. If the environment is optically thin, that is, if the radiation mean free path from bremsstrahlung emission $\bar{l}_{\rm brems} \gg h$, then the timescale of interest is when radiative cooling plays a more significant role than hydrodynamic cooling, $\tau_{\rm thin} \gg \tau_{\rm hydro}$. For

the hot, fully ionized plasma inside a supernova interior, the bremsstrahlung mean free path is

$$\bar{l}_{\text{brems}}\,(\text{cm}) = 1.7 \times 10^{37}\,\frac{[\,T\,(\text{eV})\,]^{7/2}}{Z^3[\,N_i\,(\text{cm}^{-3})\,]^2}. \tag{3.4}$$

The characteristic time for when radiative cooling is significant is set by dividing the energy density by the radiative power density:

$$\tau_{\text{thin}}\,(\text{s}) = 2.4 \times 10^{-12}\frac{(Z+1)\,T\,(\text{eV})}{ZN_i\,(\text{cm}^{-3})\Lambda_N}\,, \tag{3.5}$$

where Λ_N is the normalized cooling rate (in ergs $\text{cm}^{-3}s^{-1}$) [16]. Even though recombination radiation and line emission can be significant in the temperature range from 10 eV to 3 keV, we use the mean free path for bremsstrahlung radiation as an approximation.

Using values for a young supernova (1987A) from Ryutov et al. [2], we can calculate our scaling parameters and validate the hydrodynamic similarity of the two systems. Table 3.1 summarizes the parameters found in SN 1987A

Table 3.1: Characteristic Parameters of Shocked Ejecta in SN1987A at 13 yr and Laboratory Experiments

Quantity	SNR Value	Laboratory Value
Scale Height (cm)	3.0×10^{16}	.1
Shock Velocity (cm/s)	9.5×10^{8}	5.0×10^{6}
Density (g/cm^3)	1.0×10^{-22}	3.0×10^{-5}
Pressure (dyn/cm^2)	1.0×10^{-5}	1.0×10^{6}
Temperature (eV)	3.0×10^{4}	5

at about 13 yr after start of the ejecta phase and approximate values in the

experiments conducted for this thesis. The temperature in our experiment were estimated from numerical simulations (to be discussed in CH(5)) and mass densities calculated from experimental parameters. Using Eqn.(3.1), we have the scaling parameters $a = 3\times10^{17}$ and $b = 3.3\times10^{-18}$. The pressure was calculated from the ideal gas law as an approximation given our mass density and temperature. Our scaling parameter for pressure is then $c = 9.6 \times 10^{-12}$. The Euler numbers for our two systems is

$$\mathrm{Eu.}_{\mathrm{SNR}} = 3 \qquad \mathrm{Eu.}_{\mathrm{LAB}} = 27. \tag{3.6}$$

The Euler numbers are close enough to each other such that we can consider the two systems as behaving similarly. The timescale in the laboratory, using Eqn.(3.3), is approximately lower by a factor of 5.7×10^{-15}, i.e., 1 yr in the SNR corresponds to roughly 180 ns. Using the timescale of 13 yrs for a young SNR, we have $\tau_{\mathrm{LAB}} = 2.32 \times 10^{-6}$ s, which is about two orders of magnitude longer than the actual experiments ($\sim 50\times10^{-9}$ s). However, SNRs may enter the radiatve phase at later times with different pressures, densities, shock velocities, and temperatures which will modify the scaling parameters and consequently the experimental timescale. In the case of SN 1987A, radiative cooling plays an insignificant role until the blast wave propagates far enough and collides with the surrounding cicumstellar ring [2]. This occurs about $\sim$ 20 yrs after the initial explosion. We summarize these values in Table 3.2, taken from Ref. [2, 18]. Using these values results in a laboratory timescale of $\sim$ 30 ns, closer than as calculated before. To futher validate our scaling, we

Table 3.2: Characteristic Parameters of SN 1987A at Time of Ring Collision

Quantity	Value in CSM
Scale Height (cm)	1.0×10^{17}
Shock Velocity (cm/s)	1.0×10^{9}
Density (g/cm^3)	2.2×10^{-19}
Pressure (dyn/cm^2)	3.5×10^{-5}
Temperature (eV)	170

calculate the time $\tau_{\rm thin}$ when radiative cooling is comparable to characteristic hydrodynamic timescales, that is, $\tau_{\rm thin} < h/s$ where

$$s(\text{cm s}^{-1}) = 1.3 \times 10^{6} \sqrt{\frac{(Z+1)T(\text{eV})}{A}} \tag{3.7}$$

is the sound speed for a monatomic gas. In other words, the radiative cooling time should be less than cooling from convection [2], in addition to the condition that $\bar{l}_{\rm brems} > h$. Together, then, Eqn.(3.4) is modified to include both conditions as

$$5.2 \times 10^{-30} \sqrt{\frac{(Z+1)T(\text{eV})}{A}} < h(\text{cm}) < 4.6 \times 10^{-11} \frac{A^2 [T(\text{eV})]^{7/2}}{Z^3 [\rho(\text{g cm}^{-3})]^2}, \tag{3.8}$$

for our laboratory plasma [2]. Eqn. (3.8) is plotted in Fig. (3.2) using values of $A = 36$, $Z \approx 4.5$, $h = .2\,\text{cm}$ from a krypton blast wave experiment. The mass density is taken from numerical simulations and is lower than what Fig. (3.2) might suggest. However, Eqn. (3.8) only takes into account bremsstrahlung emission as the only radiative cooling mechanism restricting the "desired regime" to that shown in Fig. (3.2). If other radiative processes

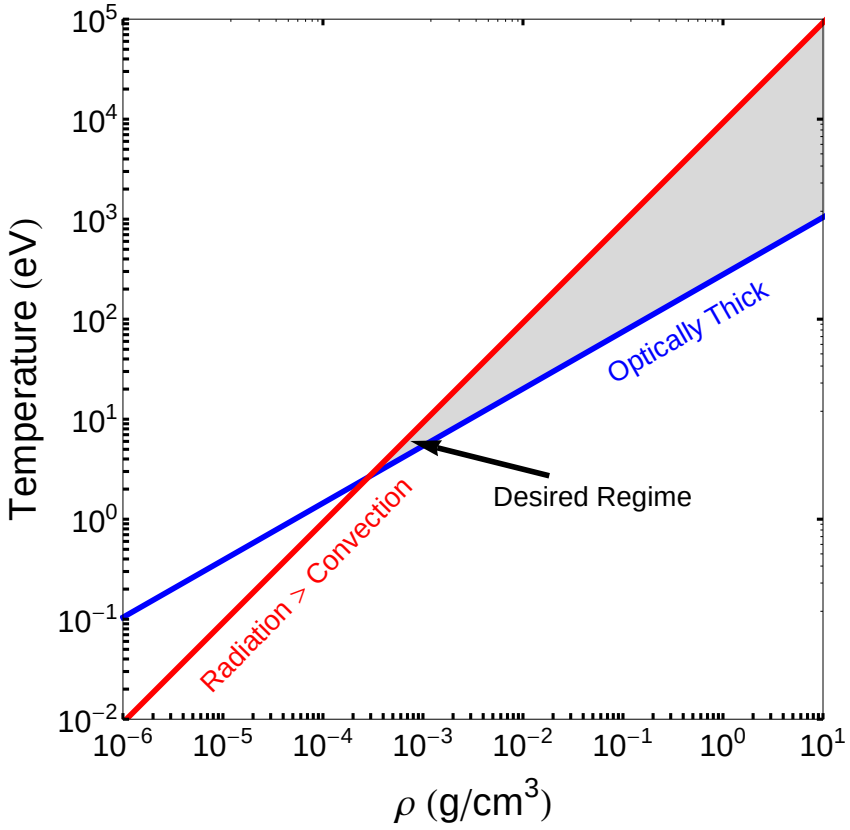

Figure 3.2: Plots of Eqn(3.8). The left inequality of Eqn. (3.8) is the red curve while the right inequality is the blue. The shaded area is the combined conditions and the desired parameter space for our experiments. If the radiated power is increased from with the inclusion of line emission instead of solely bremsstrahlung, the red line will curve upwards as density increases thereby extending our "desired regime" to lower densities and temperatures.

are included in addition to bremsstrahlung emission, then the "desired regime" may be extended to lower densities and temperatures.

3.2 Vishniac Overstability and Instability Growth

After the Sedov-Taylor phase radiative cooling will significantly affect the dynamics of the blast wave motion. Energy losses will effectively increase the number of degrees of freedom and as a result lower the adiabatic index γ along with the power law index with which the radius expands. In addition, the density inside the shock shell will increase since $\rho_1/\rho_0 = (\gamma+1)/(\gamma-1)$ while shell thickness becomes thinner [9]. A consequence of a thin shock shell is that it may become more susceptible to rippling instabilities on the surface. The study of blast wave instabilities are important in astrophysics because of their possible role in stellar and galactic formations [19]. These perturbations to the blast wave geometry can oscillate in time and the amplitudes grow depending on the wavelength of perturbations and the adiabatic index of the gas [21–23]. The oscillations are due to the disparity of forces acting on the blast wave surface as it propagates into the ambient medium. Consider a blast wave with a thin shock layer that has ripples on its surface. The ram pressure on the shock surface is always directed antiparallel to the direction of propagation while the thermal pressure inside acts normal to the shock front. The resultant force has a tangential component that causes mass to move from the ripple crests towards the troughs. When this occurs, the section that is now more massive acquires more momentum and decelerates at a lower rate. What was previously a crest now becomes a trough and vice versa, and this process repeats resulting in oscillating ripples. Fig. (3.3) shows qualitatively the mechanism that causes oscillations in the instabilities.

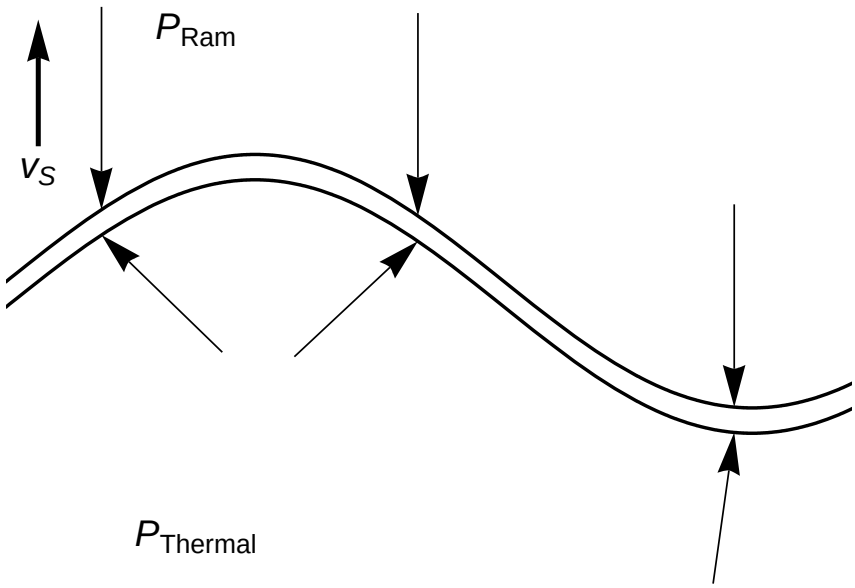

Figure 3.3: A thin shelled blast wave is propagating upwards through the ambient medium. The ram pressure always acts opposite the direction of propagation while the thermal pressure is normal to the surface. The resulting forces cause mass to move back and forth from the ripple crests and troughs

Vishiniac et al. developed a comprehensive theory [23] on these oscillatory perturbations and how they evolve in time. Much like the analysis of semiradiative blast waves in Ch. 2, the blast wave is assumed to be adiabatic and self-similar but with an altered polytropic index γ to account for radiative effects and shell thinning. The anaysis is done in three main steps: (1) The hydrodynmaic equations of motion are linearized with respect to perturbation variables. (2) The linearized equations are then normalized to the unperturbed

shock values. (3) The perturbations are defined and the equations are transformed into a similarity form. Appropriate boundary conditions are used to numerically solve the equations. Before these are solved, however, we require the values of hydrodynamic variables of an unperturbed blast wave normalized to the blast wave radius, i.e., the radial profiles of pressure, density, and gas velocity normalized to the shock front. We begin the analysis with the continuity and Euler's equations along with the entropy conservation equations. These are

$$\begin{aligned} \frac{\partial \rho}{\partial t} + \nabla \cdot (\rho \boldsymbol{v}) = 0, & \qquad \text{the continuity equation} \\ \rho \frac{\partial \mathbf{v}}{\partial t} + \rho(\mathbf{v} \cdot \nabla)\mathbf{v} + \nabla p = 0, & \qquad \text{the momentum equation} \\ \left(\frac{\partial}{\partial t} + \mathbf{v} \cdot \nabla \right) \log \frac{p}{\rho^{\gamma}} = 0. & \qquad \text{the entropy equation} \end{aligned} \tag{3.9}$$

Using the strong shock jump conditions, the pressure, density, and gas velocity relative to the ambient gas at the shock front can be expressed as

$$\begin{aligned} v_2 &= \frac{2u_1}{\gamma + 1}, \\ \rho_2 &= \rho_1 \frac{\gamma + 1}{\gamma - 1}, \\ p_2 &= \frac{2}{\gamma + 1} \rho_1 u_2^2. \end{aligned} \tag{3.10}$$

Here, the subscript 2 refers to quantities at the shock front and v_2 is the gas velocity relative to the ambient medium, while the subscript 1 refer to quantities in the ambient medium. u_1 is the shock front velocity with respect to the ambient medium. Note that the notation used in this section is different than that of Ch.2 to keep with consistency seen in many of the literature. We

can normalize v, p, and ρ, along with the similarity parameter ξ, to the values at the shock front as

$$\begin{aligned}
\tilde{v} &\equiv \frac{v}{v_2}, \\
\tilde{\rho} &\equiv \frac{\rho}{\rho_2}, \\
\tilde{p} &\equiv \frac{p}{p_2}, \\
\tilde{r} &\equiv \frac{\xi}{\xi_2} \equiv \frac{r}{r_2},
\end{aligned} \tag{3.11}$$

where r_2 is the radius of the blast wave and ξ_2 is the value of the similarity parameter,

$$\xi = r \left(\frac{\rho_1}{\varepsilon t^2} \right)^{1/4}, \tag{3.12}$$

at the shock front. The simlarity solutions are obtained by integrating our equations of motion. The derivation is not addressed in this thesis but can be found in Ref. [20]. These are

$$\begin{aligned}
\tilde{v} &= \tilde{r} v', \\
\tilde{\rho} &= \tilde{r}^{-\alpha_3/\alpha_2} v'^{-\alpha_3/\alpha_2} (\gamma + 1 - \gamma v')^{-\alpha_1\alpha_3/\alpha_2 + \alpha_4} \left(\frac{\gamma + 1 - 2v'}{\gamma - 1} \right)^{\alpha_5}, \\
\tilde{p} &= v' (\gamma + 1 - \gamma v')^{\alpha_4 - 2\alpha_1} \left(\frac{\gamma + 1 - 2v'}{\gamma - 1} \right)^{\alpha_5 + 1},
\end{aligned} \tag{3.13}$$

where

$$v'(\gamma+1-\gamma v')^{2\alpha_1}\left(\frac{2\gamma v'-\gamma-1}{\gamma-1}\right)^{2\alpha_2}=\tilde{r}^{-2},$$

$$\begin{aligned}
\alpha_1 &= \frac{1}{2},\\
\alpha_2 &= \frac{1-\gamma}{2\gamma},\\
\alpha_3 &= \frac{1}{\gamma},\\
\alpha_4 &= \frac{2}{2-\gamma},\\
\alpha_5 &= \frac{2}{\gamma-2}.
\end{aligned} \tag{3.14}$$

Fig.(3.4) shows the normalized shock profiles for different values of γ. The normalized, unperturbed shock profiles will be needed later for solving our perturbation equations later.

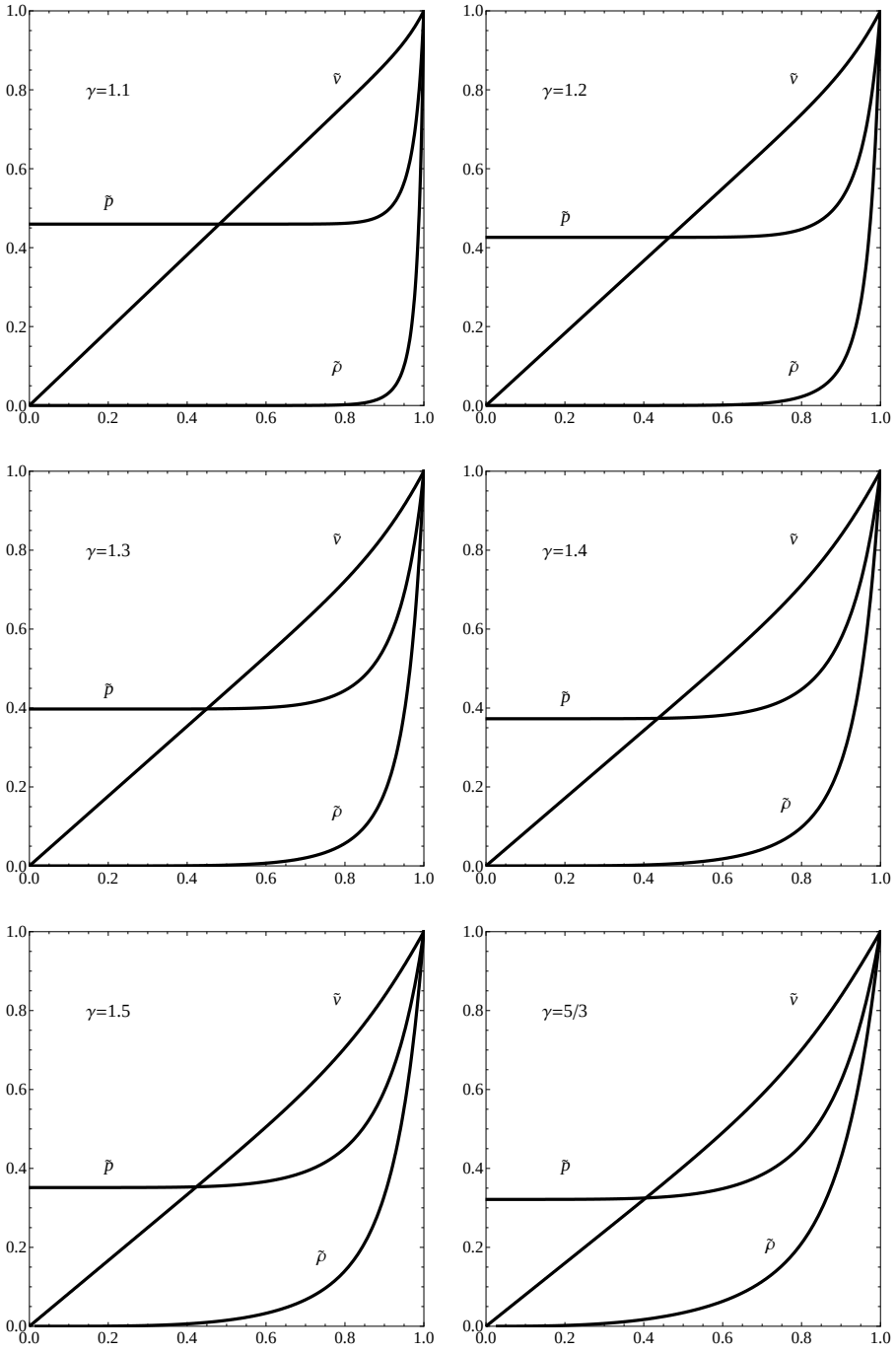

Figure 3.4: The normalized hydrodynamic quantities $\tilde{v}$, $\tilde{p}$, and $\tilde{\rho}$ as a function of normalized coordinate $\tilde{r}$ for various values of γ in cylindrical geometry.

Let us now linearize our hydrodynamic equations with perturbation variables defined as

$$\begin{aligned}
\delta\mathbf{v}(r,z,t) &\equiv \mathbf{v}(r,z,t) - v_0(r,t)\hat{\mathbf{r}}, \\
\delta\rho(r,z,t) &\equiv \rho(r,z,t) - \rho_0(r,z,t), \\
\delta p(r,z,t) &\equiv p(r,z,t) - p_0(r,z,t),
\end{aligned} \tag{3.15}$$

where the subscript 0 denotes the unperturbed quantities. The linearized equation are then

$$\begin{aligned}
\frac{\partial \delta\rho}{\partial t} + \frac{1}{r}\frac{\partial (r v_0 \delta\rho)}{\partial r} + \nabla\cdot(\rho_0 \delta\mathbf{v}) &= 0, \\
\frac{\partial \delta\mathbf{v}}{\partial t} + v_0\frac{\partial \delta\mathbf{v}}{\partial r} + \delta v_r \frac{\partial v_0}{\partial r}\hat{\boldsymbol{r}} + \frac{1}{\rho_0}\nabla\delta p + \frac{\delta\rho}{\rho_0^2}\frac{\partial p}{\partial r}\hat{\mathbf{r}} &= 0, \\
\left(\frac{\partial}{\partial t} + v_0\frac{\partial}{\partial r}\right)\left(\frac{\delta p}{p_0} - \gamma\frac{\delta\rho}{\rho_0}\right) + \delta v_r \frac{\partial}{\partial r}\log\left(\frac{p_0}{\rho_0^\gamma}\right) &= 0.
\end{aligned} \tag{3.16}$$

Note that in Eqn. (3.16), all the unperturbed variables obey the hydrodynamic equations (Eqn. (3.9)). Now we normalize our perturbations as before

$$\begin{aligned}
\delta\tilde{\mathbf{v}} &\equiv \frac{\delta\mathbf{v}}{v_2}, \\
\delta\tilde{\rho} &\equiv \frac{\delta\rho}{\rho_2}, \\
\delta\tilde{p} &\equiv \frac{\delta p}{p_2},
\end{aligned} \tag{3.17}$$

and insert into Eqn. (3.16) to obtain

$$\begin{aligned}
(\gamma+1)t\frac{\partial\delta\tilde{\rho}}{\partial t}+\frac{\partial\tilde{v}}{\partial\tilde{r}}\delta\tilde{\rho}+\tilde{v}\frac{\partial\delta\tilde{\rho}}{\partial\tilde{r}}+\frac{\partial\tilde{\rho}}{\partial\tilde{r}}\delta\tilde{v}_r+\frac{\tilde{v}}{\tilde{r}}\delta\tilde{\rho}+\frac{\tilde{\rho}}{\tilde{r}}\delta\tilde{v}_r \\
+\tilde{\rho}\tilde{\nabla}\cdot\delta\tilde{\mathbf{v}}=0, \\
(\gamma+1)t\frac{\partial\delta\tilde{\mathbf{v}}}{\partial t}-\frac{\gamma+1}{2}\delta\tilde{\mathbf{v}}+\tilde{v}\frac{\partial\delta\tilde{\mathbf{v}}}{\partial\tilde{r}}+\frac{\partial\tilde{v}}{\partial\tilde{r}}\delta\tilde{v}_r\hat{\mathbf{r}} \\
+\frac{\gamma-1}{2}\frac{1}{\tilde{\rho}}\tilde{\nabla}\delta\tilde{p}-\frac{\gamma-1}{2}\frac{1}{\tilde{\rho}^2}\frac{\partial\tilde{p}}{\partial\tilde{r}}\delta\tilde{\rho}\hat{\boldsymbol{r}}=0, \\
(\gamma+1)t\frac{1}{\tilde{p}}\frac{\partial\delta\tilde{p}}{\partial t}-(\gamma+1)t\frac{1}{\tilde{p}^2}\frac{\partial\tilde{p}}{\partial t}\delta\tilde{p}-\gamma(\gamma+1)t\frac{1}{\tilde{\rho}}\frac{\partial\delta\tilde{\rho}}{\partial t}+\gamma(\gamma+1)t\frac{1}{\tilde{\rho}^2}\frac{\partial\tilde{\rho}}{\partial t}\delta\tilde{\rho} \\
+\frac{\tilde{v}}{\tilde{p}}\frac{\partial\delta\tilde{p}}{\partial\tilde{r}}-\frac{\tilde{v}}{\tilde{p}^2}\frac{\partial\tilde{p}}{\partial\tilde{r}}\delta\tilde{p}-\gamma\frac{\tilde{v}}{\tilde{\rho}}\frac{\partial\delta\tilde{\rho}}{\partial\tilde{r}}+\gamma\frac{\tilde{v}}{\tilde{\rho}^2}\frac{\partial\tilde{\rho}}{\partial\tilde{r}}\delta\tilde{\rho}+\frac{1}{\tilde{p}}\frac{\partial\tilde{p}}{\partial\tilde{r}}\delta\tilde{v}_r \\
-\gamma\frac{1}{\tilde{\rho}}\frac{\partial\tilde{\rho}}{\partial\tilde{r}}\delta\tilde{v}_r=0.
\end{aligned} \tag{3.18}$$

In Eqn.(3.18), we used the relations

$$\begin{aligned}
v_2&=\frac{1}{\gamma+1}\frac{r_2}{t}\propto t^{-1/2}, \\
\rho_2&=\frac{\gamma+1}{\gamma-1}\rho_1, \\
p_2&=\frac{\rho_1}{2(\gamma+1)}\frac{r_2^2}{t^2}.
\end{aligned} \tag{3.19}$$

which come from the jump conditions. Note that

$$\frac{\partial}{\partial r}=\frac{\partial\tilde{r}}{\partial r}\frac{\partial}{\partial\tilde{r}}=\frac{1}{r_2}\frac{\partial}{\partial\tilde{r}}, \tag{3.20}$$

and the normalized spatial derivative is

$$\tilde{\nabla}\equiv\frac{\partial}{\partial\tilde{r}}\hat{\mathbf{r}}+\frac{1}{\tilde{r}}\frac{\partial}{\partial\phi}\hat{\boldsymbol{\phi}}+r_2\frac{\partial}{\partial z}\hat{\mathbf{z}}. \tag{3.21}$$

The normalized variables $\tilde{v}$, $\tilde{p}$, and $\tilde{\rho}$ are self-similar and is a function of a single normalized similarity parameter $\tilde{r}$:

$$\begin{aligned}\tilde{v} &= \tilde{v}(\tilde{r}),\\ \tilde{p} &= \tilde{p}(\tilde{p}),\\ \tilde{\rho} &= \tilde{\rho}(\tilde{\rho}).\end{aligned} \tag{3.22}$$

Therefore, we can assume that the normalized perturbation variables can be expanded by a similarity term (a function of only a similarity parameter $\tilde{r}$), the longitudinal spatial dependence as a Fourier series (we are assuming an azimuthally symmetric blast wave with longitudinal "ripples"), and a power-law temporal dependence:

$$\begin{aligned}\delta\tilde{\mathbf{v}}(\tilde{r},z,t) &= \delta\tilde{v}_r(\tilde{r})e^{ikz}t^s\hat{\mathbf{r}} + \delta\tilde{v}_z(\tilde{r})e^{ikz}t^s\hat{\mathbf{z}},\\ \delta\tilde{\rho}(\tilde{r},z,t) &= \delta\tilde{\rho}(\tilde{r})e^{ikz}t^s,\\ \delta\tilde{p}(\tilde{r},z,t) &= \delta\tilde{p}(\tilde{r})e^{ikz}t^s.\end{aligned} \tag{3.23}$$

Since a cylindrical blast wave expands as $r_2 \propto t^{1/2}$, the time derivatives of Eqn. (3.22) and Eqn. (3.23) are

$$\begin{aligned}\frac{\partial\tilde{v}}{\partial t} &= -\frac{1}{2}\frac{\tilde{r}}{t}\frac{\partial\tilde{v}}{\partial\tilde{r}},\\ \frac{\partial\tilde{\rho}}{\partial t} &= -\frac{1}{2}\frac{\tilde{r}}{t}\frac{\partial\tilde{\rho}}{\partial\tilde{r}},\\ \frac{\partial\tilde{p}}{\partial t} &= -\frac{1}{2}\frac{\tilde{r}}{t}\frac{\partial\tilde{p}}{\partial\tilde{r}},\end{aligned} \tag{3.24}$$

and

$$\begin{aligned}
\frac{\partial \delta\tilde{\mathbf{v}}}{\partial t} &= -\frac{1}{2}\frac{\tilde{r}}{t}\frac{\partial \delta\tilde{\mathbf{v}}}{\partial \tilde{r}} + \frac{s}{t}\delta\tilde{\mathbf{v}}, \\
\frac{\partial \delta\tilde{\rho}}{\partial t} &= -\frac{1}{2}\frac{\tilde{r}}{t}\frac{\partial \delta\tilde{\rho}}{\partial \tilde{r}} + \frac{s}{t}\delta\tilde{\rho}, \\
\frac{\partial \delta\tilde{p}}{\partial t} &= -\frac{1}{2}\frac{\tilde{r}}{t}\frac{\partial \delta\tilde{p}}{\partial \tilde{r}} + \frac{s}{t}\delta\tilde{p}.
\end{aligned} \tag{3.25}$$

As a final step, we insert Eqns. (3.23), (3.24), and (3.25) into Eqn. (3.18) and obtain the similarity form of the perturbation equations

$$\begin{aligned}
&\tilde{\rho}\frac{d\delta\tilde{v}_r}{d\tilde{r}} - \left(\frac{\gamma+1}{2}\tilde{r} - \tilde{v}\right)\frac{d\delta\tilde{\rho}}{d\tilde{r}} + \left(\frac{\tilde{\rho}}{\tilde{r}} + \frac{d\tilde{\rho}}{d\tilde{r}}\right)\delta\tilde{v}_r + \left[(\gamma+1)s + \frac{\tilde{v}}{\tilde{r}} + \frac{d\tilde{v}}{d\tilde{r}}\right]\delta\tilde{\rho} \\
&\qquad\qquad + ikr\frac{\tilde{\rho}}{\tilde{r}}\delta\tilde{v}_z = 0, \\
&\left(\tilde{v} - \frac{\gamma+1}{2}\tilde{r}\right)\tilde{\rho}\frac{d\delta\tilde{v}_r}{d\tilde{r}} + \frac{\gamma-1}{2}\frac{d\delta\tilde{p}}{d\tilde{r}} + \left[\frac{\gamma+1}{2}(2s-1) + \frac{d\tilde{v}}{d\tilde{r}}\right]\tilde{\rho}\delta v_r \\
&\qquad\qquad - \frac{\gamma-1}{2}\frac{1}{\tilde{\rho}}\frac{d\tilde{p}}{d\tilde{r}}\delta\tilde{\rho} = 0, \\
&\left(\tilde{v} - \frac{\gamma+1}{2}\right)\tilde{\rho}\frac{d\delta\tilde{v}_z}{d\tilde{r}} + ikr\frac{\gamma-1}{2}\frac{1}{\tilde{r}}\delta\tilde{p} + \frac{\gamma+1}{2}(2s-1)\tilde{\rho}\delta\tilde{v}_z = 0, \\
&\gamma\left(\frac{\gamma+1}{2}\tilde{r} - \tilde{v}\right)\frac{d\delta\tilde{\rho}}{d\tilde{r}} - \frac{\tilde{\rho}}{\tilde{p}}\left(\frac{\gamma+1}{2}\tilde{r} - \tilde{v}\right)\frac{d\delta p}{d\tilde{r}} - \left(\gamma\frac{1}{\tilde{\rho}}\frac{d\tilde{\rho}}{d\tilde{r}} - \frac{1}{\tilde{p}}\frac{d\tilde{p}}{d\tilde{r}}\right)\tilde{\rho}\delta\tilde{v}_r \\
&\qquad - \gamma\left[(\gamma+1)s + \left(-\frac{\gamma+1}{2}\tilde{r} - \tilde{v}\right)\frac{1}{\tilde{\rho}}\frac{d\tilde{\rho}}{d\tilde{r}}\right]\delta\tilde{\rho} \\
&\qquad + \frac{\tilde{\rho}}{\tilde{p}}\left[(\gamma+1)s + \left(\frac{\gamma+1}{2}\tilde{r} - \tilde{v}\right)\frac{1}{\tilde{p}}\right]\delta\tilde{p} = 0.
\end{aligned} \tag{3.26}$$

For notational simplicity, explicit functional dependence of the perturbed quantities have been taken out, for example, $\delta\tilde{v}_r = \delta\tilde{v}_r(\tilde{r})$ and not $\delta\tilde{v}_r(\tilde{r}, z, t)$,

in the above equations.

To solve Eqn. (3.26), we need appropriate boundary conditions. The gas flow across the perturbed shock front obeys the conservation laws and is expressed as

$$\begin{aligned}
[\rho u_r] &= 0, \\
\left[p + \rho u_r^2\right] &= 0, \\
[u_z] &= 0, \\
\left[\frac{1}{2}u^2 + \frac{\gamma}{\gamma-1}\frac{p}{\rho}\right] &= 0,
\end{aligned} \tag{3.27}$$

where u_r is the component of the gas velocity relative to and normal to the shock front and u_z is the tangential component. The square brackets denote the difference of the enclosed quantities across the shock front. Linearizing Eqn. (3.27) about perturbations, we have

$$\left(\delta\rho + \eta\frac{\partial\rho_0}{\partial r}\right)(v_0 - u_1) + \rho_0\left(\delta v_r + \eta\frac{\partial v_0}{\partial r} - \frac{d\eta}{dt}\right) = -\rho_1\frac{d\eta}{dt},$$

$$\left(\delta p + \eta\frac{\partial p_0}{\partial r}\right) + \left(\delta\rho + \eta\frac{\partial\rho_0}{\partial r}\right)(v_0 - u_1)^2 + 2\rho_0(v_0 - u_1)\left(\delta v_r + \eta\frac{\partial v_0}{\partial r} - \frac{d\eta}{dt}\right) = 2\rho_1 u_1\frac{d\eta}{dt},$$

$$(v_0 - u_1)\left(\delta v_r + \eta\frac{\partial v_0}{\partial r} - \frac{d\eta}{dt}\right) + \frac{\gamma}{\gamma-1}\frac{1}{\rho_0}\left(\delta p + \eta\frac{\partial p_0}{\partial r}\right) - \frac{\gamma}{\gamma-1}\frac{p_0}{\rho_0^2}\left(\delta\rho + \eta\frac{\partial\rho_0}{\partial r}\right) = u_1\frac{d\eta}{dt}, \tag{3.28}$$

where η is the perturbation of the shock front position. Again, normalizing to

the values at the shock front

$$\tilde{\eta} \equiv \frac{\eta}{r_2} \tag{3.29}$$

and likewise expanding it as

$$\tilde{\eta}(\tilde{r}, z, t) = \tilde{\eta}(\tilde{r}) e^{ikz} t^s, \tag{3.30}$$

our conditions become

$$\begin{aligned}
\left(\delta\tilde{\rho} + \tilde{\eta}\frac{d\tilde{\rho}}{d\tilde{r}}\right)\left(\frac{1-\gamma}{2}\right) + \left(\delta\tilde{v}_r + \frac{d\tilde{v}}{d\tilde{r}}\right) &= 2\eta(s+1/2) \\
-\frac{1}{2}\left(\delta\tilde{p} + \tilde{\eta}\frac{d\tilde{p}}{d\tilde{r}}\right) + \left(\frac{1-\gamma}{2}\right)\left(\delta\tilde{\rho} + \tilde{\eta}\frac{d\tilde{\rho}}{d\tilde{r}}\right) + \left(\delta\tilde{v}_r + \tilde{\eta}\frac{d\tilde{v}}{d\tilde{r}}\right) &= 0 \\
(1-\gamma)\left(\delta\tilde{v}_r + \tilde{\eta}\frac{d\tilde{v}}{d\tilde{r}}\right) + \gamma\left(\delta\tilde{p} + \tilde{\eta}\frac{d\tilde{p}}{d\tilde{r}}\right) - \gamma\left(\delta\tilde{\rho} + \tilde{\eta}\frac{d\tilde{\rho}}{d\tilde{r}}\right) &= 2\gamma\tilde{\eta}(s+1/2).
\end{aligned} \tag{3.31}$$

Here we use the relations $\tilde{v}(1) = \tilde{\rho}(1) = \tilde{p}(1) = 1$ and $r = r_2 \propto t^{1/2}$. After some algebraic manipulations, we obtain the conditions at the shock front where $\tilde{r} = 1$:

$$\begin{aligned}
\delta\tilde{v}_r &= -\tilde{\eta}\frac{d\tilde{v}}{d\tilde{r}} + \tilde{\eta}(1+2s), \\
\delta\tilde{\rho} &= -\tilde{\eta}\frac{d\tilde{\rho}}{d\tilde{r}}, \\
\delta\tilde{p} &= -\tilde{\eta}\frac{d\tilde{p}}{d\tilde{r}} + \tilde{\eta}(2+4s).
\end{aligned} \tag{3.32}$$

We see that in Eqn. (3.32) $\tilde{\eta}$ is simply a scale factor which can be arbitrarily set to 1 for convenience. Lastly, consider the z-component of the gas flow velocity at $kr = \pi/2$; from condition $[u_z] = 0$, this becomes

$$u_z = \frac{2}{\gamma+1} u_1 \cos\theta \sin\theta, \tag{3.33}$$

where θ is the angle between the shock front surface and the $r = r_2$ plane at $kr = \pi/2$. With θ being small, this yields

$$\begin{aligned} \cos\theta &\approx 1, \\ \sin\theta &\approx k\tilde{\eta} = k, \end{aligned} \tag{3.34}$$

and our z-component gas velocity boundary condition becomes

$$\delta\tilde{v}_z = -ikr. \tag{3.35}$$

The condition at the origin is [23]

$$\delta p = 0. \tag{3.36}$$

To numerically solve the normalized perturbation equations, we first rearrange Eqn. (3.26) into matrix form

$$\mathbf{A} \cdot \frac{d\delta\tilde{\mathbf{Q}}}{d\tilde{\mathbf{r}}} = \mathbf{B} \cdot \delta\tilde{\mathbf{Q}}, \tag{3.37}$$

where

$$\delta\tilde{\mathbf{Q}} = \left[\delta\tilde{v}_r, \quad \delta\tilde{\rho}, \quad \delta\tilde{p}, \quad \delta\tilde{v}_z\right],$$

and $\mathbf{A}$ and $\mathbf{B}$ are the 4×4 matrices

$$\mathbf{A} = \begin{bmatrix} \tilde{\rho} & \left(-\frac{\gamma+1}{2}\tilde{r} + \tilde{v}\right) & 0 & 0 \\ \left(-\frac{\gamma+1}{2}\tilde{r} + v\right)\tilde{\rho} & 0 & \frac{\gamma-1}{2} & 0 \\ 0 & 0 & 0 & \left(-\frac{\gamma+1}{2}\tilde{r} + \tilde{v}\right)\tilde{\rho} \\ 0 & -\gamma\left(-\frac{\gamma+1}{2}\tilde{r} + \tilde{v}\right) & \frac{\tilde{\rho}}{\tilde{p}}\left(-\frac{\gamma+1}{2}\tilde{r} + \tilde{v}\right) & 0 \end{bmatrix},$$

$$\mathbf{B} = \left[\begin{array}{ccc} \left(\frac{d\tilde{\rho}}{d\tilde{r}} - \frac{\tilde{\rho}}{\tilde{r}}\right) & \left(\frac{\tilde{v}}{\tilde{r}} + \frac{d\tilde{v}}{d\tilde{r}} - (\gamma+1)s\right) & \cdots \\ \left(\frac{\gamma+1}{2}(1-2s) + \frac{d\tilde{v}}{d\tilde{r}}\right)\tilde{\rho} & \frac{\gamma-1}{2}\frac{1}{\tilde{\rho}}\frac{d\tilde{p}}{d\tilde{r}} & \cdots \\ 0 & 0 & \cdots \\ \left(\gamma\frac{1}{\tilde{\rho}} - \frac{1}{\tilde{p}}\frac{d\tilde{p}}{d\tilde{r}}\right) & \gamma\left((\gamma+1)s + \left(\frac{\gamma+1}{2}\tilde{r} + \tilde{v}\right)\frac{1}{\tilde{\rho}}\frac{d\tilde{\rho}}{d\tilde{r}}\right) & \cdots \end{array}\right.$$

$$\left.\begin{array}{ccc} \cdots & \left(\frac{d\tilde{\rho}}{d\tilde{r}} - \frac{\tilde{\rho}}{\tilde{r}}\right) & \left(\frac{\tilde{v}}{\tilde{r}} + \frac{d\tilde{v}}{d\tilde{r}} - (\gamma+1)s\right) \\ \cdots & \left(\frac{\gamma+1}{2}(1-2s) + \frac{d\tilde{v}}{d\tilde{r}}\right)\tilde{\rho} & \frac{\gamma-1}{2}\frac{1}{\tilde{\rho}}\frac{d\tilde{p}}{d\tilde{r}} \\ \cdots & 0 & 0 \\ \cdots & \left(\gamma\frac{1}{\tilde{\rho}} - \frac{1}{\tilde{p}}\frac{d\tilde{p}}{d\tilde{r}}\right) & \gamma\left((\gamma+1)s + \left(\frac{\gamma+1}{2}\tilde{r} + \tilde{v}\right)\frac{1}{\tilde{\rho}}\frac{d\tilde{\rho}}{d\tilde{r}}\right) \end{array}\right] .$$

Now we invert the matrix $\mathbf{A}$ and multiply both sides of Eqn. (3.37) such that it becomes

$$\begin{aligned} \frac{d\delta\tilde{\mathbf{Q}}}{d\tilde{\mathbf{r}}} &= (\mathbf{A}^{-1}\cdot\mathbf{B})\cdot\delta\tilde{\mathbf{Q}} \\ &= \mathbf{C}\cdot\delta\tilde{\mathbf{Q}}. \end{aligned} \tag{3.38}$$

The numerical calculations are performed by a finite difference formula [23]

$$\frac{d\delta\tilde{\mathbf{Q}}}{d\tilde{\mathbf{r}}} = \frac{\delta\tilde{\mathbf{Q}}(\tilde{x}+h) - \delta\tilde{\mathbf{Q}}(\tilde{x})}{h}, \tag{3.39}$$

where h is an arbitrarily small value. For a given value of γ and kr, a value for s is guessed and the equations numerically integrated from $\tilde{x} = 1$ to $\tilde{x} = 0$

in steps of h. The results are checked to see how it matches the boundary conditions and if not, then s is modified to $s + \Delta s$ with Δs given by

$$\Delta s = -\frac{\delta\tilde{p}(\tilde{x}=0)}{\partial\delta\tilde{p}(\tilde{x}=0)/\delta s}, \tag{3.40}$$

and $\partial\delta\tilde{p}/\partial s$ calculated by

$$\frac{d}{d\tilde{x}}\frac{\partial\delta\tilde{\mathbf{Q}}}{\partial s} = \frac{\partial\mathbf{C}}{\partial s}\cdot\delta\tilde{\mathbf{Q}} + \mathbf{C}\cdot\frac{\partial\delta\tilde{\mathbf{Q}}}{\partial s}. \tag{3.41}$$

The iterations are continued until $\Delta s \leq 10^{-4}$. In this analysis, s is a complex number and the real part gives the rate at which perturbations decay or grow. The imaginary part gives the frequency of oscillations. The objective of our experiments were to measure the decay rate of perturbations and are mainly concerned with the $Re[s]$. Fig. (3.5) shows the results of this calculations, for several values of γ.

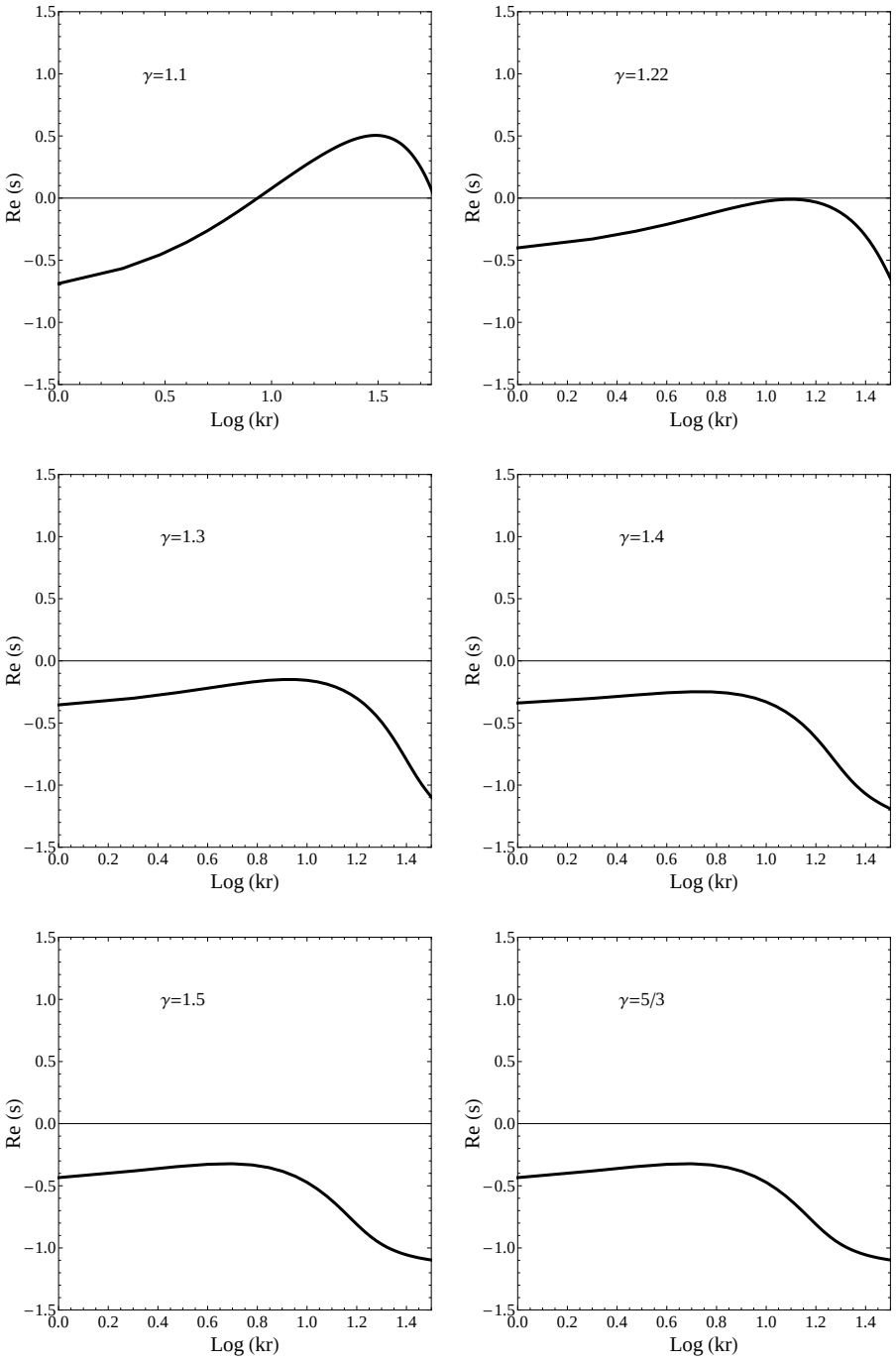

Figure 3.5: The temporal power law index s for several values of γ as a function of $\mathrm{Log}\,(kr)$

These calculations show that for $\gamma \leq 1.22$ there are longitudinal modes for which s is positive, or overstable: the amplitude of perturbations with these modes will exhibit growth. The plots would imply that the quantity kr remains fixed, that is, as the blast wave propagates, the wavelengths grow to keep kr constant. This, however, is not the case for perturbations in rectangular geometry (which is the case for an azimuthally symmetric blast wave with longitudinal ripples). The use of plotting as a function of kr is merely for convenience. Physically, a blast wave with a certain perturbation with wavenumber k will expand with the same k throughout its motion [24]. This is not the case for perturbations in polar geometry such as for spherical blast waves. As the radius expands, the wavelengths will diverge proportionately to keep mode number l constant. This aspect of cylindrical blast waves will be addressed in Ch. 5 in which experimental data is compared to theory.

Chapter 4

Experimental Setup and Diagnostics

Our experiments utilized a high intensity laser system to drive a cylindrical blast wave in a medium of atomic clusters for various gases. A small percentage of the beam was used to optically probe the blast wave at different times. Two separate optical diagnostics were used to measure the trajectory and electron density and the temporal evolution of perturbations on the blast wave. Previous experiments [25, 27, 28] used a small plastic pin target immersed in a gas to create the blast waves and an array of thin wires placed ahead to induce perturbations of a given wavelength, determined by the wire spacing. Because of the smaller spatial scales of our blast waves, use of a wire array was not a feasible option. Instead, we used a separate transverse beam to "machine" the cluster medium prior to the onset of the main drive beam. This transverse beam consists of a focused interferometric beam that has a spatial periodicity in the intensity to modify the cluster medium ahead of time. Since clusters are very effective at absorbing laser energy, the resulting blast wave exhibited a periodic longitudinal structure that served as the induced perturbation.

4.1 Laser System

Our experiments were conducted on the **G**lass **H**ybrid **O**ptical Parametric Chirped Pulse Amplification **S**cale **T**estbed (**GHOST**) Laser System at the University of Texas at Austin. This laser is a multi-terawatt system that fires a 150 fs pulse centered at 1054 nm with a peak energy of 2J that was initially developed as a scaled testbed for the Texas Petawatt Laser. Unlike titanium-sapphire lasers, this system uses a hybrid of doped glass as a gain medium to deliver the pulse. The front end of the laser consists of a commercial mode-locked oscillator that delivers short, low energy, laser pulses. The initial low energy beam is sent to a set of optical gratings that stretches the pulses in time such that subsequent amplification does not damage optical elements along the way. This stretched pulse is initially amplified by two sets of two BBO crystals pumped by a commercial 532nm PRO laser. The energy of the pulses after this initial amplification is around 30 mJ. After a set of spatial filters to clean up the beam, it is sent to a series of two hybrid glasses for final amplification before entering the compression chamber. The compression chamber has a set of optical gratings that works in reverse to the stretcher to compress the beam in time before entering the experimental chamber.

4.2 Experimental Apparatus

Our blast wave experiments required the use of three separate laser beams to deliver the main drive pulse, optical probes, and a transverse machining beam. The drive/pump beam is the most energetic of the three. The

other two beams require less energy and was acquired by use of beam splitters inside the experimental chamber. Previous blast wave experiments conducted on the THOR laser system [30] took a fraction of the uncompressed main beam beforehand and utilized a separate air compressor for use as the probe and machining beam. This air compressor was a set of optical gratings much like that inside the compression chamber but on a smaller scale. An additional vacuum chamber was not necessary because of the low energy of this split-off beam making it less prone to self-focusing and other nonlinear optical effects [29]. The intensity requirements of the machining beam and short pulse duration of the probe beam, however, still required optical compression. A probe pulse in the nanoseconds range is undesirable because a blast wave can expand significantly in this time period and thus "smear" out the images. The limited geometry of the GHOST laser facility, however, did not allow for a separate air compressor to be used as a source for these two beams. Instead, the main beam from the vacuum compressor was split into all three inside our experimental chamber. Fig. (4.1) shows a Solidworks drawing of the main experimental chamber and the various beams made during the initial design phase of the experiment.

The compressed beam enters the experimental chamber from the compressor and is sent through a series of two beam splitters. The first is a 65/35 (reflection/transmission) beam splitter (BS1) that directs the more energetic 65% beam to a spherical 45" focal length mirror. This mirror produces a 30 μm diameter beam focused underneath the supersonic gas jet and serves as our

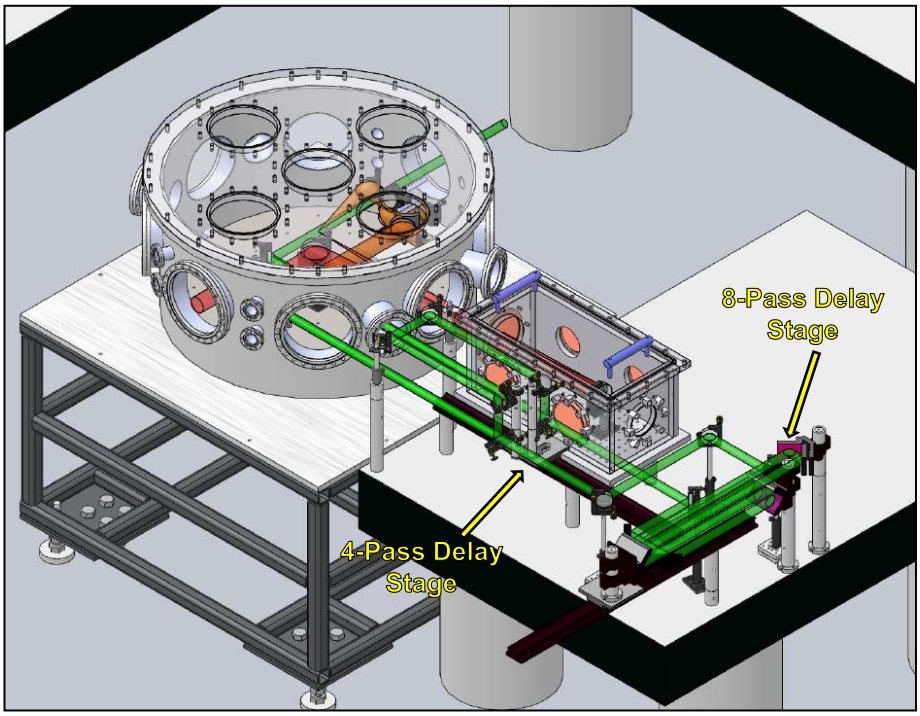

Figure 4.1: Solidworks drawing of the experimental apparatus. The separate beams are designated by the following color scheme: Red - Drive/Pump Beam, Green - Optical Probe Beam, Orange - Machining Beam

drive/pump beam. The remaining 35% is sent to the second 90/10 beamsplitter (BS2) that directs the 90% component to our optical machining assembly. The remaining 10% exits the chamber through a glass port and is routed to an optical delay stage to serve as our probe beam. Fig. (4.2) is a top-down view of the experimental chamber and beams. All three beams originate from inside the experimental chamber. The probe line reenters the chamber after traveling a distance based on time delay of interest by use of multipass optical delay stage.

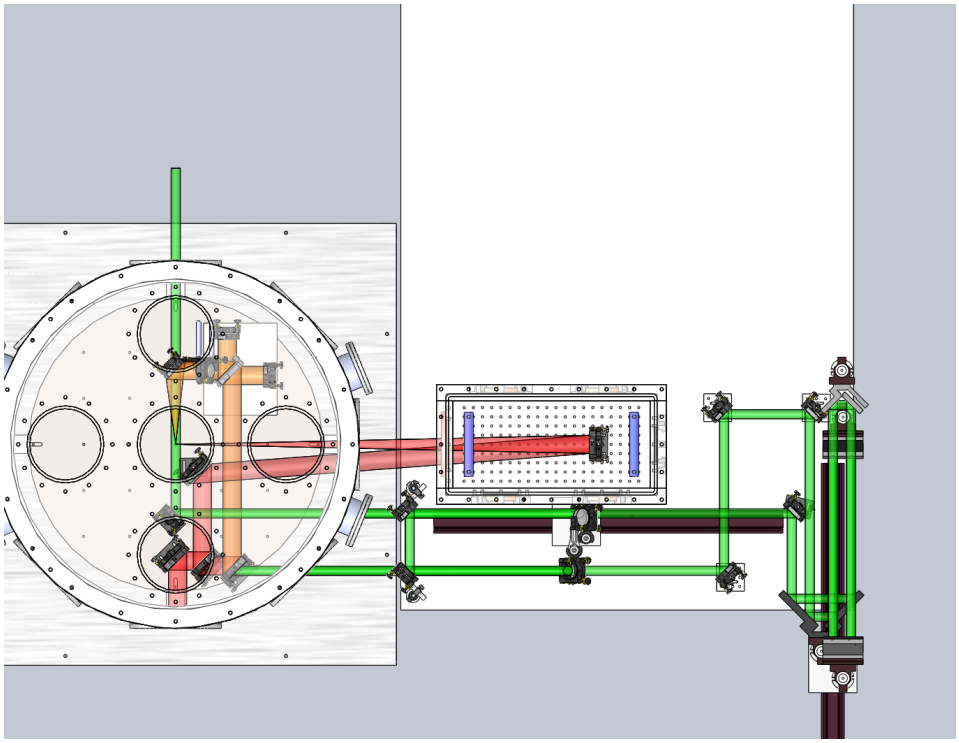

Figure 4.2: Top-down view of experimental chamber and the three beams. Color scheme is same as Fig. (4.1).

4.2.1 Pump Beam

The pump beam is produced by a 4" gold-coated spherical mirror with a focal length of 45". Such a long focal length was necessary because of the requirement that this beam arrive approximately ~ 2.5 ns after the machining beam modulates the cluster environment. We placed the spherical mirror inside a separate external chamber connected by steel bellows to position the focal spot just beneath the gas jet nozzle. With a $f/22$ spherical mirror, our peak intensity at the focus was on the order of 10^{17} W/cm^2. The Rayleigh

range of this beam is $\sim$ 2mm, consequently resulting in a blast wave of similar length. This proved to be a convenient size as our imaging diagnostics with a magnification of 2$\times$ imprinted an image that fit within the CCD chip. Fig. (4.3) shows an image of the experimental chamber.

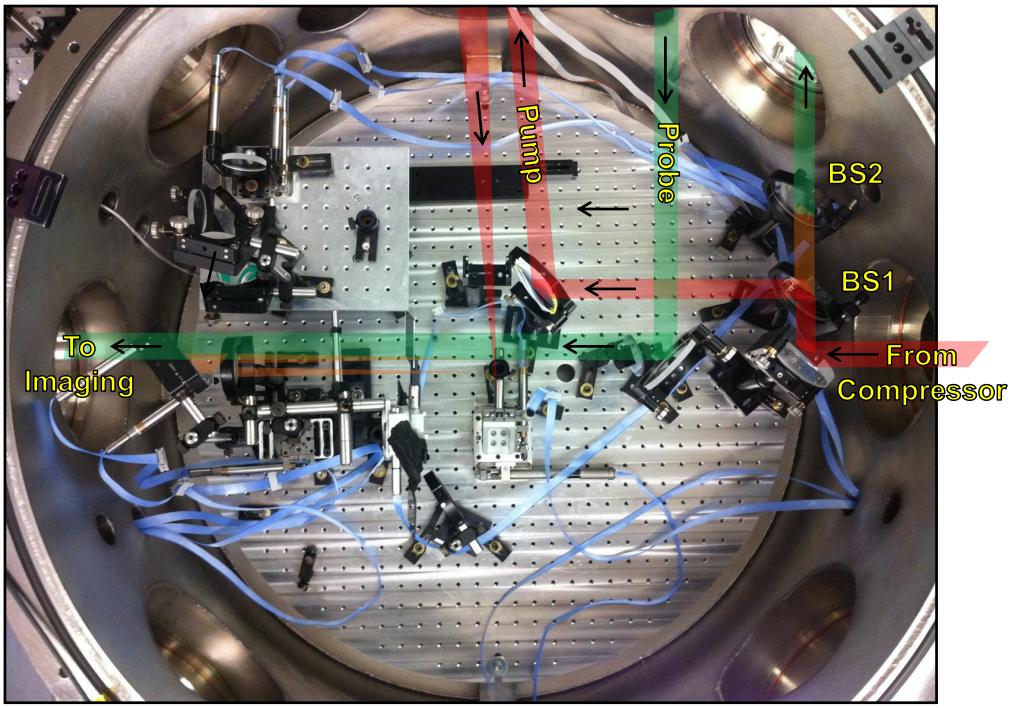

Figure 4.3: Top-down view of experimental chamber. BS1 and BS2 are the 65/35 and 90/10 beamsplitters, respectively.

4.2.2 Machining Beam

After passing through BS1, the remaining 35% of the beam is then routed to BS2 where 90% is reflected to our machining beam apparatus. This consists of a standard Michelson interferometer that produces interference

fringes which is then focused beneath our gas jet, perpendicularly and overlapping with the pump beam. This apparatus was placed inside our experimental chamber to fulfill the requirement that the cluster environment be modulated approximately 2 ns prior to the pump beam. Once the fringes are produced in the interferometer, it is routed upwards where it passes through a f = 30 cm convex spherical lens and a f = -70 cm cylindrical lens. The positive lens serves to focus down the entire beam at the gas jet location while the cylindrical lens spreads out the beam in the longitudinal direction. The periodic intensity profile of this beam, then, destroys clusters in the regions where the intensity is high such that the consequent blast wave is seeded with some perturbed structure. Fig. (4.4) shows directly imaged machining beams for two modulation wavelengths. The end mirror adjustments for path length and the two steering axes were connected to motors which allowed us to control the fringe spacing and contrast.

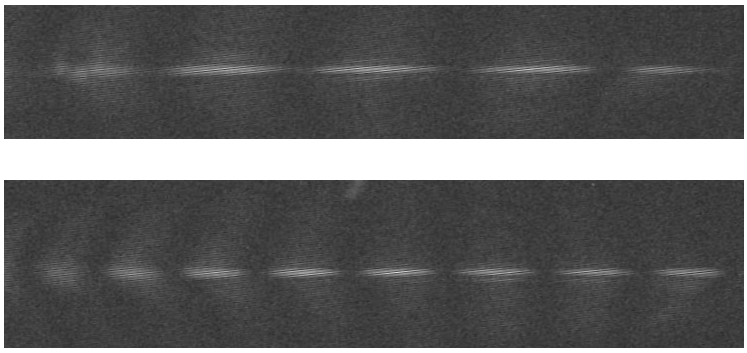

Figure 4.4: Sample image of machining beam at focus. The period of intensity fluctuations are controlled by slight steering adjustments of one of the interferometer end mirrors.

We used two separate diagnostics to ensure proper overlap of the machining and pump beam. We imaged the nozzle and pump beam in the axial direction and matched the machining beam focus accordingly. To overlap the two longitudinally, we imaged a fiducial at the pump beam focus and steered the machining beam to the same location. Lastly, as a final check, we shot blast waves with an imprinted modulation and made fine adjustments. Fig. (4.5) shows how the two diagnostics allowed us to align both beams in all three axes.

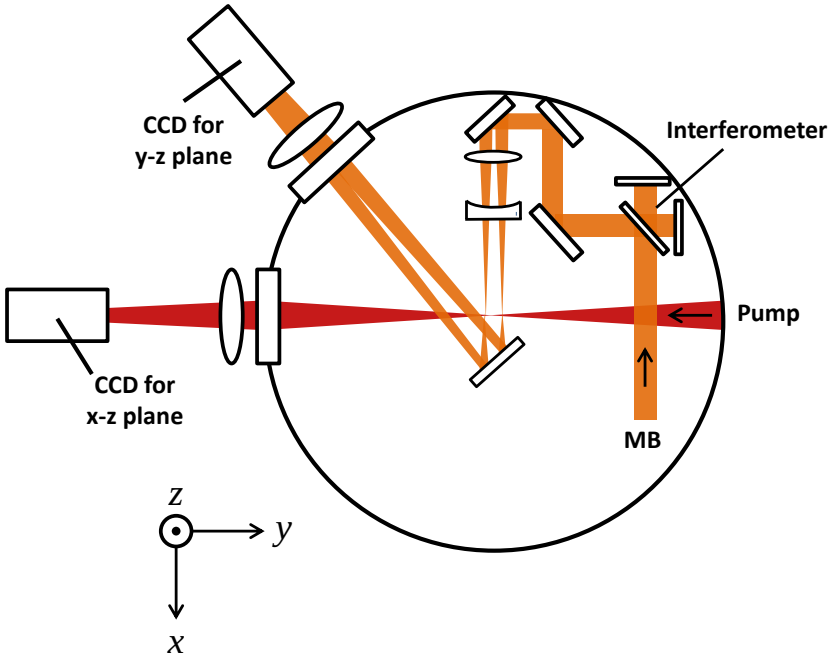

Figure 4.5: Schematic diagram of the chamber with the machining and pump beam diagnostics.

4.2.3 Probe Beam

We used an optical rail and a system of multipass mirrors to achieve the desired time delay between the pump and probe beams. The multipass mirror system consisted of a 4-pass and 8-pass delay stage for short and long time delays, respectively. The probe beam was the remaining 10% of transmitted light from BS2 that was sent outside of our chamber to the respective multipass systems and reentered the chamber to pass through the plasma filament. The 4-pass consists of four 45° mirrors on an optical rail to reflect the beam four times before reentering the chamber. The time delay was adjusted by moving the stage on the rail thereby lengthening or shortening the distance between passes. The entire 4-pass system was mounted on a magnetic base for easy removal when longer time delays were desired and the 8-pass system was used. We achieved a time delay of roughly -2 to 10 ns with the 4-pass stage while the 8-pass system allowed for time delays of 18 to 70 ns. The two systems did suffer the drawback of a delay gap between 10 to 18 ns. We calibrated the delay stages by measuring the difference in time between the pump and probe beams at the target location for various distances of the delay leg using a photodiode. Fig. (4.6) shows a sample plot of this calibration. The distance measured was between the front of the optical rail to an arbitrary point on the delay stage apparatus.

The probe beam reentered the chamber and passed orthogonally through the plasma filament. It was sent to a magnification 2× telescope consisting of an $f_1 = 30$ cm and $f_2 = 60$ cm convex lens. The f_1 lens was placed roughly 30

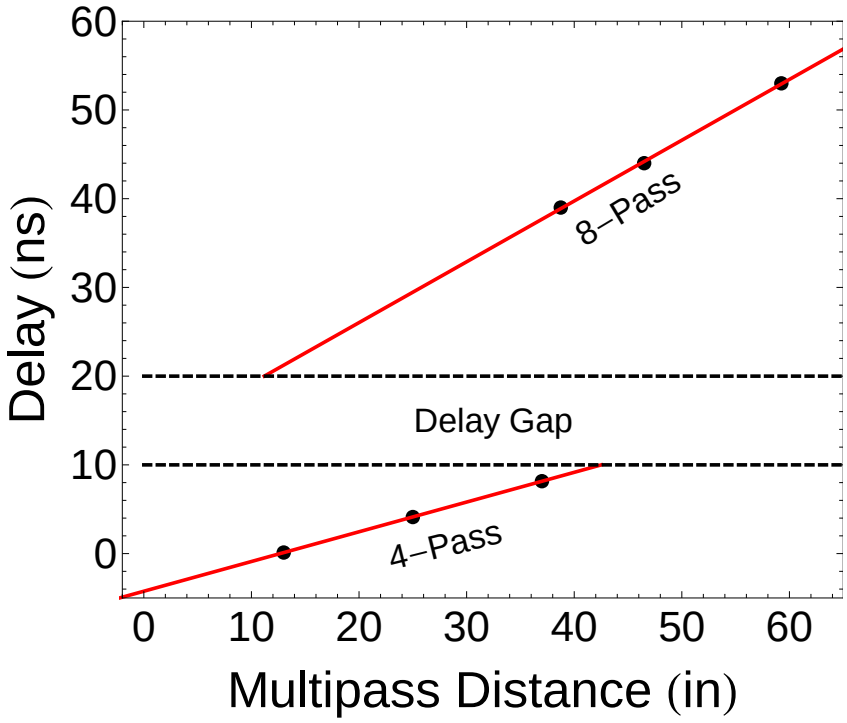

Figure 4.6: Time delay calibration. Error bars are obscured by the plot points.

cm from the plasma filament, f_2 roughly 90 cm from f_1, and lastly our CCD camera roughly 60 cm from f_2 giving us the desired magnification.

4.2.4 Gas Jet

We used a high pressure pulsed gas jet to produce clusters as our target media. Clusters are an ideal medium for these experiments because of their high efficiency in absorbing laser light [31–33]. The gas jet assembly was positioned on top of our experimental chamber and fitted with a 3-axis translation stage. The nozzle extended down from the ceiling of the chamber top and was

manipulated into place, roughly 3 mm above the pump beam focus.

Clusters form when a plume of gas is supersonically released into vacuum. The Van der Waals forces acts on the individual atoms to coalesce them into clusters. The number of atoms in a cluster, or the degree to which clusterization occurs, depends on the parameters of the gas jet such as opening angle and backing pressure. The average number of atoms in a cluster is given by [34, 35]

$$N_C = 100 \left(\frac{\Gamma^*}{1000} \right)^{1.8}, \tag{4.1}$$

where Γ^* is the Hagena parameter that is related to the nozzle characteristics and backing pressure as

$$\Gamma^* = k \frac{(d/\tan\alpha)^{0.85}}{T^{2.29}} P_0, \tag{4.2}$$

where d is the nozzle diameter (μm), α the opening half angle, T the temperature (Kelvin) before expansion, and P_0 the backing pressure (mbar) of the gas. k is a constant related to bond formation for a given gas [34, 36] and is listed for several gases in Table 4.1. We used a nozzle with a 790 μm diameter opening and an opening half angle of $\alpha = 5°$. The Γ^* values and cluster number densities for the several gases we used are summarized in Table (4.2). Clusterization begins for $\Gamma^* \geq 100 - 300$ and the cluster number density can

Table 4.1: k values for the Hagena parameter Γ^* for various gases

Gas	H_2	D_2	N_2	O_2	CO_2	CH_2	He	Ne	Ar	Kr	Xe
k	184	181	528	1400	3660	2360	3.85	185	1650	2890	5500

be calculated from dividing the atomic number density before clustering by the average number of atoms per cluster, $n_c \approx N_0/N_C$. The number density

Table 4.2: Γ^* values for the gases in our experiments. The backing pressure was 300, 800, and 1000 PSI for krypton, argon, and nitrogen, respectively.

Gas	Kr	Ar	N_2
Γ^*	470200	308800	188100
$N_C(\times 10^6)$	6.5	3.0	1.2

N_0 is calculated using the ideal gas law.

4.3 Imaging Diagnostics

We used two main imaging systems to obtain data for our blast wave experiments. The first was a schlieren or dark-field imaging systems that captures the image of a blast wave taking advantage of the large density gradient present at the shock front. The second method we used was optical interferometry. This method uses the change in the index of refraction due to ionized electrons to record the electron density landscape of the blast wave. This diagnostic not only captures the spatial information of the blast wave but whether ionization from radiative processes are present.

4.3.1 Schlieren Images

The schlieren technique involves using a pin or knife edge to obscure most of the undisturbed probe light and is sensitive to the first spatial derivative of the refractive index [37]. A plane parallel probe beam that passes

through a plasma slab will be refracted and deviate away from its normal path. An obstruction at the focal point of a lens in the imaging setup will obscure light that has been undeviated by the plasma and only the refracted beam will end up at the image plane. This results in bright areas on the image plane where large density gradients are present in our plasma slab. Fig. (4.7) illustrates this principle. The angle by which the beam is deflected is

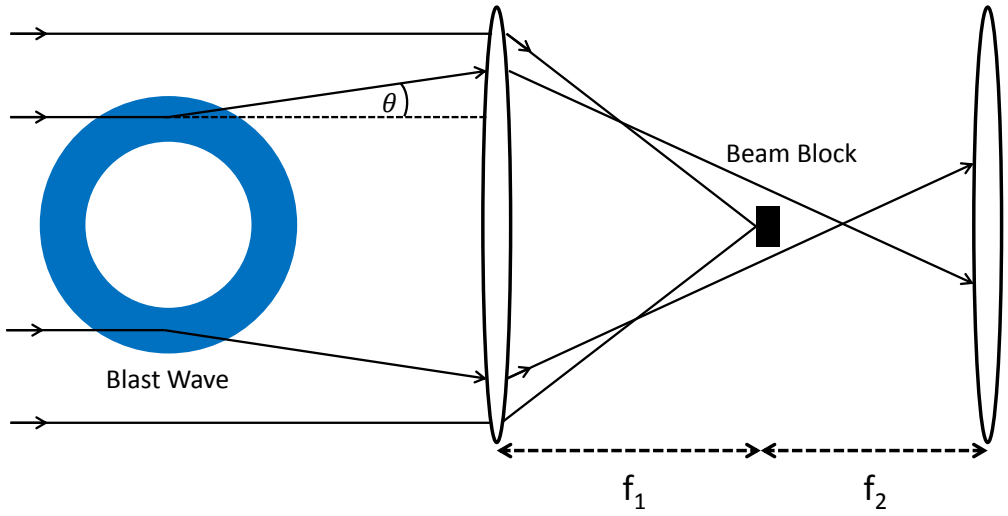

Figure 4.7: Undeivated light is obscured by a beam block or blade. Light that traverses a density gradient will be deflected past the block.

$$\theta = \frac{d}{dy} \int ndl, \tag{4.3}$$

where N is the index of refraction. In our experiments, we used a thin wire oriented in the horizontal direction to serve as our beam block. This diagnostic is useful in obtaining spatial information about the blast wave such as the small

scale perturbations induced on the shock surface. A sample image of a blast wave in krypton gas is shown in Fig. (4.8)

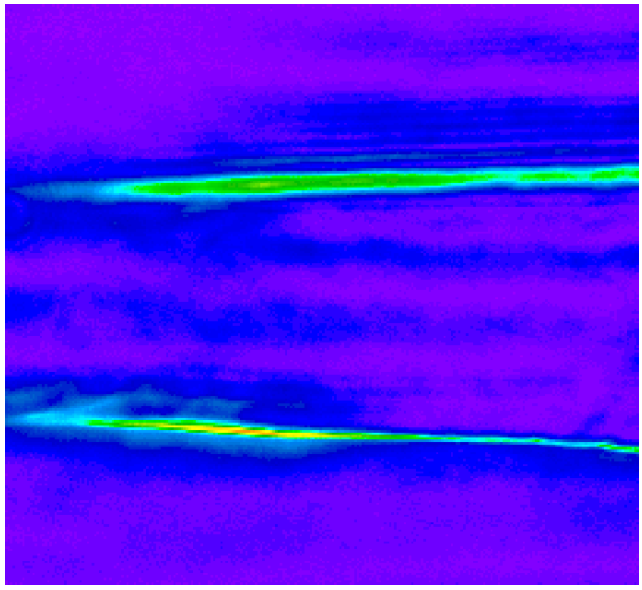

Figure 4.8: Schlieren image of a blast wave in krypton at 34 ns.

4.3.2 Interferometry

We also utilized a Michelson interferometer to obtain measurements of the electron density in our blast waves. This method also relies on the electron density dependence of the index of refraction through the phase shift induced on light [37].

The index of refraction of a plasma is given by

$$n^2 = 1 - \frac{\omega_p^2}{\omega^2} = 1 - \frac{N_e}{N_c}, \tag{4.4}$$

where

$$\omega_p^2 = \frac{N_e e^2}{\varepsilon_0 m_e} \tag{4.5}$$

is the plasma frequency, ω the angular frequency of the laser, and

$$N_c = \frac{\omega^2 m_e \varepsilon_0}{e^2} \tag{4.6}$$

is the critical density. m_e and e is the mass and charge of an electron, respectively, and N_e is the electron density that we seek to measure. Consider the two beams of an interferometer with phase difference ϕ in their electric fields

$$E_1(t) = E_1 \exp i\omega t \quad \text{and} \quad E_2(t) = E_2 \exp i(\omega t + \phi) \tag{4.7}$$

added together. The phase difference could be due to some slight misalignment of the two beams resulting in a different path length traversed by the two beams. The total field is then

$$E_{Tot} = (E_1 + E_2 \exp i\phi) \exp i\omega t, \tag{4.8}$$

and the intensity is

$$I = |E_{Tot}|^2 = [E_1^2 + E_2^2] \left[1 + \frac{2E_1 E_2}{E_1^2 + E_2^2} \cos\phi\right]. \tag{4.9}$$

Thus the output has a constant component and a periodic component that varies as $\cos\phi$. Since ϕ is dependent on the path length, what appears on the detector screen will be a series of bright and dark fringes. Any additional phase induced on the beam, for example, by a plasma filament will result in a shift in the fringes on the detector screen. If we assume that one arm of

the interferometer passes through the plasma, then the phase difference of this arm compared to the reference arm is

$$\Delta\phi = \int (n-1)\frac{\omega}{c}\, dl \tag{4.10}$$

Using Eq. (4.5) and (4.6), Eq. (4.10) becomes

$$\begin{aligned}\Delta\phi &= \frac{\omega}{c}\int \left[\left(1-\frac{N_e}{N_c}\right)^{1/2} - 1\right] dl \\ &= \frac{-\omega}{2cN_c}\int N_e\, dl,\end{aligned} \tag{4.11}$$

where we use the approximation $n \approx -\frac{1}{2}(N_e/N_c)$ which is valid if the plasma density is sufficiently small, i.e., $N_e \ll N_c$ [37].

To use this method in our experiments, we aligned the probe beam asymmetrically through the plasma filament such that only a portion of the beam passed through it. We then interfered this portion (the portion that contains the phase information) with a part of the beam that passed through undisturbed by the plasma. We used a rooftop mirror on one end of our interferometer to flip the image upon reflection such that upon recombination, the two halves of the probe beam can interfere with each other. Fig. (4.9) illustrates this diagnostic.

The raw interferometric images were first Fourier transformed to yield a phase map which we then applied an Abel inversion to extract a radial profile of the electron density. Fig. (4.10) is a sample interferometric image of a blast wave. The fringe pattern of Fig. (4.10) can be represented as a function of

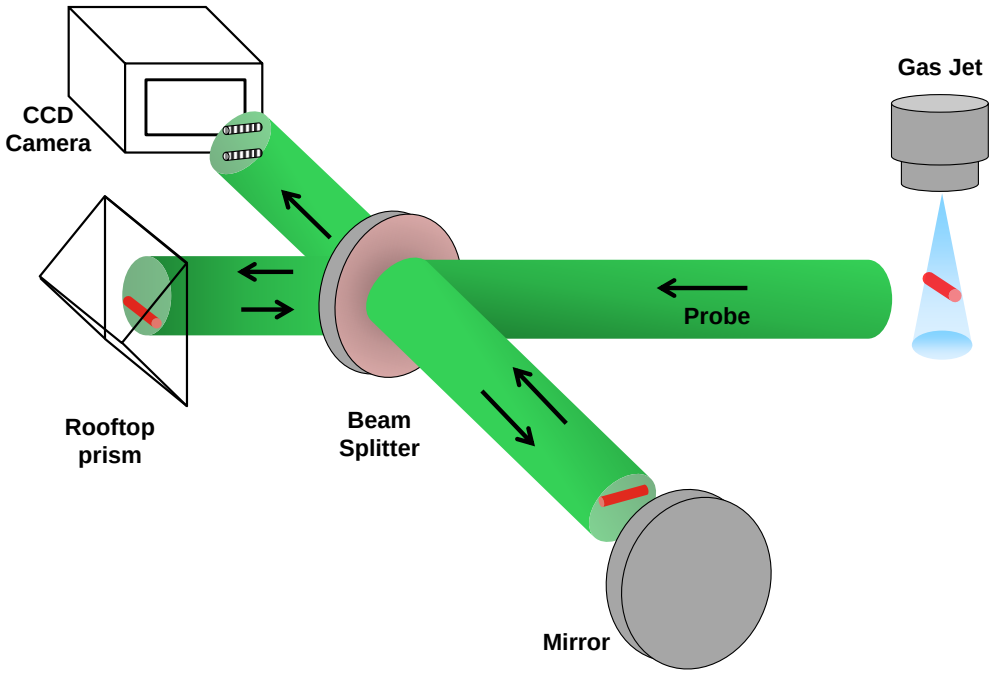

Figure 4.9: Illustration of inteferometry for measuring electron density.

the form

$$g(z,y) = a(z,y) + b(z,y)\cos[2\pi f_0 z + \phi(z,y)], \tag{4.12}$$

where $\phi(z,y)$ is the phase information of interest, $a(z,y)$ and $b(z,y)$ represent background intensity variations, and f_0 is the frequency of the fringe pattern [38]. For convenience, Eq. (4.12) is rewritten as

$$g(z,y) = a(z,y) + c(z,y)\exp(2\pi i f_0 z) + c^*(z,y)\exp(-2\pi i f_0 z), \tag{4.13}$$

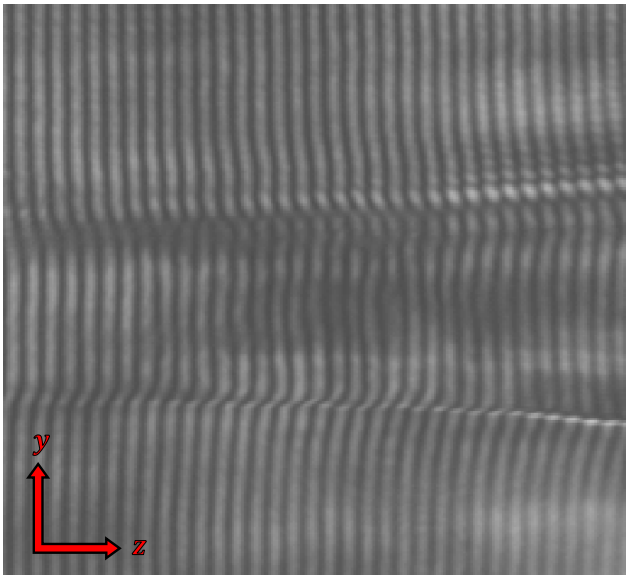

Figure 4.10: Interferometric image of a blast wave in krypton at 22 ns. Note the fringe shift at the shock front

with

$$c(z,y) = \frac{1}{2} b(z,y) \exp[i\phi(z,y)]. \tag{4.14}$$

Applying a Fourier transform on Eq. (4.13) with respect to the x direction yields

$$G(f,y) = A(f,y) + C(f - f_0, y) + C^*(f + f_0, y), \tag{4.15}$$

where f is the spatial frequency in the z direction. If $a(z,y)$, $b(z,y)$, and $\phi(z,y)$ vary slowly compared to f_0, then the Fourier spectra $A(f,y)$, $C(f-f_0,y)$, and $C^*(f+f_0,y)$ are separated by f_0 as shown in Fig. (4.11). We can thus filter out and isolate either of the two side peaks and translate it by f_0 to obtain $C(f,y)$. We next calculate the inverse Fourier transform with respect to f

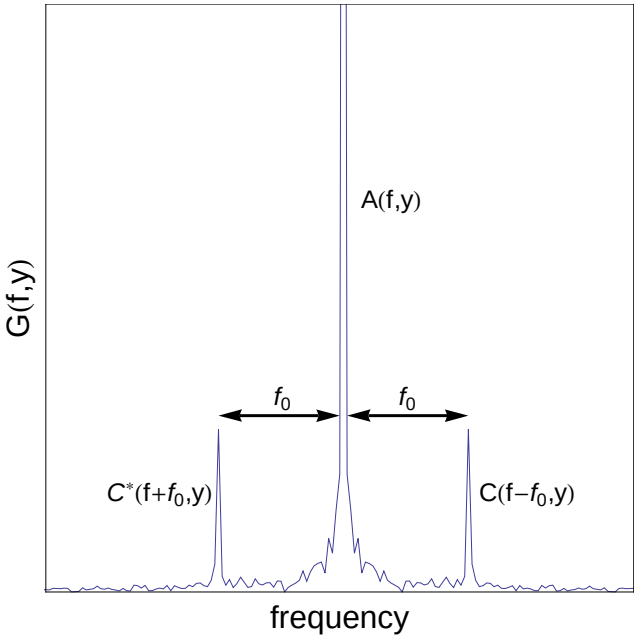

Figure 4.11: Sample Fourier spectrum of inteferogram of Fig. (4.10). The prominent peak in the center of the spectrum is the zero frequency term.

which yields $c(z, y)$, and take the logarithm giving us

$$\log[c(z, y)] = \log[(1/2)b(z, y)] + i\phi(z, y). \tag{4.16}$$

We do this for every line of our raw inteferometric image and construct a phase map of our blast wave.

The technique of Abel inversion requires that the quantity of interest is cylindrically symmetric which is a valid assumption of our blast wave [37]. At any given longitudinal position of our blast wave, we have the phase measurements which are chord integrals of the form

$$\phi(y) = \int_{-\sqrt{(a^2-y^2)}}^{+\sqrt{(a^2-y^2}} \phi(r)dx \tag{4.17}$$

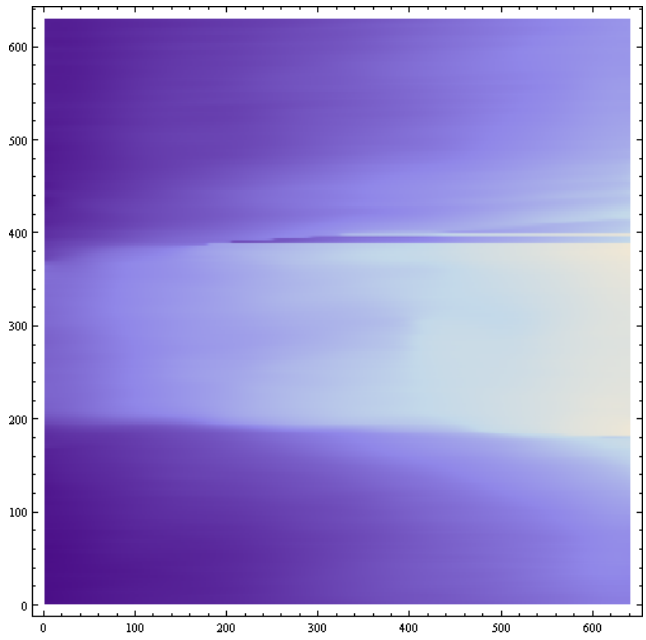

Figure 4.12: Phase map $\phi(z, y)$ of Fig. (4.10).

as illustrated in Fig. (4.13). We change Eq. (4.17) as an integral over r to yield

$$\phi(y) = 2\int_y^a \phi(r)\frac{rdr}{(r^2+y^2)^{1/2}} \tag{4.18}$$

and apply the Abel inversion which gives us

$$\phi(r) = -\frac{1}{\pi}\int_r^a \frac{d\phi(y)}{dy}\frac{dy}{(y^2-r^2)^{1/2}}. \tag{4.19}$$

This technique allows us to calculate the radial phase map based on a image that only has phase information on a projected two dimensional plane. With the phase as a function of radius r we use Eq. (4.11) to calculate the radial electron density profile

$$N_e(r) = N_c\frac{\lambda}{\pi^2}\phi(r). \tag{4.20}$$

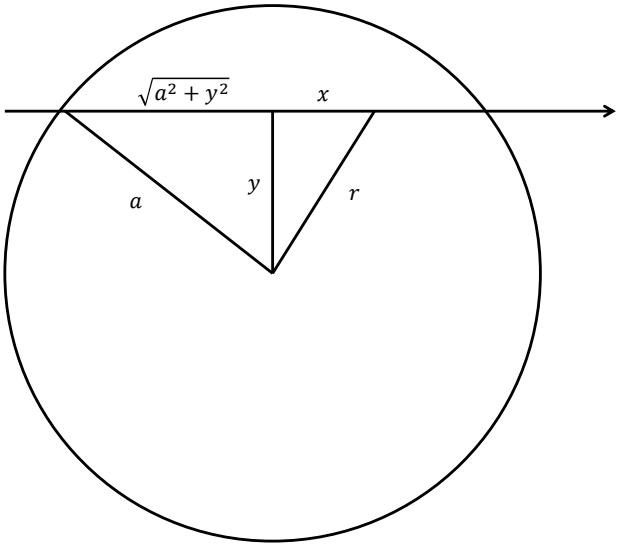

Figure 4.13: Chordal measurement diagram of phase map.

Fig. (4.14) shows the three dimensional plot of the electron density calculated from the phase map of Fig. (4.12).

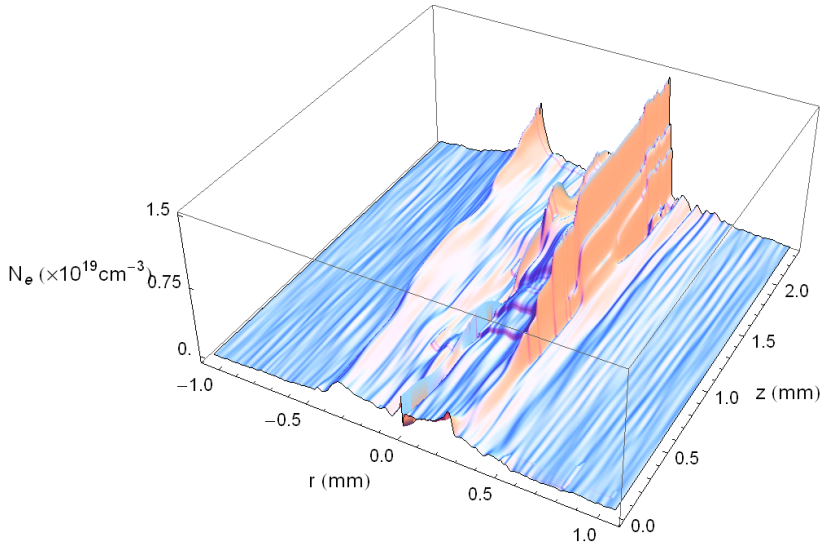

Figure 4.14: Electron density from phase map of Fig. (4.12)

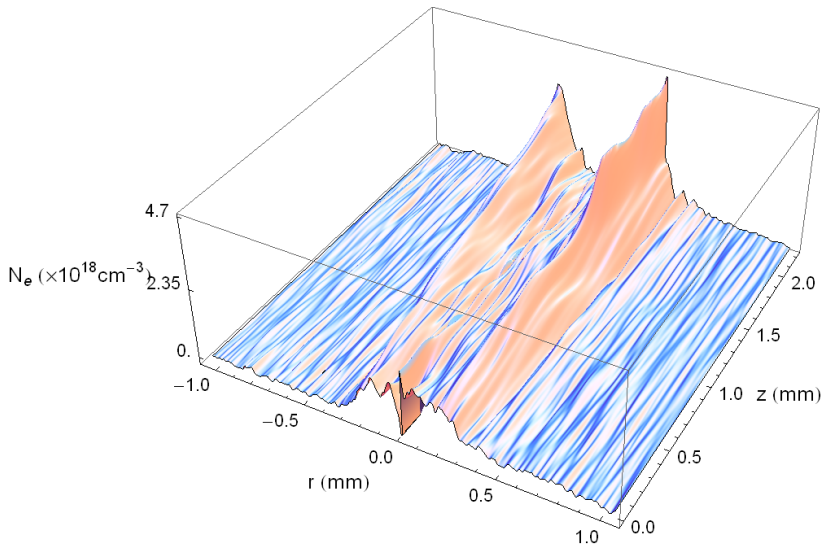

Figure 4.15: Electron density of krypton blast wave at 22 ns with 80 mJ of energy.

A line-out plot of the three dimensional graphs shown in Fig. (4.15) and (4.14) may be more useful in illuminating the features of the electron density profile as shown in Fig. (4.16).

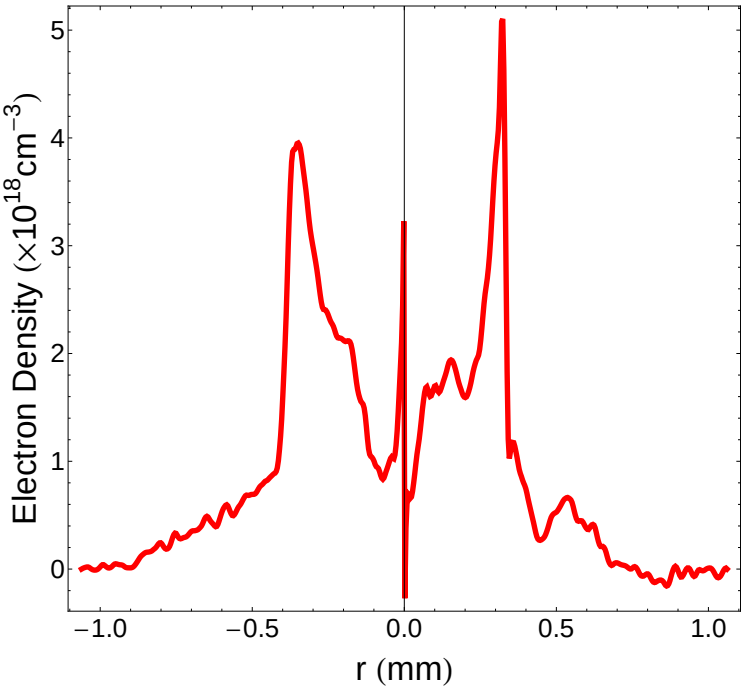

Figure 4.16: Line-out of electron density at $z \approx .5$ mm of Fig. (4.14).

Chapter 5

Experimental Results and Analysis

We performed several experimental campaigns to study the properties of radiative blast waves in several gases focusing particularly on the behavior of hydrodynamic instabilities. We first discuss the experimental results along with numerical simulations that show how radiative losses affect the evolution of blast waves. Lastly we examine and analyze the temporal behavior of perturbations induced on the surface of our blast waves.

5.1 Radiative Effects on Blast Wave Trajectory

As discussed in Ch.2, radiative losses from a blast wave surface will cause it to propagate with a smaller power-law index than the energy-conserving Sedov-Taylor value of 1/2 for a cylindrical blast wave. By measuring the trajectory, that is, how the radius changes over time, we are able ascertain whether a blast wave has suffered energy losses through radiation.

High Z gases exhibit more radiative losses because of the presence of more line emission in addition to bremsstrahlung as a means of radiation. Krypton was chosen as a target gas because of its relative high atomic number compared to argon but not as high as xenon as previously studied [39–41].

The first set of results are images of blast waves in krypton and argon for various drive energies. We operated the cluster gas jet with a backing pressure of 300 and 800 PSI for krypton and argon, respectively. These values were chosen based on calculations of the Hagena parameter discussed in Ch. 4. We acquired both Schlieren and interferometric images and traced out the edge of the blast wave by hand to measure its radius for the various time delays. Images of blast waves in krypton at various time delays are shown in Figs. (5.1) and (5.2). The radius measurements were taken at the position indicated in the figure. This position was chosen because the blast wave is not necessarily strictly cylindrical throughout its longitudinal length and exhibits some sphericity at or close to the location where the laser pulse first deposits its energy. These radius measurements were fit to a power law of the form

$$R(t) = A * t^n \tag{5.1}$$

with A and n as fitting parameters. Sample schlieren and inteferometric images for krypton are shown in Figs. (5.3)-(5.7). Figs. (5.3)-(5.7) are the radius vs. time data for krypton blast waves for different laser energies. Superimposed with the data are the fitting curves. The blast wave with a drive energy of 80 mJ (Fig. (5.3)) follows a more complicated trajectory than the rest. For this one, the data was divided into two segments, for the earlier and later times, and the regression analysis done separately for each. The lower deceleration parameter of $n = 0.12 \pm 0.01$ during the earlier phase suggest that the blast wave is initially strongly radiative and has not swept up enough mass to become self-similar and approach the Sedov-Taylor or sub-Sedov-Taylor

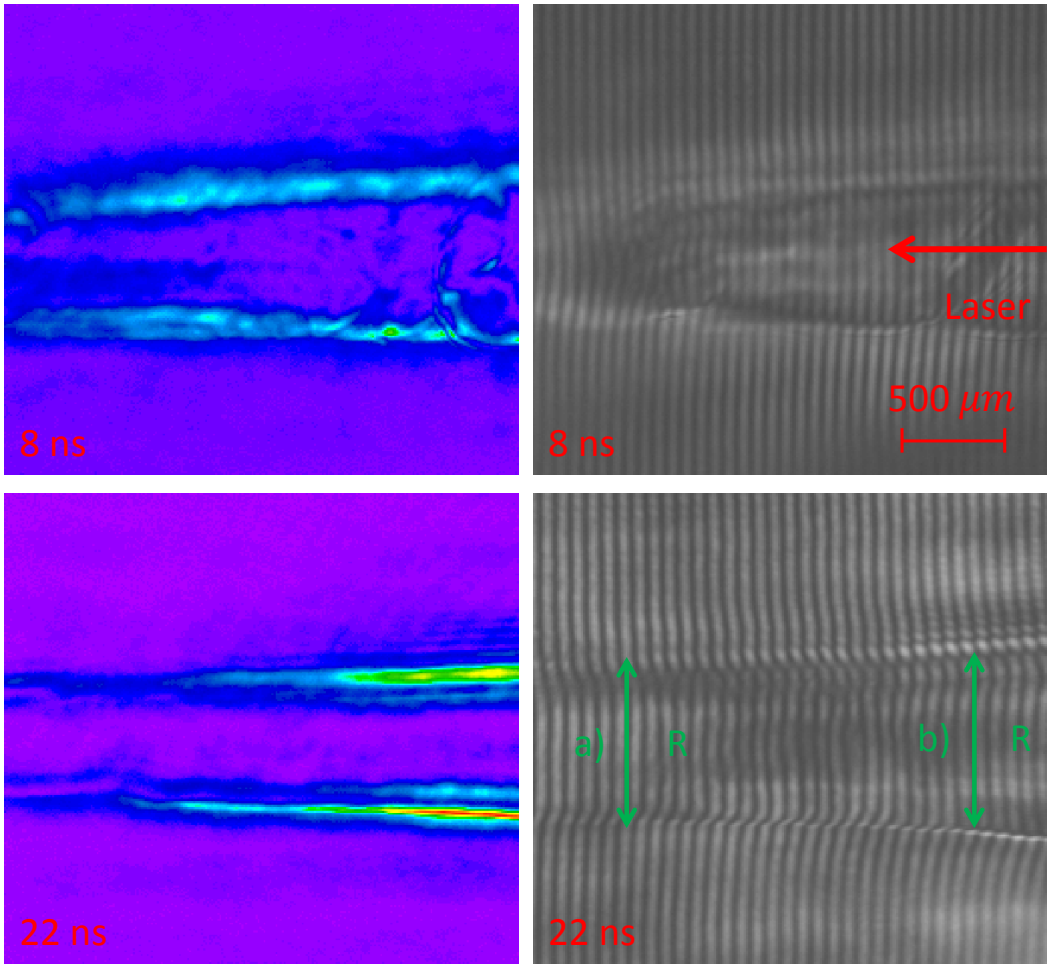

Figure 5.1: Schlieren and interferometric images of blast waves in krypton with backing pressure of 300 PSI and a 360 mJ laser pulse.

trajectory. After ∼10 ns, the blast wave settles to a value of $n = 0.42 \pm 0.03$, lower than the adiabatic case of $n = 1/2$.

For the blast waves in krypton with 360 and 600 mJ of energy, a sharp shock front has not yet fully developed until around ∼10 ns, approximately

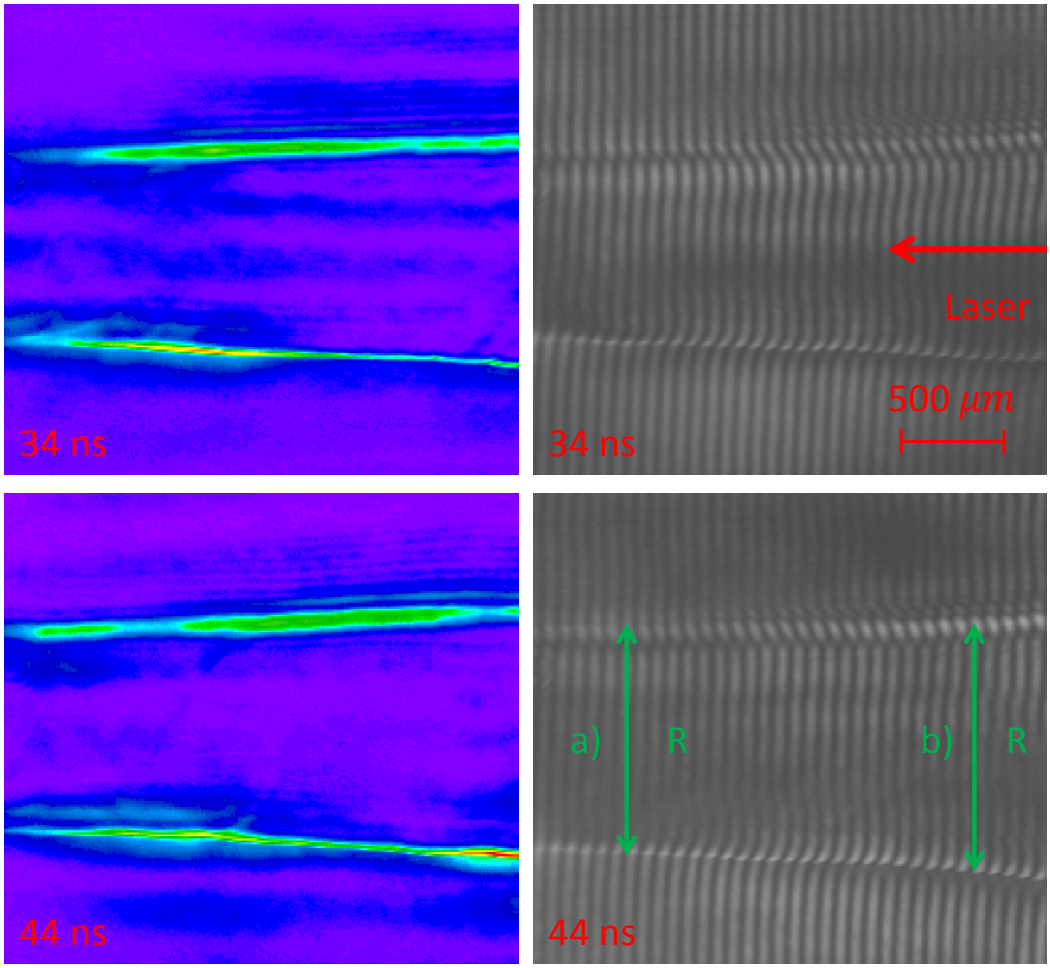

Figure 5.2: Schlieren and interferometric images of blast waves in krypton with a backing pressure of 300 PSI and a 360 mJ laser pulse.

the time at which we expect the blast wave to have swept up enough mass to enter the self-similar phase [11, 42]. We also see that with higher energy, the overall deceleration parameter is less than that of the 80 mJ case indicating that radiative losses are greater. With higher initial energy, a blast wave will

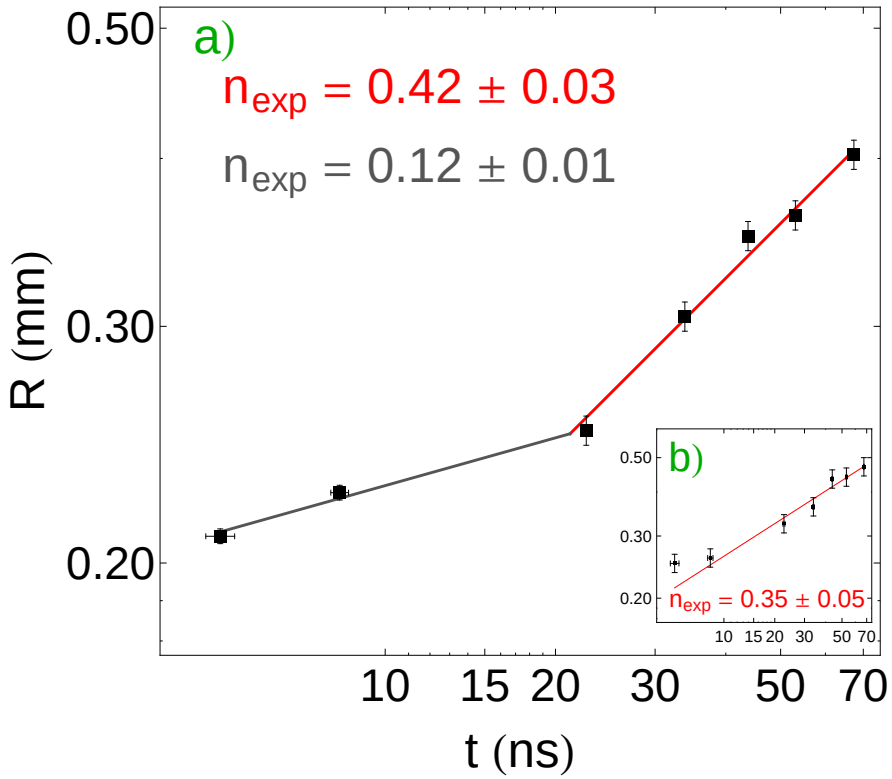

Figure 5.3: Plot of blast wave radius vs. time in krypton with 80mJ of laser energy. The red curve excludes the first two data points. The inset is the trajectory of the blast wave at the longitudinal location where the laser initially deposits its energy.

undergo more radiative losses because of the greater amount bremsstrahlung emission from hotter electrons and more bound-bound excitations in the atoms that eventually decay and emit light. Figs. (5.3)-(5.7) also show that at the longitudinal position indicated in Fig. (5.1) and (5.2), closer to the location of energy deposition, the deceleration parameter is generally lower, approaching

that of the radiative spherical case of $n \leq 2/5$.

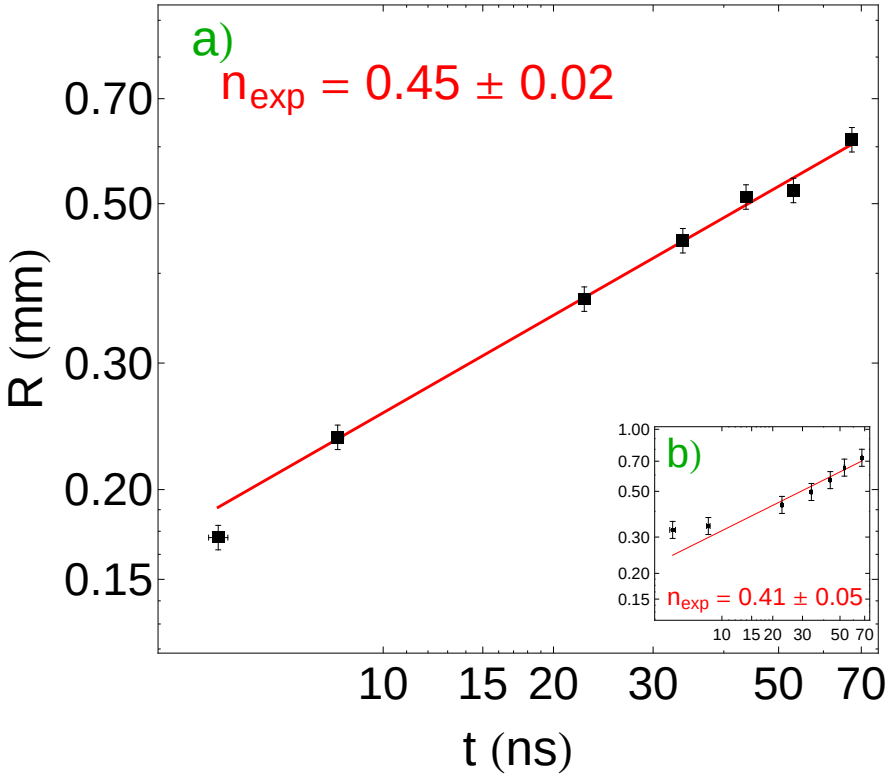

Figure 5.4: Plot of blast wave radius vs. time in krypton with 360mJ of laser energy.The solid red curve is the best fit to the data. The inset is the trajectory of the blast wave at the longitudinal location indicated by "b)" in Figs. (5.1).

We performed numerical simulations in HYADES, a one dimensional Lagrangian hydrodynamics code to investigate the effects of radiation on blast wave evolution. HYADES employs a tabular equation of state and treats radiation as a diffuse approximation with user defined photon groups. Figure (5.5) are simulation results for the density and pressure profiles of a blast wave

in hydrogen. As a low Z gas, the blast wave shows a sharp shock front due to the lack of radiative losses. We used an initial mass density of 2×10^{-4}

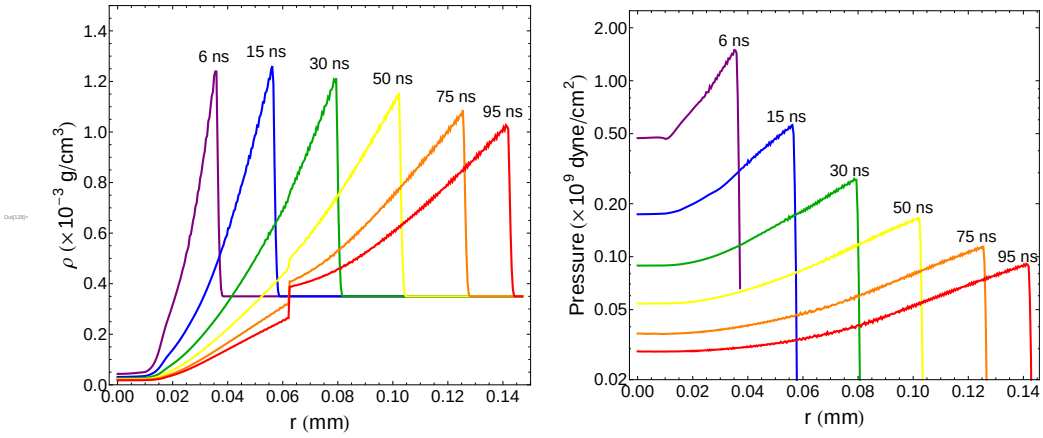

Figure 5.5: HYADES simulation for the density and pressure profiles of a blast wave in hydrogen.

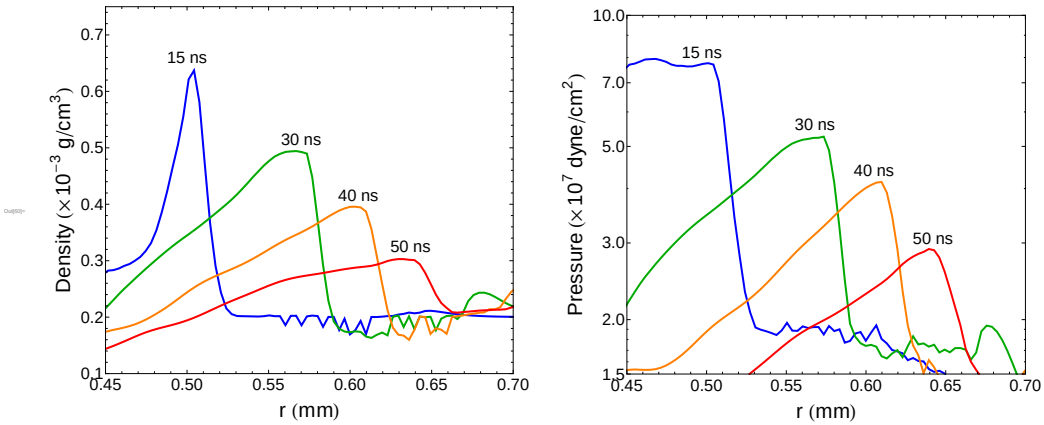

Figure 5.6: Density profiles at various times of a blast wave in krypton from HYADES simulations.

g/cm^3 and a 110 eV hot plasma filament at $t = 0$ to set off the blast wave in krypton. Figure (5.6) shows the density and pressure profiles from these simulations. The simulation results for the trajectory, $n = 0.450 \pm 0.008$, show good agreement with the experimental data for the blast wave in krypton with 600 mJ of laser energy when considering the entire time interval. However, if we divide the trajectory into segments and consider them separately, we arrive at different values for the power-law index: $n = 0.352 \pm 0.008$ from 10 to 25 ns and $n = 0.542 \pm 0.007$ from 25 to 70 ns. This is due to the blast wave in the simulation entering the radiative phase at earlier times and propagating with the lower deceleration parameter. As it expands and cools, the blast wave then enters the energy-recovery phase where it reabsorbs energy from the preheated ionized gas leading to a greater deceleration parameter than the Sedov-Taylor value of 1/2 [41].

Images of blast waves in argon are shown in Fig. (5.8). Since argon, has a lower Z value than krypton, we observe a deceleration parameter that is slightly greater than that of krypton of the same initial energy. In addition, these images suggest that argon blast waves enter the self-similar similar phase earlier than that of krypton as the fringe shifts are much sharper in the earliest image. We observed an experimental value of $n = 0.46 \pm 0.04$ for these blast waves. From HYADES simulations using an initial temperature of 140 eV, we observed a value of $n = 0.552 \pm 0.006$ for the entire time period which is greater than the Sedov-Taylor adiabatic value. If we divide the trajectory into segments as we did for krypton, the deceleration parameter takes the

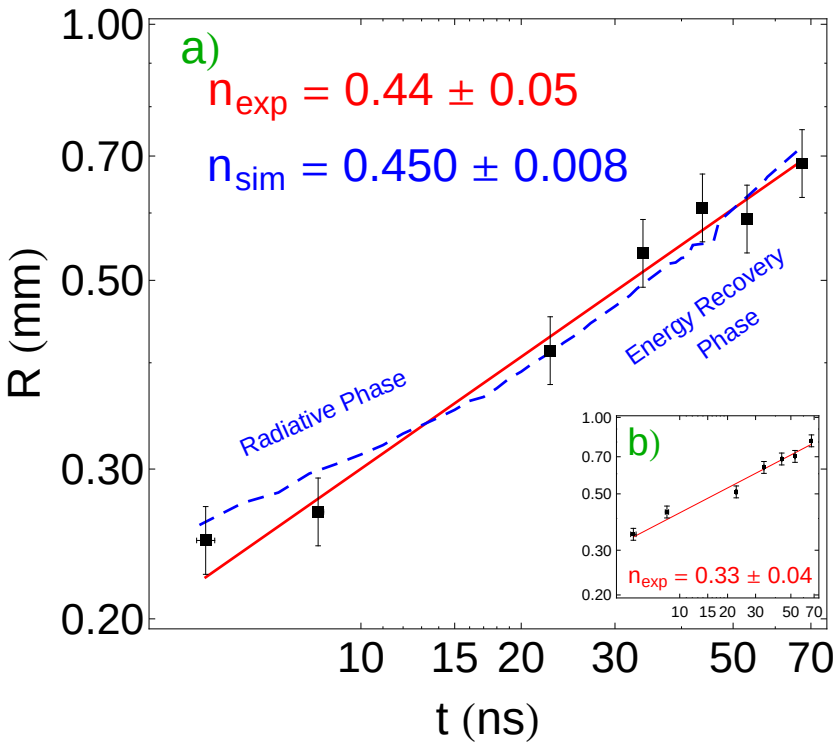

Figure 5.7: Plot of blast wave radius vs. time in krypton with 600mJ of laser energy. The solid red is the best fit for the data while the dashed blue is the trajectory from HYADES. The blast wave here enters the radiative phase at ∼10 ns.

value $n = 0.467 \pm 0.005$ from 10 to 20 ns and $n = 0.612 \pm 0.002$ from 20 to 45 ns. The HYADES simulations show that argon is less radiative than krypton during the radiative phase. It still recovers some energy from the preheated upstream medium and travels with a higher deceleration parameter than krypton during this phase. Figure (5.10) are the simulation results for the density and pressure profiles in argon at various times. We can calculate the

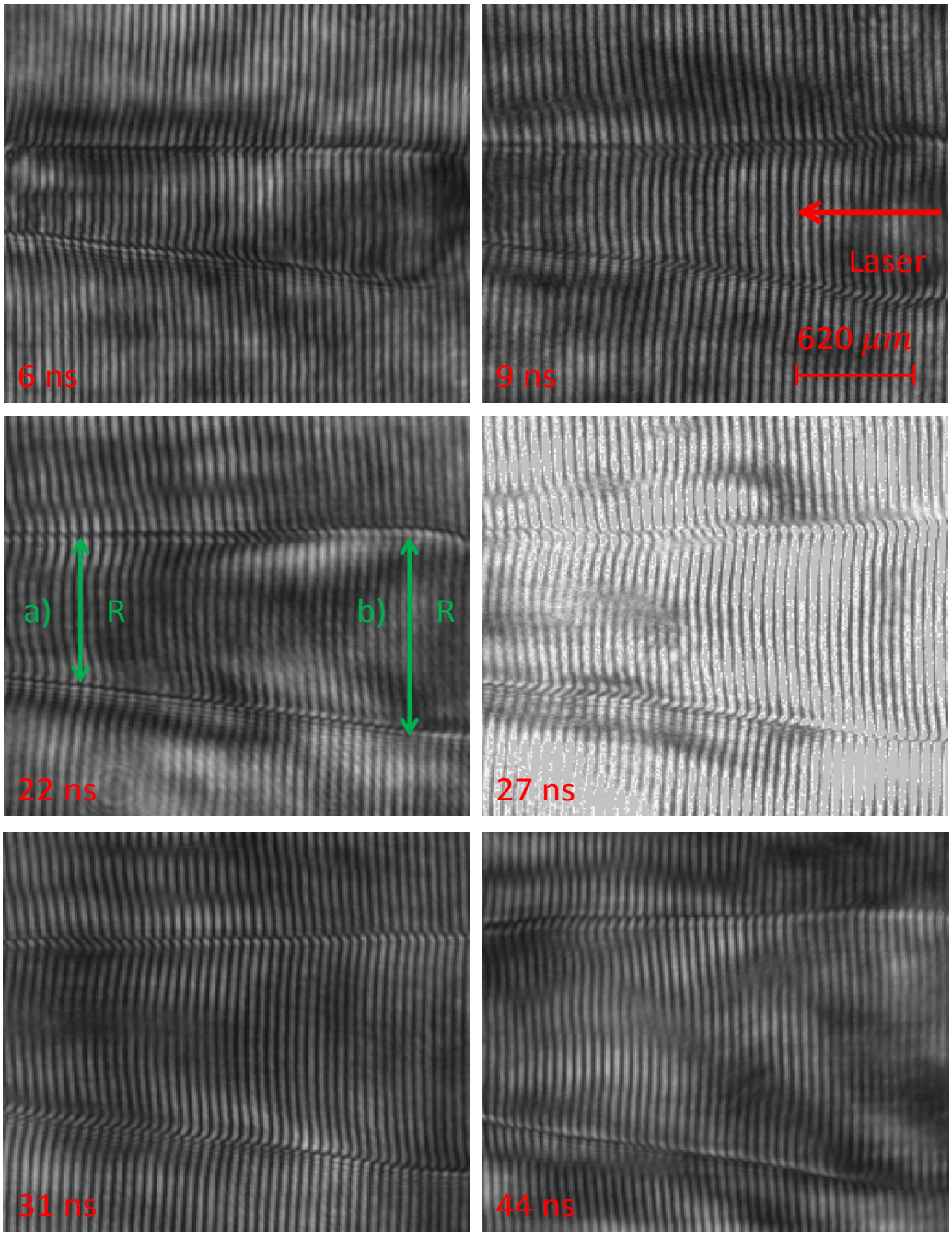

Figure 5.8: Interferometric images of blast waves in argon with a backing pressure of 800 PSI and a 600 mJ laser pulse. These blast waves exhibit more sphericity near the right edge than in those in krypton.

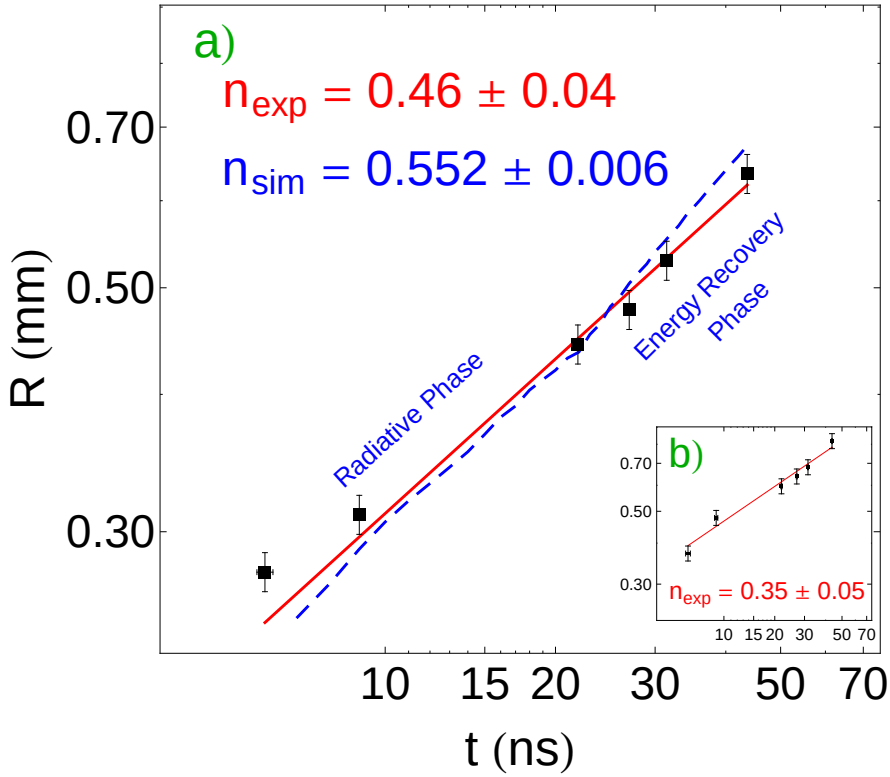

Figure 5.9: Plot of blast wave radius vs. time in argon with 600mJ of laser energy. The blue curve is the best fit for all data points. The red curve is the best fit for the last five data points, starting at around ∼10ns when we expect the motion to be self-similar. The inset is the trajectory of the blast wave indicated in Fig. (5.8).

effective adiabatic index γ_1 from these data using the semiradiative analysis, Eqn. (2.101). It should be noted that these calculations use for the adiabatic index of the internal cavity γ_c as 5/3. The physical quantities of interest are summarized in Table (5.1). These results indicate that blast waves in both krypton and argon are radiative, consistent with previous results, though the

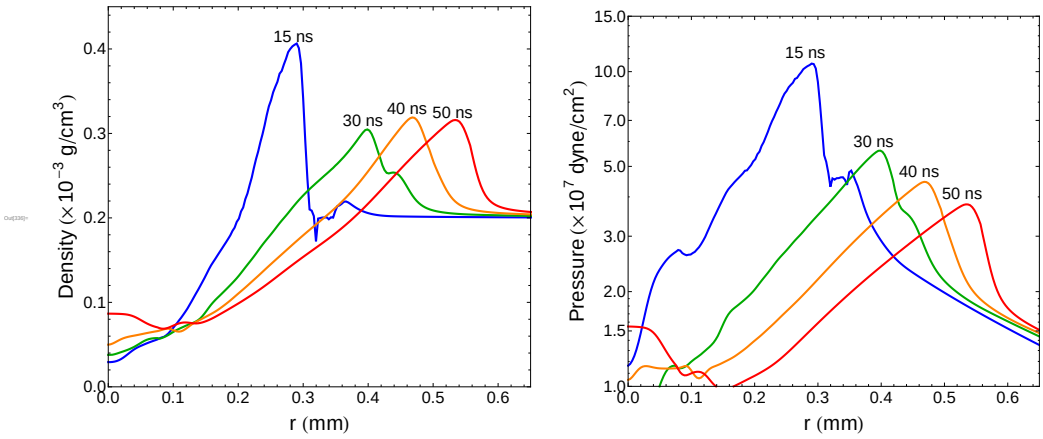

Figure 5.10: Density profiles at various times of a blast wave in argon from HYADES simulations.

effective adiabatic indexes reported in this thesis are higher [43].

Table 5.1: Deceleration Parameter n and Effective Adiabatic Index γ_1

Target Gas	n	γ_1
Argon	0.46 ± 0.04	1.40 ± 0.23
Krypton	0.44 ± 0.05	1.28 ± 0.28

5.2 Radiated Energy Loss Fraction

We can calculate the fraction of the blast wave's initial energy lost to radiation using the dimensionless cooling rate, ϵ, discussed in Ch. 2. Using Eqs. (2.86), (2.97), and (2.98), and the deceleration parameters measured from both experiment and HYADES simulations we calculated ϵ for the blast waves

in argon and krypton. Figs. (5.11) and (5.12) show the fraction of energy lost by radiation for argon and krypton blast waves, respectively.

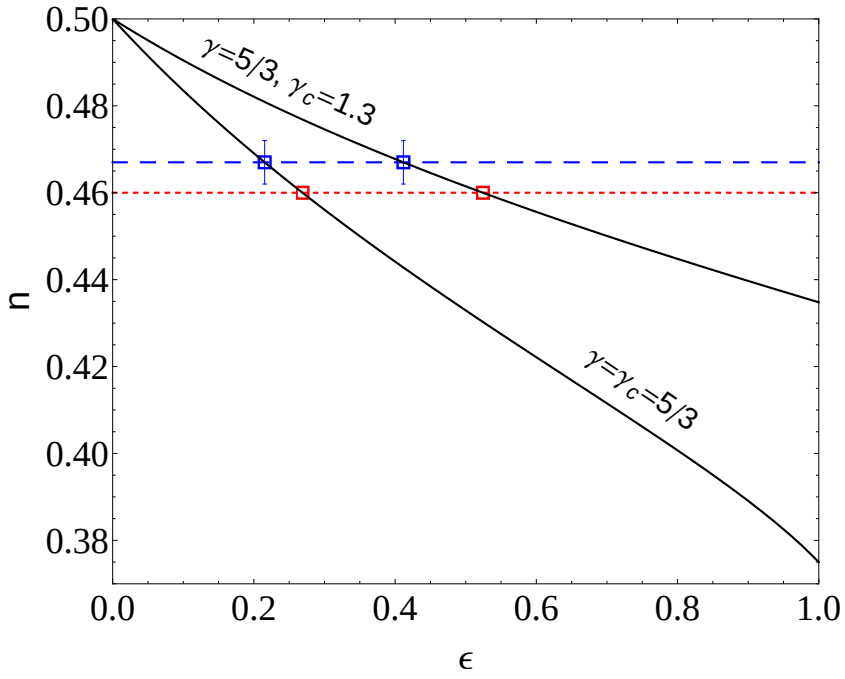

Figure 5.11: The energy loss fraction ϵ in argon for two values of the cavity polytropic index (see Section (2.4)). The horizontal lines are the deceleration parameters calculated from the trajectory in HYADES simulations (blue) and experimental data (red). The corresponding squares are intercepts of the n vs. ϵ curve and n from both.

In argon, the trajectory during the radiative phase from HYADES simulations were used to calculate ϵ since the deceleration parameter for the entire time interval was higher than the Sedov-Taylor case. In krypton, conversely, we used the trajectory during the entire time interval since the deceleration parameter during the radiative phase was in the fully radiative regime ($\epsilon \approx 1$).

The calculated radiated energy-loss fractions are summarized in Table (5.2).

Table 5.2: Energy-loss fraction ϵ from experiment and HYADES simulations.

Target Gas	γ_c	ϵ_{Exp}	ϵ_{Sim}
Argon	5/3	0.27	0.22
Krypton	5/3	0.44	0.35
Argon	1.3	0.52	0.41
Krypton	1.3	0.89	0.70

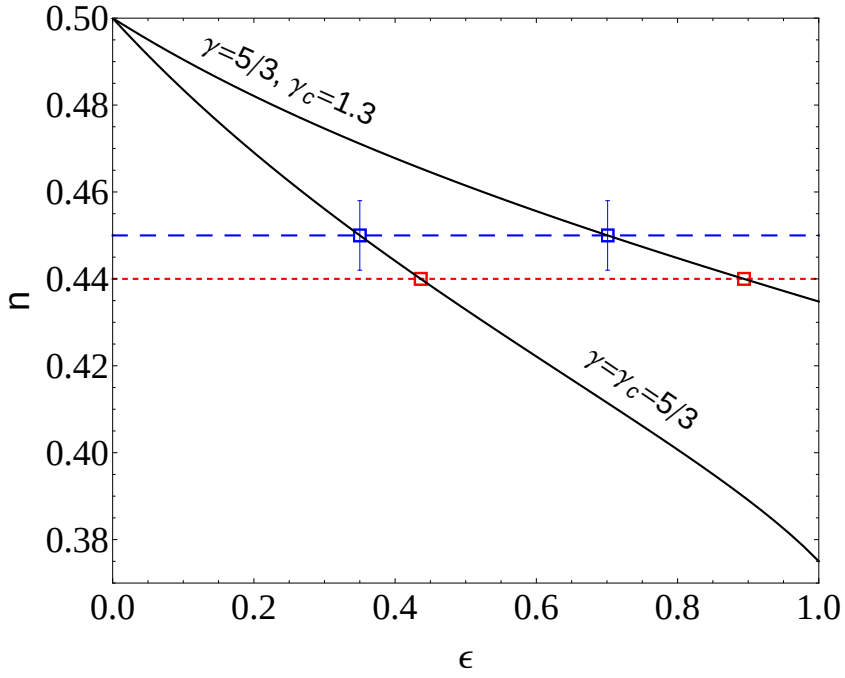

Figure 5.12: The energy loss fraction ϵ in krypton for two values of the cavity polytropic index (see Section (2.4)). The horizontal lines are the deceleration parameters calculated from the trajectory in HYADES simulations (blue) and experimental data (red). The corresponding squares are intercepts of the n vs. ϵ curve and n from both.

5.3 Ionization Precursor from Radiative Losses

A characteristic feature of a radiative blast wave is the gradual gradient in the electron density starting at the shock front and extending radially outwards. Conversely, a blast wave that is adiabatic or nearly adiabatic will exhibit a steep and abrupt electron density peak at the shock front. When radiative losses are present, the emitted radiation will preheat the upstream material and ionize the surrounding gas. This ionization front is observed in the Abel-inverted phase maps retrieved from interferometric images. Figs. (5.13) and (5.14) show the radial electron density profile of blast waves in krypton and argon, respectively.

Previous studies of blast waves in argon report the absence of an ionization front [40, 41] and attribute this to the less efficient radiation production because of argon's lower Z value. In contrast, the data from our experiments indicate that radiative losses indeed are present in argon. This is due to the higher energies with which we produced our blast waves. With higher deposited energies, the blast wave medium will undergo more radiation production since hotter electrons will radiate more bremsstrahlung emission and more atoms will be ionized or excited to higher energy levels resulting in greater line emission and radiative recombination emission.

It is in this preheated ionized upstream medium that a blast wave recovers some of the energy initially lost during its radiative phase. As the blast wave expands into this region, it reabsorbs energy which becomes added to the system resulting in an acceleration to the blast wave (it travels with a

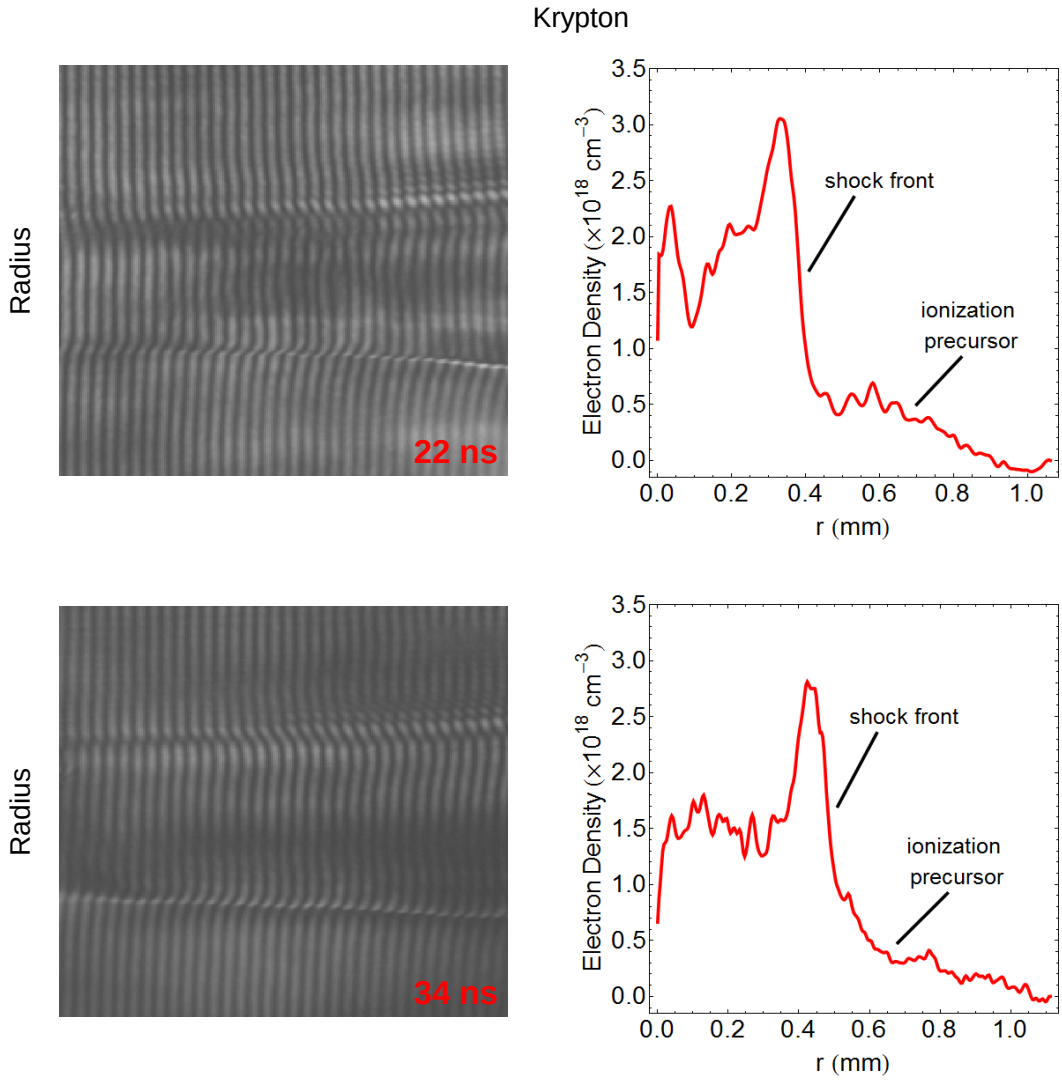

Figure 5.13: Radial electron density profile of krypton blast waves at 22 and 34 ns with 300 PSI of backing pressure and 360 mJ of laser energy. To the left are the raw interferometric images.

higher deceleration parameter). If enough energy is recovered, the blast wave can expand with a deceleration parameter that is greater than the Sedov-

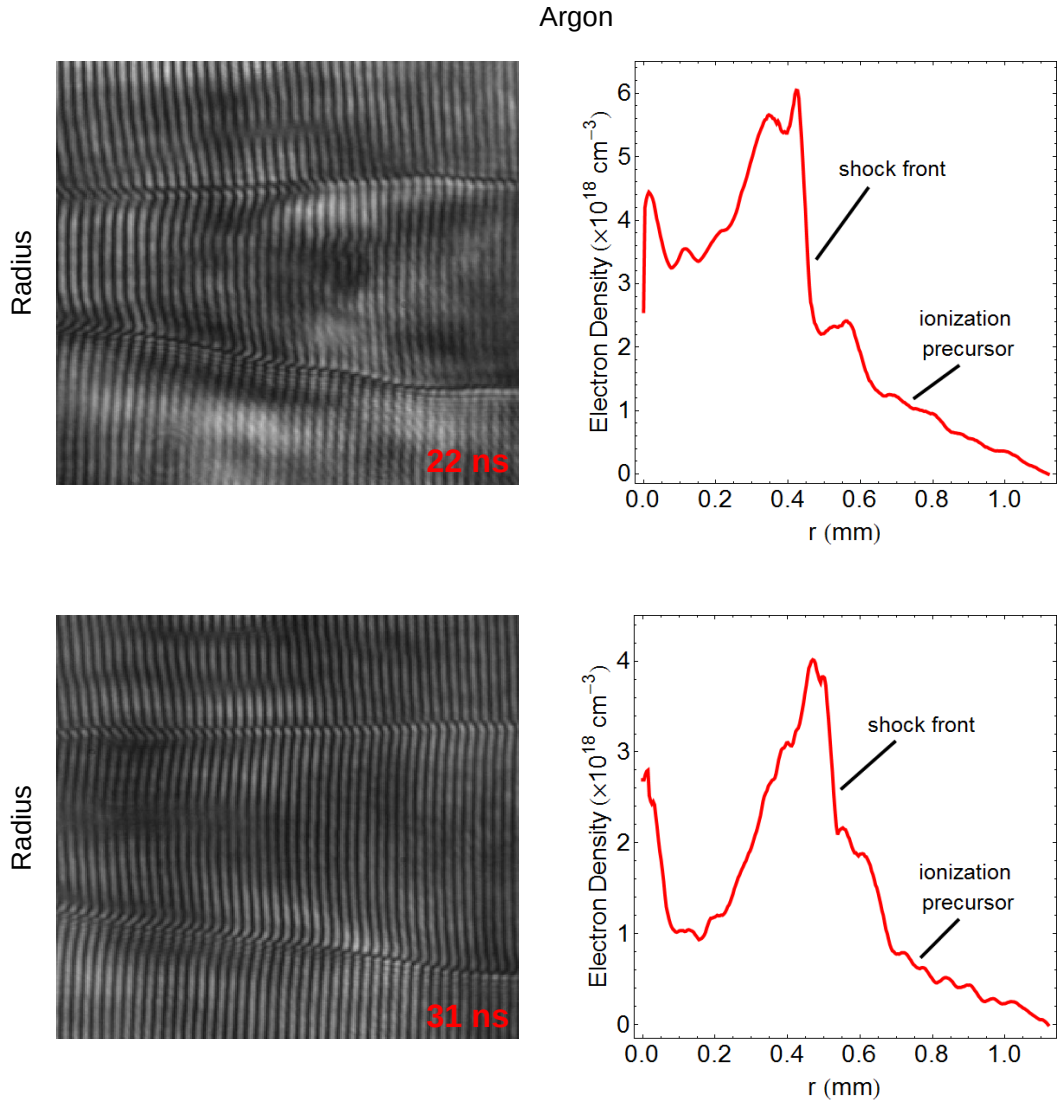

Figure 5.14: Radial electron density profile of argon blast waves at 22 and 31 ns with 800 PSI of backing pressure and 600 mJ of laser energy. To the left are the raw interferometric images.

Taylor value of 1/2. This effect is observed in the HYADES simulations we performed. As seen in Figs. (5.7) and (5.9), the simulations showed that

the blast wave trajectory in argon and krypton experience an increase in the deceleration parameter at later times.

5.4 Double Shock Front Formation from a Strongly Radiative Blast Wave

The presence of an ionization precursor and a lower deceleration parameter are indications that a blast wave is experiencing radiative losses. We have found in a series of experiments that if a strongly radiative blast wave is traveling in an optically thick medium, the emitted radiation is reabsorbed by the upstream medium and a secondary shock in the ionization precursor is produced.

It was first reported by Hansen et al. [44] that under certain conditions, a high Mach number, strongly radiating laser-driven blast waves in xenon gas exhibited structure characteristic of a second shock forming out in front of the primary blast front. They attributed this phenomenon to the reabsorption of radiation by the optically thick upstream medium creating a radiative heat wave (RHW) that travels supersonically ahead of the main shock [44]. As the blast wave propagates into the heated medium it slows and loses energy, diminishing in speed. When the radiative heat wave slows down to the transonic regime, a secondary shock in the ionization precursor is produced.

In this experiment, the authors focused a 10 to 200 J, 1064 nm laser pulse with a pulsewidth of 5 ns onto a solid steel pin target immersed in either nitrogen or xenon gas at a pressure of $\sim$1 kPa. A spherical blast wave

was created by the rapid ablation of the pin by the laser. They employed a standard Schlieren technique to image the blast wave. In xenon gas as the ambient medium, the blast wave is observed until $t \approx 8\,\mu s$ at which point a second shock forms ahead of the initial main shock. Images of blast waves in xenon with observation of a secondary shock structure is seen in Fig. (5.15). To understand their experimental results, these authors ran 1D numerical

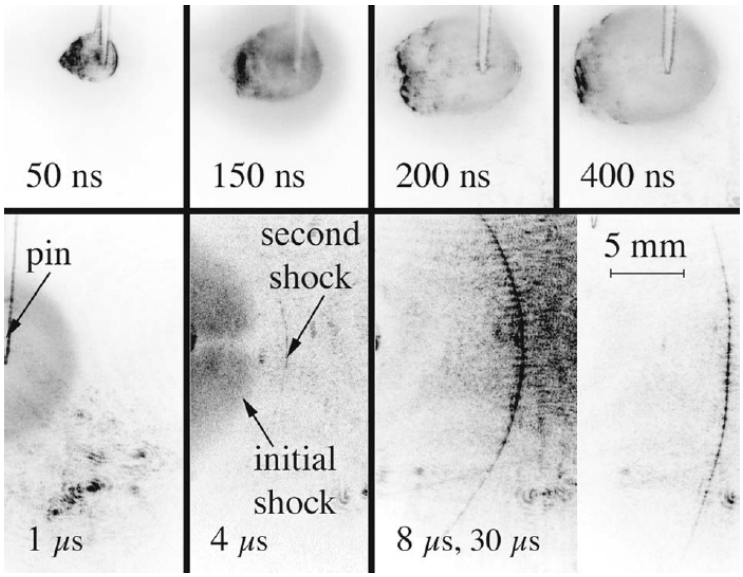

Figure 5.15: Schlieren images of blast wave expansion in xenon gas (1.3 kPa) at $t = 50\,ns$ to $30\,\mu s$ produced by laser ablation of solid pin ($E_l = 10\,\mathrm{J}$). At $t \approx 4\,\mu s$, a second shock appears ahead of the main shock front. Taken from Ref. [44].

simulations using the LASNEX code [44] in which a multiphoton diffusion approximation was used to treat radiative losses and a large enough optical depth in the RHW. Fig. (5.16) shows the results of these simulations in xenon.

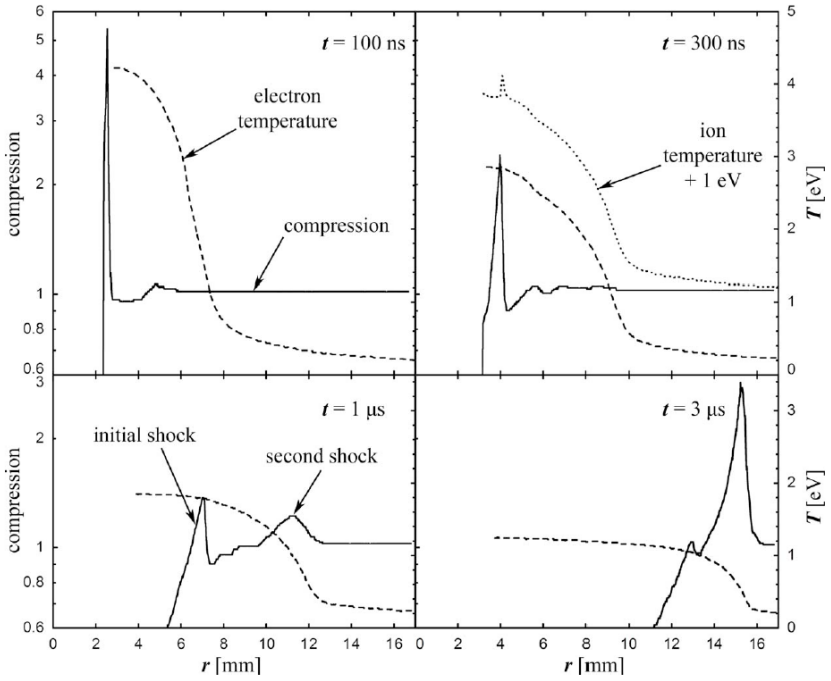

Figure 5.16: 1D numerical simulation results in the electron/ion temperature and compression using the LASNEX code, taken from Ref. [44]. At $t = 1\,\mu s$, the simulations show the birth of a second shock.

In our experiments using krypton as the cluster target source, we produced cylindrical blast waves with a high-intensity $\sim 10^{17}$ W/cm^2, 1057 nm, $\sim$115 fs laser pulse and observed the presence of a secondary shock structure from interferometric images. These appear as a shift in the fringes ahead of the main shock front in Fig. (5.17), especially apparent in the image at 9 ns. A sharp fringe shift like this is indicative of a steep electron density gradient as found when a shock discontinuity occurs.

To elucidate the physics behind radiative shocks, we performed numer-

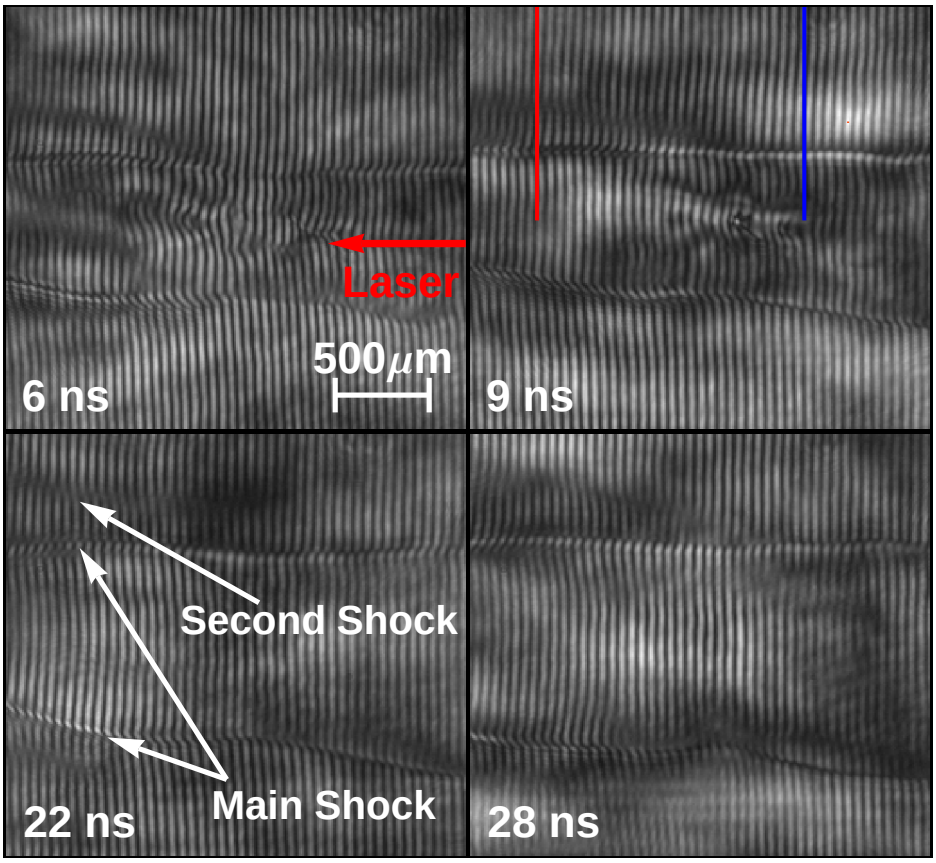

Figure 5.17: Inteferograms of blast waves in krypton at 300 PSI backing pressure. Note the additional fringe shift in the upper left portion ahead of the main shock front.

ical simulations using the 1D hydrodynamic code HYADES. These calculations were performed using a multigroup photon treatment for radiative losses and adjusting the optical depth to large enough values such that reabsorption would occur within the spatial scales of the experiment. Under the right conditions, we observed evidence of a secondary shock forming ahead of the main

shock. Exclusion or weakening of radiative processes from the numerical simulations prevented this phenomenon from occurring, and it was further found that the thermal conductivity of electrons was negligible in the overall dynamics. Furthermore, our simulations have shown that the local mass density of the region of interest plays a significant role in the radiative hydrodynamics of the process, with lower values being more conducive to a secondary shock formation. In our simulations we have found that a mass density of .00003 g/cm^3 corresponded well to our observed experimental data. Fig (5.18) and (5.19) show the measured and calculated radial electron density profiles of these blast waves that show the secondary shock structure along with the simulation results for the compression and electron temperature. Below the electron density profiles are the numerical results of the compression and electron temperature. Note that the second shock is borne at the location where the radiative heat wave is present as indicated by the electron temperature profile. At the initial shock, this temperature profile takes on a more adiabatic jump as expected.

The blast wave and secondary shock front trajectory was measured in the same manner as discussed in Section (5.1). A decleration parameter of $s = 0.42 \pm 0.04$ and $s = 0.34 \pm 0.02$, respectively, was calculated from these measurements. The departure of the blast wave's deceleration parameter from that of the Sedov-Taylor case suggests that radiative losses are playing a significant role while the secondary shock front is itself too slow to be radiative [45]. Fig. (5.20) shows the trajectory of both shock fronts.

The absence of a secondary shock at longitudinal positions to the right

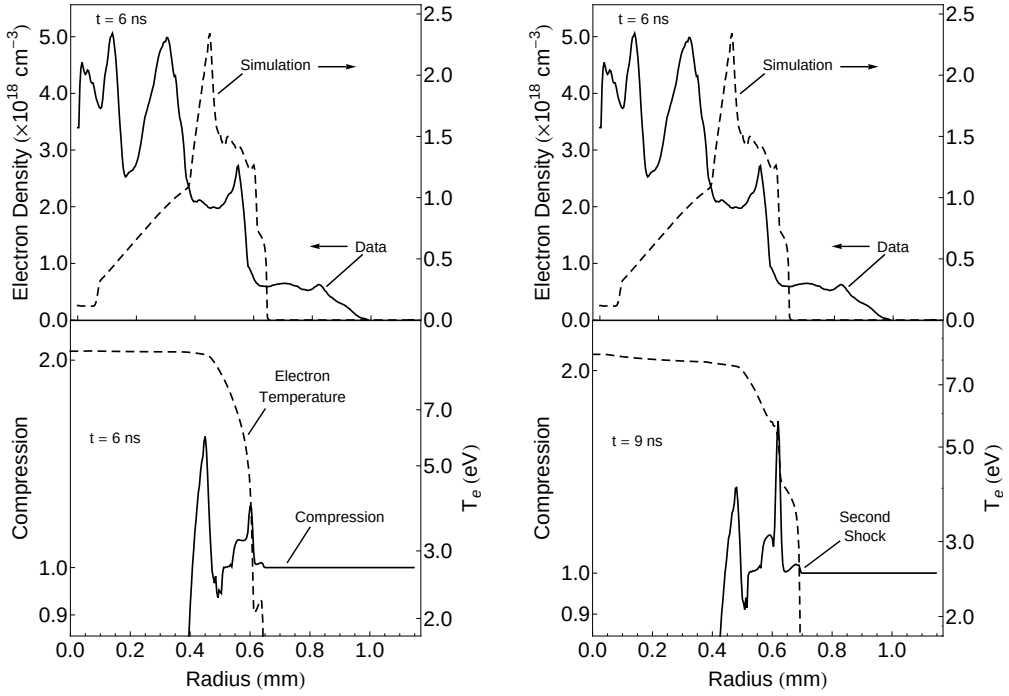

Figure 5.18: Radial electron density measurements (top) of the blast waves seen in Fig. (5.17) from the upper left corner where the secondary shock is seen (solid). Shown together are the electron density calculations from HYADES (dashed). The compression and electron temperature calculations from HYADES are on bottom.

may be due to the higher local mass density of the gaseous medium which is in closer proximity to the gas jet (upper right in Fig. (5.17), off screen). At these locations, radiative losses manifest themselves as an ionization precursor. Fig. (5.21) shows the radial electron density profiles of the blast waves at 9 ns and 22 ns.

If the medium is optically thin, a radiative heat wave would not form

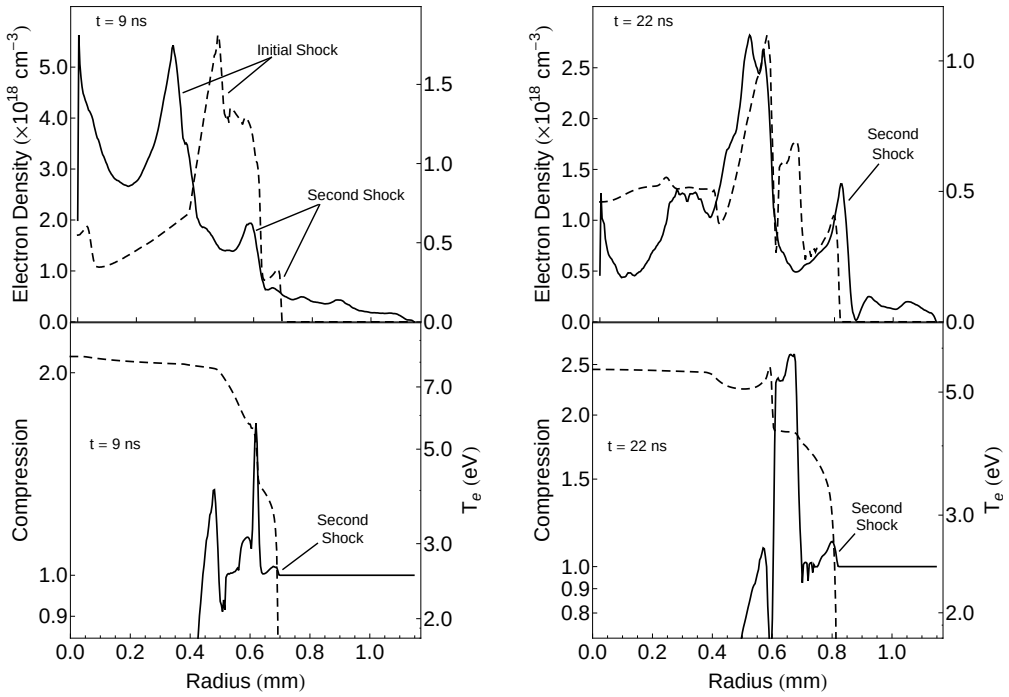

Figure 5.19: Radial electron density measurements (top) of the blast waves seen in Fig. (5.17) from the upper left corner where the secondary shock is seen (solid). Shown together are the electron density calculations from HYADES (dashed). The compression and electron temperature calculations from HYADES are on bottom.

and the energy lost by radiation from the blast wave would be carried out to "infinity" [44]. In order that we observe the effects of a RHW means that the radiation mean free path is relatively short, at least within the length scales of our imaging diagnostics. The sequence of events for when a secondary shock forms is as follows: a strongly radiative blast wave (which we refer to as S1) loses energy via radiation in an optically thick medium. The radiation mean

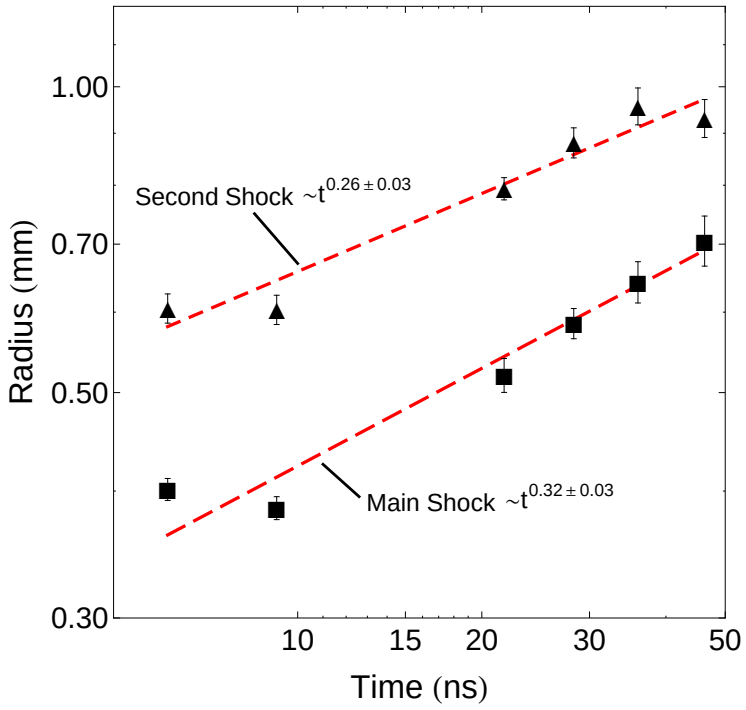

Figure 5.20: Initial and secondary shock front trajectories of the blast waves in Fig. (5.17) at the upper left corner where the second shock is present.

free path is relatively short resulting in a supersonic radiative heat wave that travels ahead of S1. As S1 slows down, it radiates less and the RHW slows down because of its expansion and diminishing radiative losses from S1 which act as a driving source. When the supersonic RHW slows down to 2 times the sound speed of the region immediately behind it, a shock will form in order that momentum be conserved. Fig. (5.22) shows schematically a cross sectional view of a cylindrical blast wave with the sequence of events.

We can calculate the location of where a second shock forms by us-

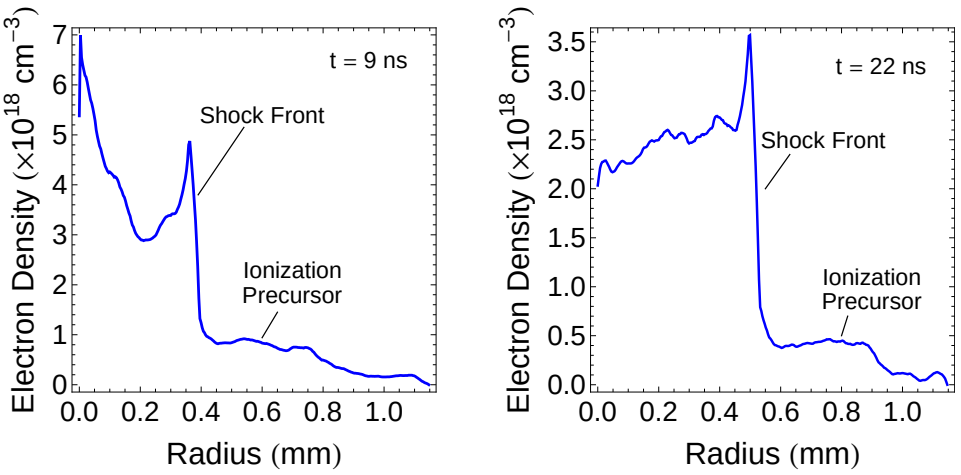

Figure 5.21: Electron density measurements at 9 ns and 22 ns of the blast waves in krypton. These measurements are taken from the blast waves of Fig. (5.17) in the upper right portion of the image, closer in proximity to the gas jet nozzle.

ing Barenblatts [46] self-similar solution for an instantaneous point release of energy (for the cylindrical case it would be a line release of energy) with heat conduction included [47]. Consider the 1D fluid equations for mass and momentum conservation

$$\rho_1 u_1 = \rho_2 u_2 \tag{5.2}$$

and

$$P_1 + \rho_1 u_1^2 = P_2 + \rho_2 u_2^2 \tag{5.3}$$

in the rest frame of the radiative heat wave (RHW), where ρ, P, and u are the density, and gas velocity, respectively. Here, quantities with subscript 1 denote the region ahead of the RHW while quantities with subscript 2 denote

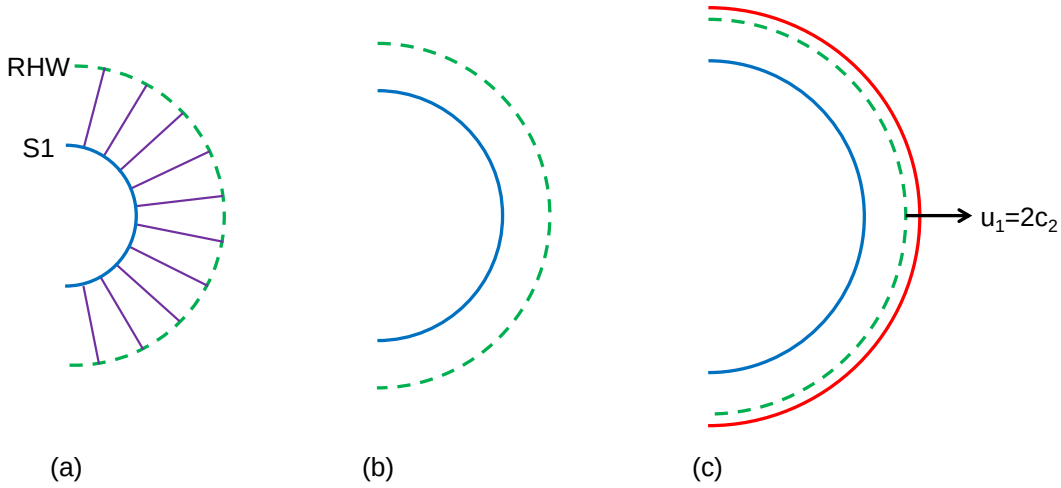

Figure 5.22: Sequence of events for formation of secondary shock front (time increases from left to right): (a) A cylindrical blast wave, S1, is strongly radiative and drives a radiatve heat wave ahead of itself. (b) S1 radiates less as it expands and slows down. The RHW is also expanding and slows down as the driving source for it, i.e., the radiation from S1, diminishes. (c) When the velocity of the RHW slows down to $u_1 = 2c_2$, where c_2 is the sound speed in the region immediately behind, a shock forms to conserve momentum.

the region behind. By combining these two conservation equations, we can solve for the compression

$$\eta \equiv \frac{\rho_2}{\rho_1} = \frac{c_1^2 + u_1^2 \pm \sqrt{(c_1^2 + u_1^2)^2 - 4c_2^2 u_1^2}}{2c_2^2} \tag{5.4}$$

(Here we assume an ideal gas, $P = \rho c^2$, where c is the speed of sound). A real-valued compression, η, requires $u_1 \geq c_2 + \sqrt{c_2^2 - c_1^2} \approx 2c_2$, where we use the approximation $c_1 \ll c_2$ (this is a valid approximation because the temperature behind the RHW is much higher than the temperature in front it [47]). This leads to the requirement that the mixed Mach number, $M \equiv u_1/c_2 \geq 2$. Once the Mach number drops below 2, the RHW can no longer satisfy Eq. (5.4)

and a shock forms at the location of the RHW to conserve momentum. To approximate the position of the RHW when this mixed Mach number drops below 2, we first assume a power-law dependence of the radiative conductivity (in SI units of J m^{-1} K^{-1} s^{-1})

$$\chi = \chi_0 \rho^a T^b \tag{5.5}$$

in the upstream medium. In a fully ionized plasma, $a = -2$ and $b = 13/2$ [47]. The RHW radius r_h is given by Barenblatt's self-similar solution

$$r_h(t) = r_0 t^\delta, \tag{5.6}$$

where

$$r_0 = \left[\left(\frac{2(\gamma-1)}{S_n B(n/2, 1+1/b)} \frac{E_0}{\rho_0} \right)^b \left(\frac{2\chi_0(\gamma-1)}{\Gamma^{b+1}\rho^{1-a}} \frac{nb+2}{b} \right) \right]^\delta \tag{5.7}$$

and

$$\delta = 1/(nb+2). \tag{5.8}$$

Here, $B(x, y)$ is the Beta function, $n = 1, 2, 3$ and $S_n = 1, 2\pi, 4\pi$ for planar, cylindrical, and spherical geometry, respectively. Γ is the gas constant and is given by the ideal gas law $(\gamma - 1)e = \Gamma T$. To solve for χ_0 we use the relation

$$\chi = \frac{16\sigma T^3 l_R}{3}, \tag{5.9}$$

where

$$l_R = \frac{4.4 \times 10^{20}\, T^{\circ 7/2}}{N_e^2 \overline{m}(\overline{m}+1)^2}\ (\mathrm{m}) \tag{5.10}$$

is the Rosseland mean free path for a multiply ionized gas of hydrogen-like atoms with an appropriate charge and is derived using Saha equilibrium for

ion densities [5]. In Eq. (5.9), N_e is the electron density, $\overline{m}$ the average ionization, and σ the Stefan-Boltzmann constant. The average ionization in a ∼2.5 eV krypton plasma is ∼4.5 [48]. Using our measured value for the electron density of $\sim 3 \times 10^{18}$, we estimate for the Rosseland mean free path $l_R \approx 1.5\,\text{mm}$. From this, we can solve for the time at which the RHW velocity $u_1 = \frac{dr_h}{dt}$ becomes Mach 2. In our experiment, this occurs at $t \approx 7\,\text{ns}$ with $r_h \approx .8\,\text{mm}$. The interferometric images in our data show what appears to be a steepening of the ionization precursor and the beginnings of a shock structure at 6 ns out at a radius of $\sim .5\,\text{mm}$ while the simulations show this occurring at a radius of $\sim .6\,\text{mm}$ for the same time. A more prominent shock discontinuity is seen at 22 ns with a second shock radius of $\sim .8\,\text{mm}$.

5.5 Evolution of Blast Wave Instabilities

The time evolution of instabilities on a blast wave surface is an area of interest in these types of laboratory astrophysics experiments because of its application in understanding certain astrophysical phenomenon. Previous experiments [25, 28] sought to make experimental observations of the Vishniac overstability and measure the growth rate of these instabilities. In the experiments by Grun et al., they created spherical blast waves by irradiating a 6 μm polystyrene foil in a chamber filled to 5 Torr of pressure in either nitrogen or xenon [25]. This work reported the growth of instabilities from noise when blast waves were launched in xenon gas but not in nitrogen. Images of blast waves from this work can be seen in Fig. (5.23).

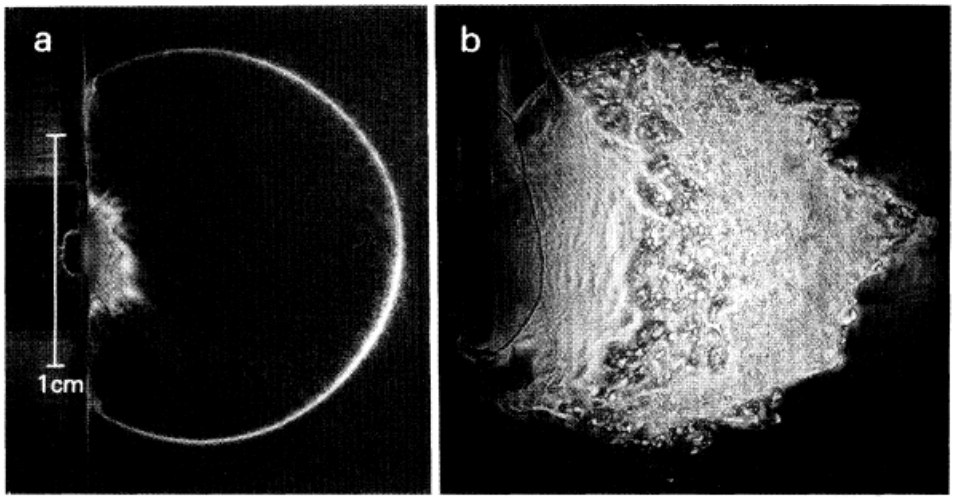

Figure 5.23: Schlieren images of a stable blast wave in (a) nitrogen, and an unstable one in (b) xenon. These blast waves were produced with a 200 J, 1054 nm, 5 ns laser pulse. Figure taken from [25].

The work by Grun et al. reported a growth rate of $t^{1.6}$ for a spherical mode number of $l \sim 10$ with $\gamma = 1.06$, the value they measured for xenon, whereas the theory set forth by Ryu and Vishniac [23] predicts a growth rate of $t^{0.7}$ for the same parameters. This discrepancy was later resolved by Edens et al. in which they observed similar turbulent structures in xenon and nitrogen blast waves but attributed this to preionization of the gas in the region traversed by the drive laser [27]. The velocity and temperature of a laser driven blast waves increases with the laser energy and therefore the significance of radiative losses on the hydrodynamics of the blast wave. Edens et al. reported the presence of these unstable features in both nitrogen and xenon primarily in the region traversed by the laser. These features became more prominent

as the drive laser energy was increased.

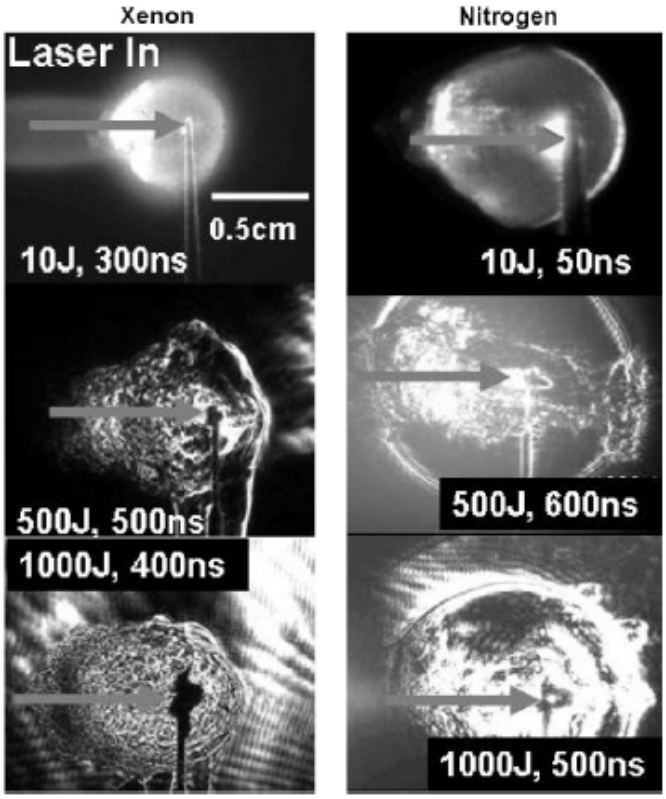

Figure 5.24: Schlieren images of blast wave in nitrogen and xenon showing turbulent features in both in the region traversed by the laser. These features become more prominent as laser energy is increased. Taken from Ref. [27].

Further work by Edens et al. [28] explored the validity of the Vishiniac overstability mechanism in hydrodynamic instabilities by directly inducing perturbations on the blast wave surface by means of a regularly spaced wire array. This method sidestepped the difficulty of measuring small amplitude perturbations that grew out of noise [26] such as the work of Laming and

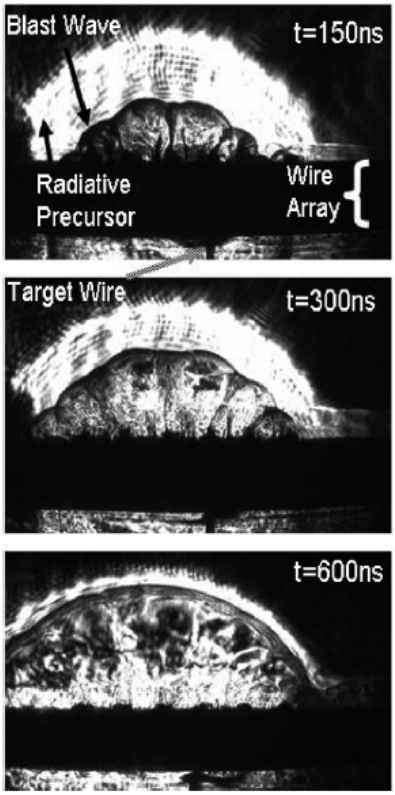

Figure 5.25: Schlieren images of blast wave in nitrogen at various times showing ripples induced by a wire array with a 4 mm spacing corresponding to a mode number of $l = 28$. Figure taken from Ref. [28].

Grun [25]. The growth rate of perturbations by the Vishniac overstability mechanism is primarily dependent on its spatial frequency (or mode number l) and the polytropic index γ of the gas. These experiments used a plastic pin target in a chamber filled with various gases and produced spherical blast waves. A wire array was placed in the path of the expanding blast wave to induce perturbations on the surface. The mode number l was controlled by the spacing of the wires and its radial distance from the origin and polytropic

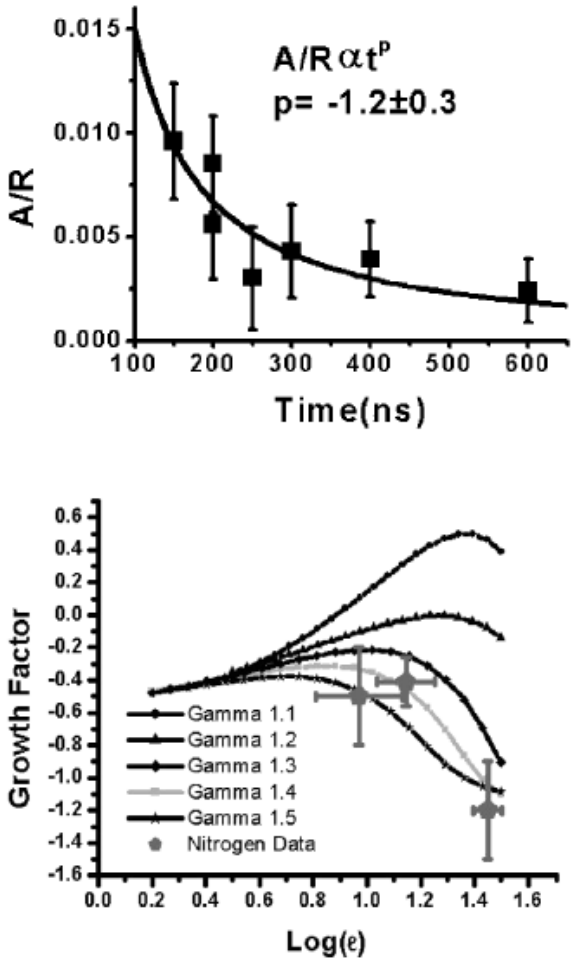

Figure 5.26: Plot of the normalized amplitude of the perturbation with mode number $l = 28$ as a function of time (Top). The data points are fitted to a power law in time. Plot of the decay rate of perturbed blast waves in nitrogen for several values of l (Bottom). Shown are experimental data points superimposed with theoretical curves of Ryu and Vishniac for several values of γ [23]. Figures taken from Ref. [28].

index γ by using various gases. Schlieren images of rippled blast waves were traced out and Fourier-transformed to extract the mode number of interest set

by the particular wire array. Shown in Fig. (5.25) are sample images of these blast waves. By tracking the amplitude normalized to the blast wave radius with respect to time, these authors were able to compare their results with the predictions of Vishniac [28]. The normalized amplitude of the primary l was fitted to a power law in time and tabulated for several values of l to compare to predictions. Fig. (5.26) are the results of Edens et al..

We have performed experiments with cylindrical blast waves to explore further the Vishinac overstability in hydrodynamic instabilities. These blast waves were produced by irradiating a gas of atomic clusters. Unlike the experiments of Edens et al., we addressed the in-feasibility of using a wire array because of the smaller length scales typically involved in these cluster experiments by means of optically "machining" the cluster medium to induce perturbations [49, 50]. Blast waves were produced using a cluster gas jet assembly backed by either nitrogen, argon, or krypton.

In these experiments, we varied the modulation frequency, or the wavenumber k, of the induced perturbation by adjusting the fringe spacing from the machining beam interferometer. For argon and krypton blast waves, we modulated the blast waves with a wavenumber of $k = 14,\ 17,$ and $22\ \text{mm}^{-1}$ corresponding to a modulation wavelength of $\lambda = 0.43,\ 0.36,$ and 0.28 mm, respectively. Shown in Figures (5.27) - (5.29) are images of blast waves in argon, krypton, and nitrogen that have been imparted with a modulation wavelength of $\lambda = 0.43$ mm.

The images of argon with this particular wavenumber show prominent

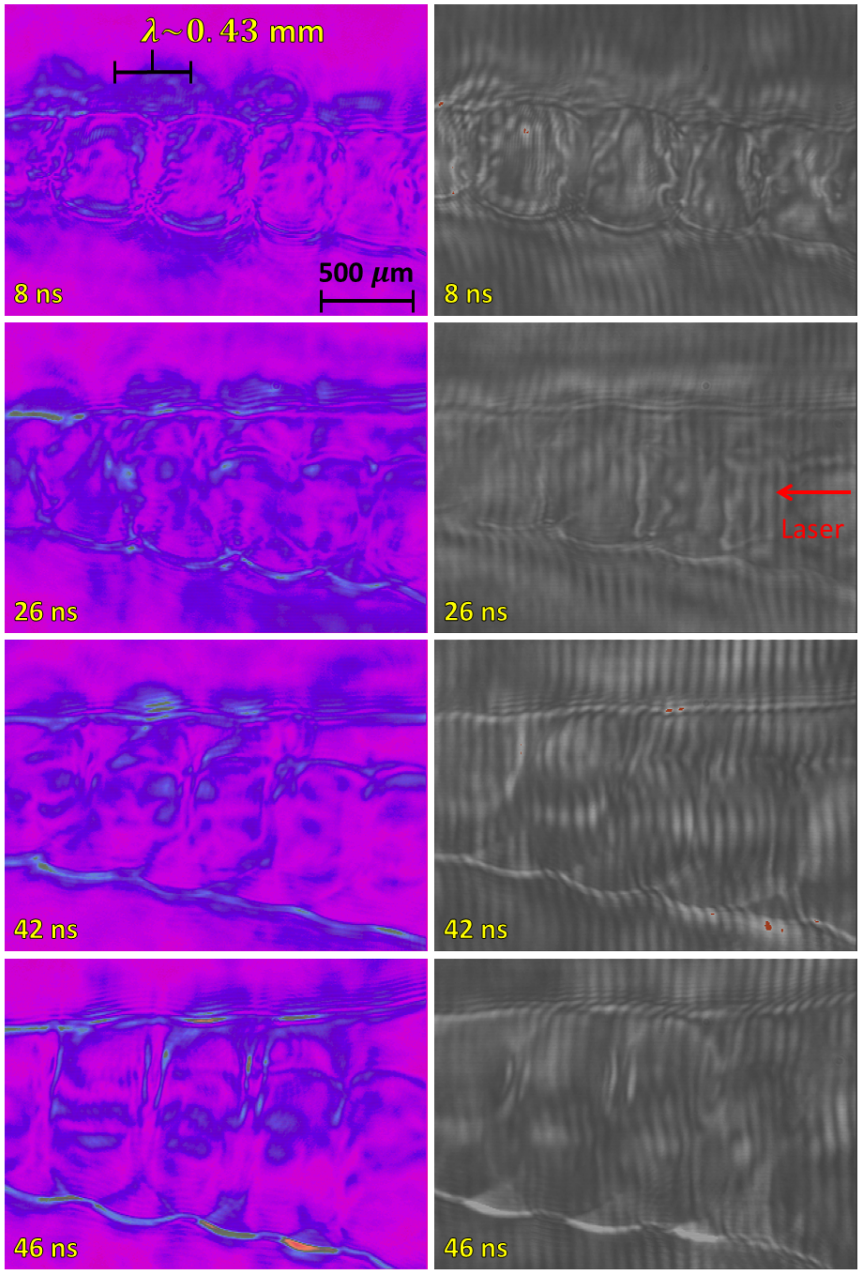

Figure 5.27: Schlieren and interferometric images of modulated blast waves in argon produced with a backing pressure of 800 PSI and a 600 mJ laser pulse. The wavenumber of the modulation is $k = 14\,\mathrm{mm}^{-1}$.

modulations and even appears to be larger in amplitude at 46 ns than at 42 ns. However, it must be noted that it is the amplitude normalized to the blast wave radius at that particular time that must be considered in our analysis.

Nitrogen, with its lower Z number provides a useful comparison as it is less radiative than both argon and krypton. Fig. (5.29) show the images of modulated blast waves in nitrogen. At earlier times, these modulations are clearly visible but seem to decay more readily than the other gases with the same wavenumber. This is especially apparent on the upper portion of the blast wave surface where the modulations seem to have damped out completely.

In general, for a given polytropic index, shorter wavelength modulations decay faster than for longer ones. To compare the behavior of perturbations with higher wavenumbers, we produced blast waves in all three gases under the same conditions with the higher wavenumber $k = 22$ mm^{-1}. Figures (5.30) to (5.32) show images of modulated blast waves with wavenumber $k = 22$ mm^{-1}. These shorter wavelenghth perturbations to indeed appear to damp out faster than those of Figs (5.27) to (5.29), especially for that of krypton.

To analyze the evolution of these blast waves with an imparted perturbation we traced out by hand the blast wave surface and Fourier transformed it to obtain a frequency spectrum. A sample plot of such a trace is shown in Fig. (5.33). We applied a 80% cosine taper window to smooth out the discontinuities at the ends to these traces [25] and Fourier transformed to obtain the primary modulation wavenumber. This was performed for the images acquired for the various time delays and normalized to the blast wave radius at

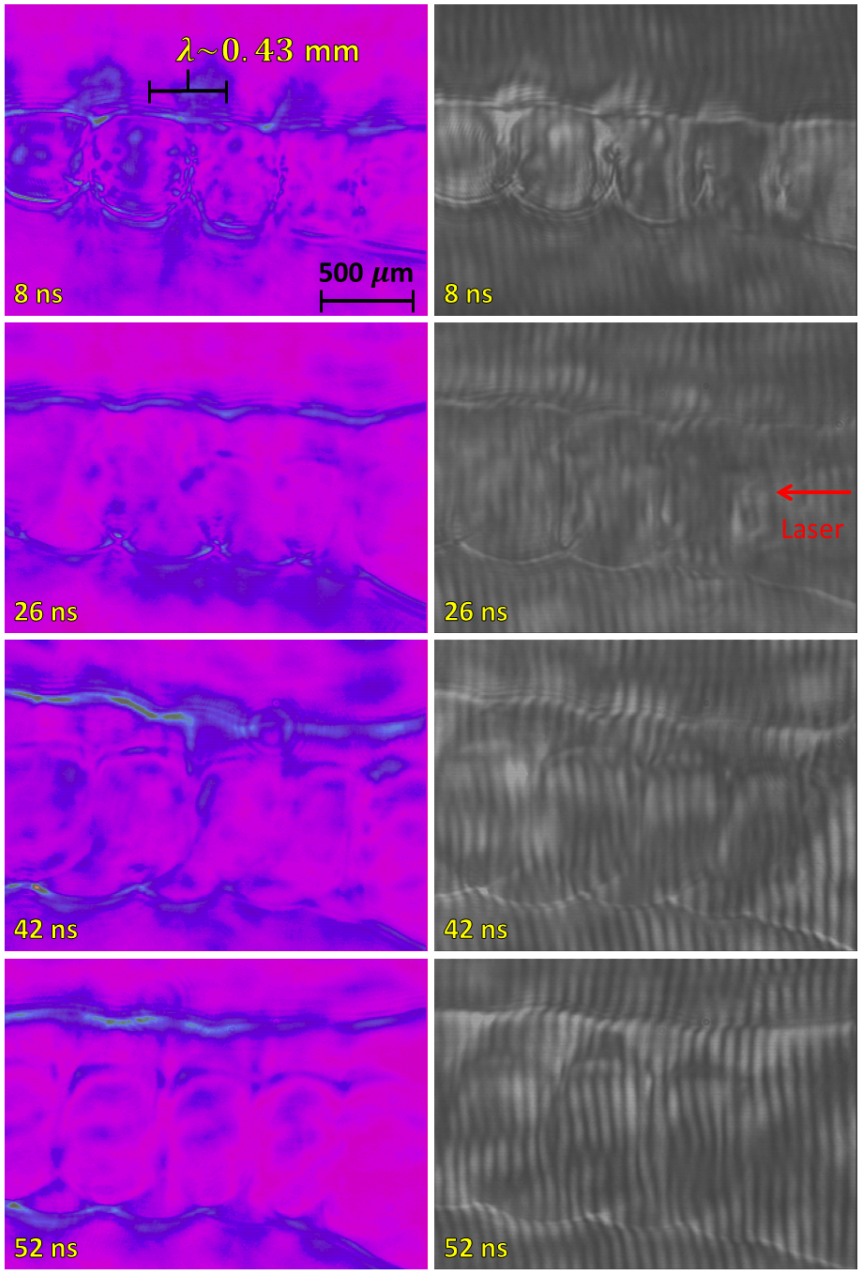

Figure 5.28: Schlieren and interferometric images of modulated blast waves in krypton produced with a backing pressure of 300 PSI and a 600 mJ laser pulse. The wavenumber of the modulation is $k = 14\,\mathrm{mm}^{-1}$.

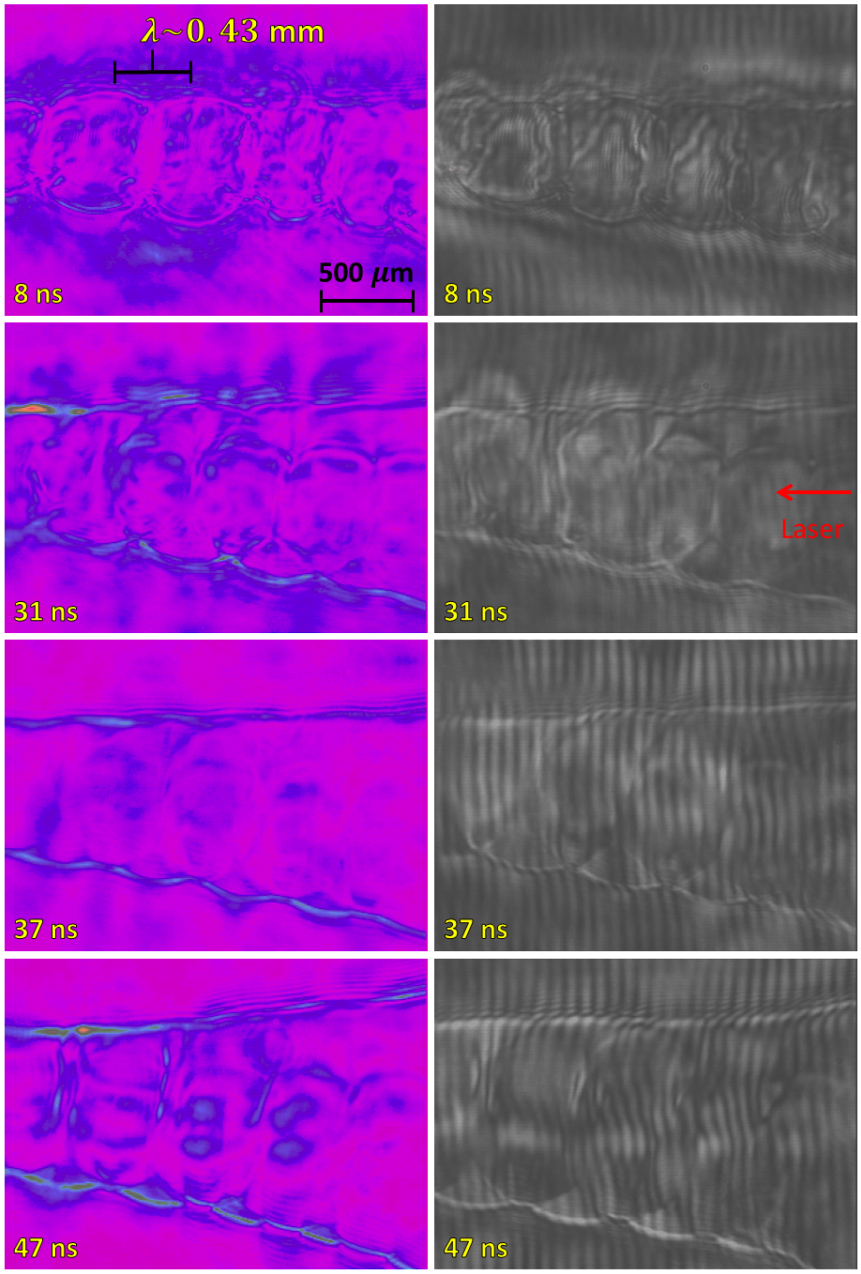

Figure 5.29: Schlieren and interferometric images of modulated blast waves in nitrogen produced with a backing pressure of 1000 PSI and a 600 mJ laser pulse. The wavenumber of the modulation is $k = 14\,\mathrm{mm}^{-1}$.

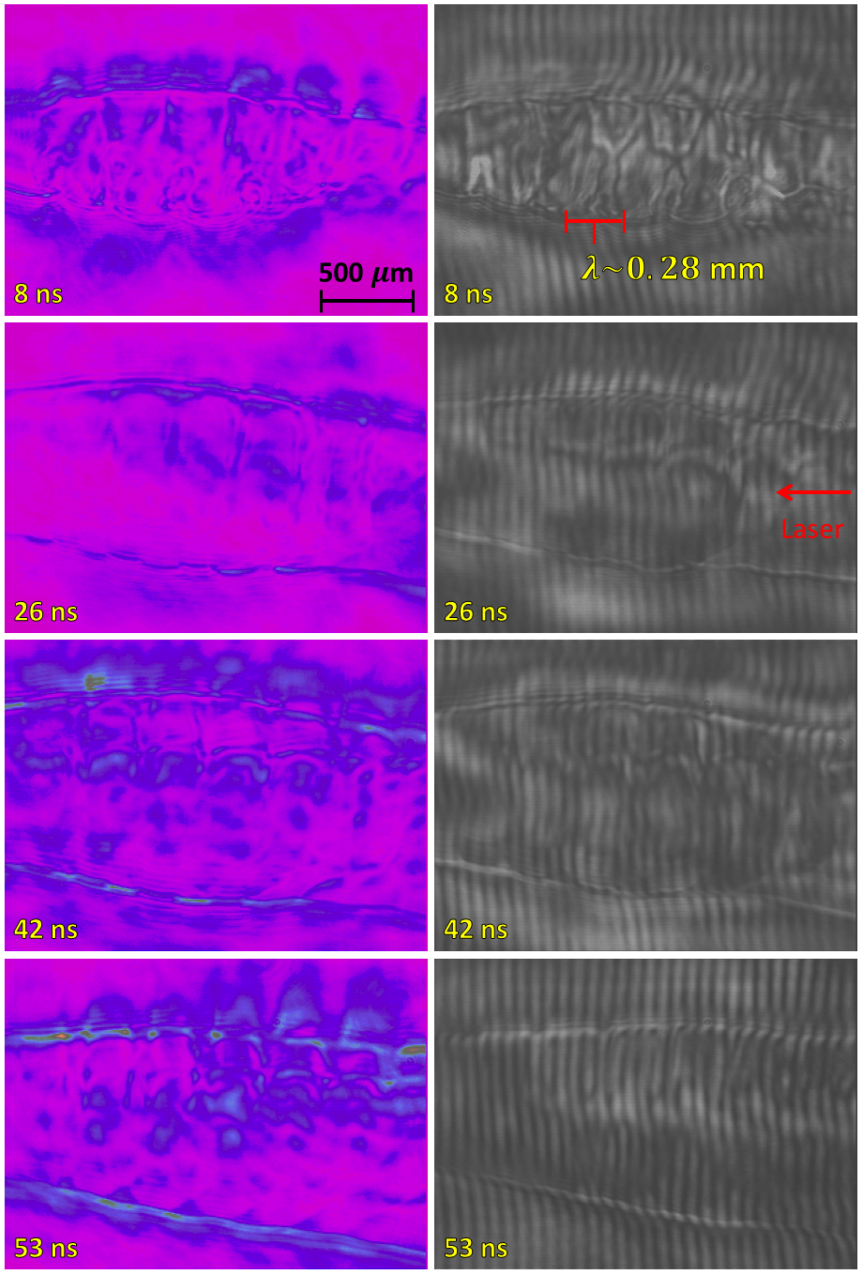

Figure 5.30: Schlieren and interferometric images of modulated blast waves in argon produced with a backing pressure of 800 PSI and a 600 mJ laser pulse. The wavenumber of the modulation is $k = 22\,\mathrm{mm}^{-1}$.

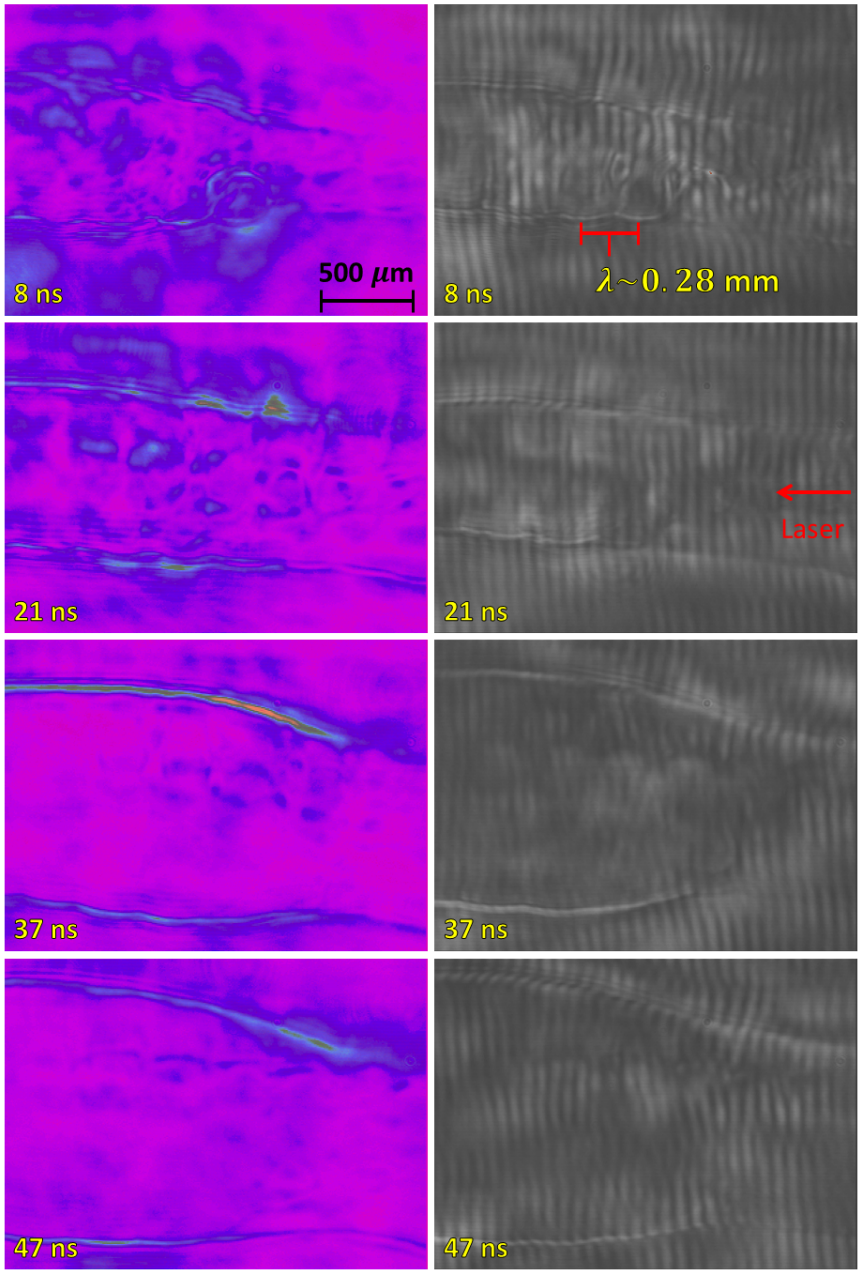

Figure 5.31: Schlieren and interferometric images of modulated blast waves in krypton produced with a backing pressure of 300 PSI and a 600 mJ laser pulse. The wavenumber of the modulation is $k = 22\,\mathrm{mm}^{-1}$.

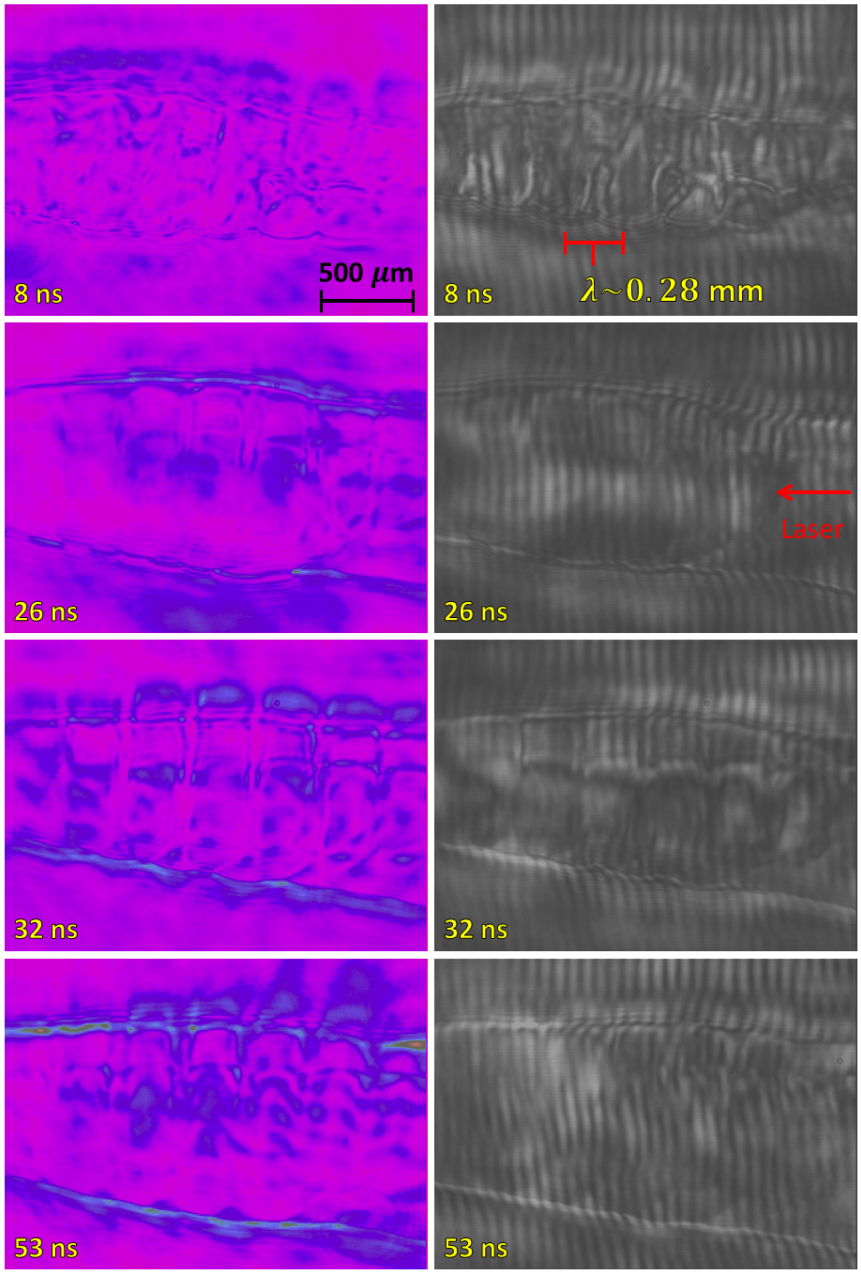

Figure 5.32: Schlieren and interferometric images of modulated blast waves in nitrogen produced with a backing pressure of 1000 PSI and a 600 mJ laser pulse. The wavenumber of the modulation is $k = 22\,\mathrm{mm}^{-1}$.

that delay. We calculated this radius by taking the mean radial displacement of the modulated blast wave surface. Analysis of longitudinal modulations

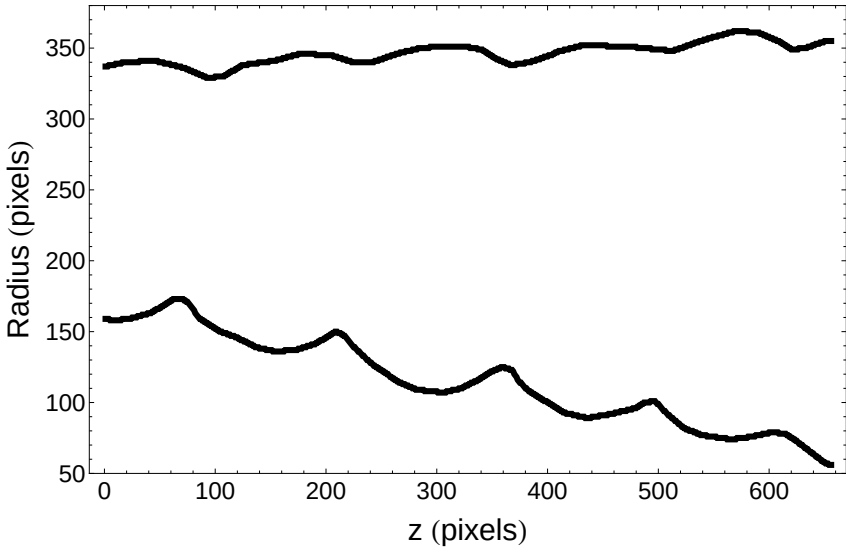

Figure 5.33: Sample plot of a blast wave surface. Shown is a trace performed on an argon blast wave at 26 ns with a modulation wavenumber of $k = 14$ mm^{-1}.

on a cylindrical blast wave differs from that of the spherical case since the wavelength of the perturbation remains constant throughout its evolution. In the spherical case, since the mode number l remains constant, the wavelength must grow as the blast wave expands. In that case, then, the analysis requires a simple power law fit $\sim t^s$ of the normalized perturbation amplitude where $s =$ constant. In our case, both k and the wavelength remains constant. It is more useful, then, to consider $s = s(r)$ for a given k value rather than the quantity $s = s(kr)$ as is plotted in Fig. (3.5).

We can compute $s = s(r)$ for all the k's considered in our experimental

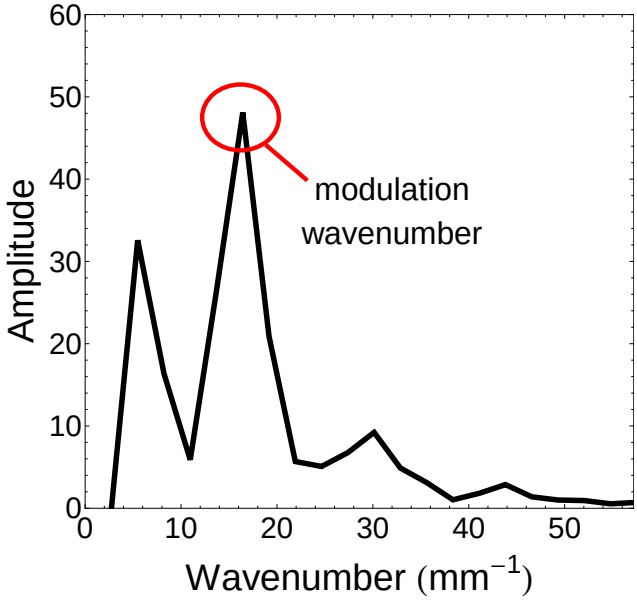

Figure 5.34: Sample Fourier transform of a modulated blast wave. The peak corresponds to the primary modulation wavenumber. This particular plot is from a krypton blast wave at 7 ns with a modulation wavenumber of $k = 17$ mm^{-1}.

data. Fig. (5.35) are plots of $s = s(r)$ for $k = 14$ mm^{-1} of the Vishiniac overstability model for various values of γ.

We can transform the plots shown in Fig. (5.35) from $s = s(r)$ to $s = s(t)$ by fitting the blast wave radius to a power law $R = At^{1/2}$ and use the fit parameter A to compute $t = A^2/R^2$ since this analysis assumes that the unperturbed component of the blast wave follows the classic Sedov-Taylor trajectory.

The normalized amplitudes of the perturbation is then fit to a function of the form $\sim t^{s(t)}$, where s is no longer just a constant. Here lies the

difference between analyzing longitudinal perturbations in cylindrical blast waves and those of spherical case. The normalized amplitudes for the various wavenmubers in argon, krypton, and nitrogen blast waves are plotted in Fig. (5.37)-(5.44) along with the curves fitted to the data for the effective polytropic index shown in Table (5.1).

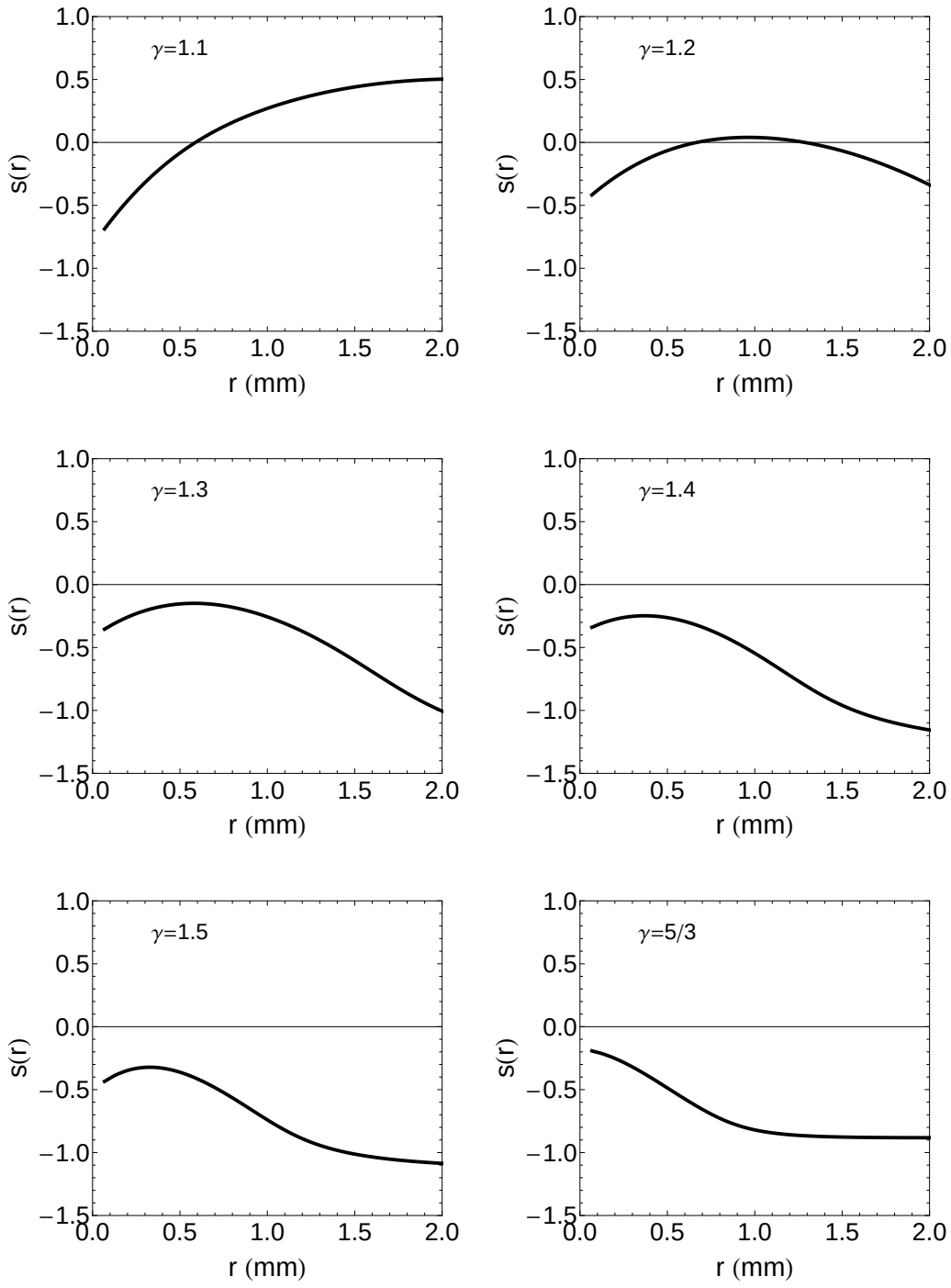

Figure 5.35: Plot of $s = s(r)$ for $k = 14$ mm^{-1} for various γ's.

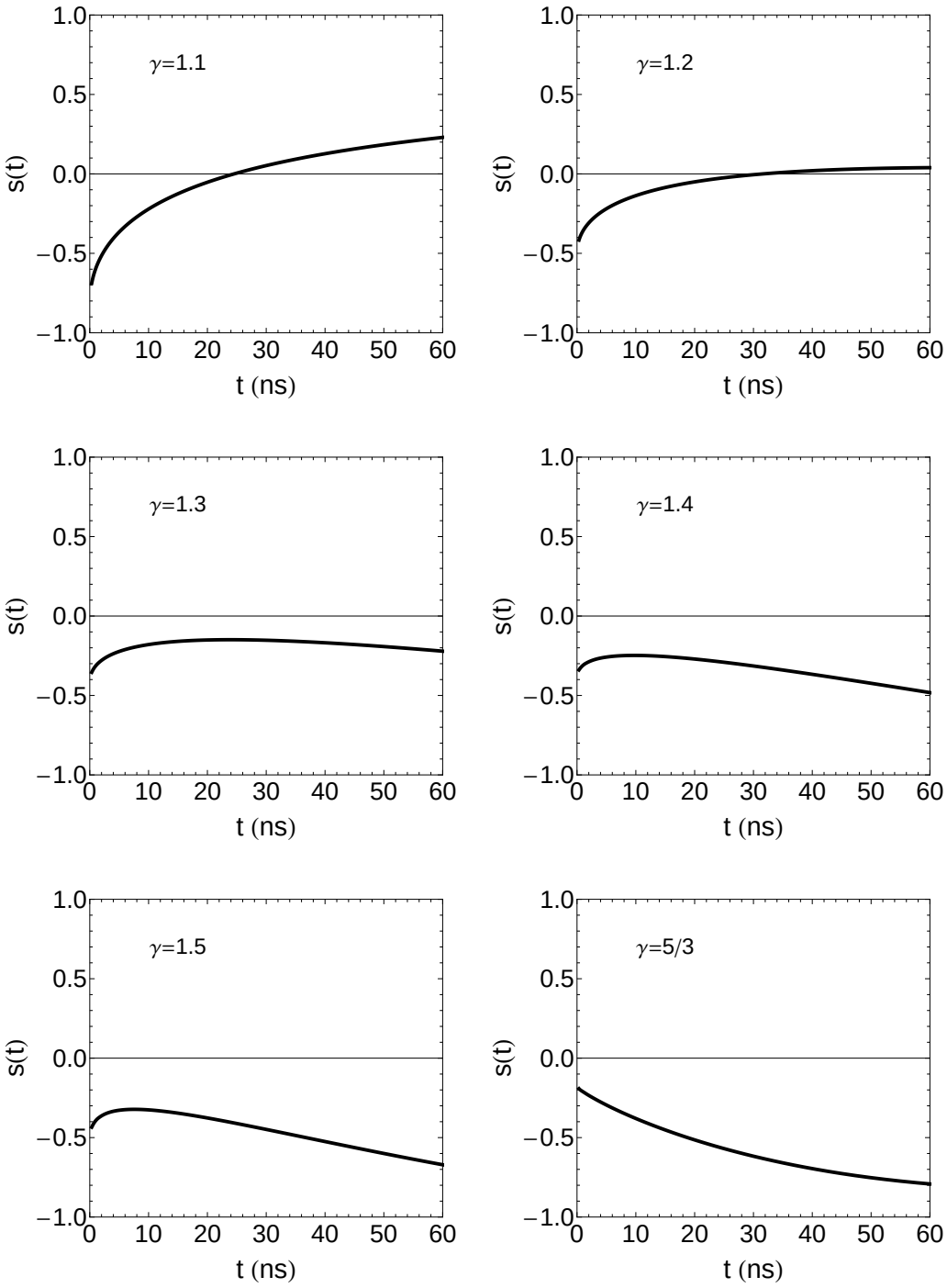

Figure 5.36: Plot of $s = s(t)$ for $k = 17$ mm^{-1} for various γ's.

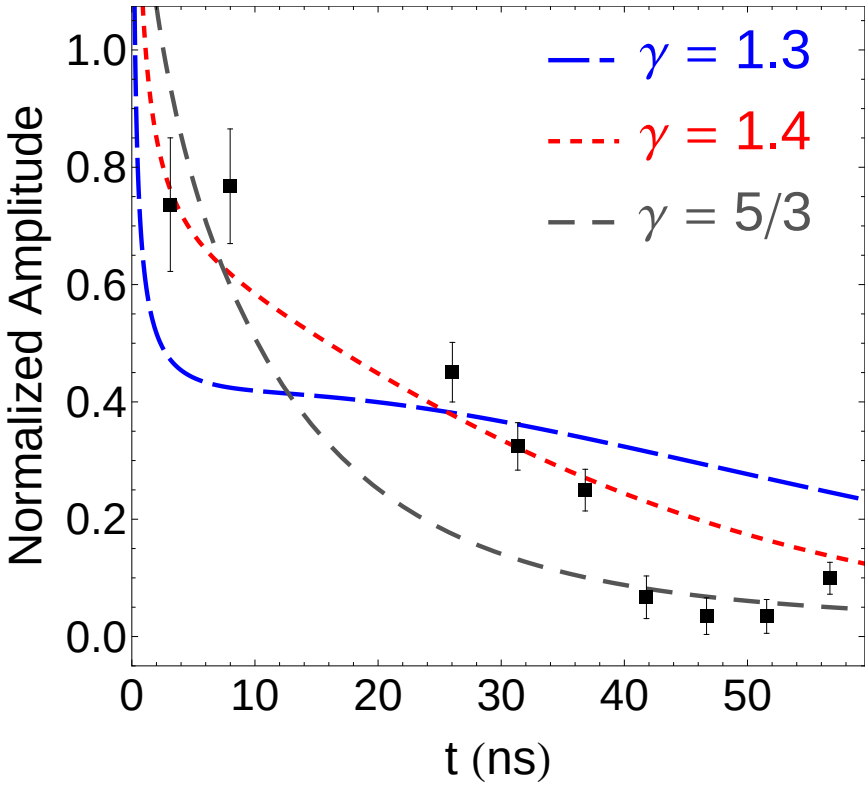

Figure 5.37: Plot of the normalized amplitude versus time for blast wave modulations with wavenumber $k = 14$ mm^{-1} in argon. Shown together are the functions of the form $\sim Bt^{s(t)}$ fit to the data for various γ's.

The results for argon for $k = 14$ mm^{-1}, shown in Fig. (5.37), suggest a polytropic index of $\gamma = 1.4$ at earlier times that eventually settles to a value of 5/3. The former is in agreement with calculations performed using the semiradiative model of blast waves and the experimentally observed trajectory under similar laboratory conditions discussed in Section 5.1. The latter value may be due to a decrease in the gas temperature as the blast wave expands and cools, eventually making radiation less important [26]. The polytropic index,

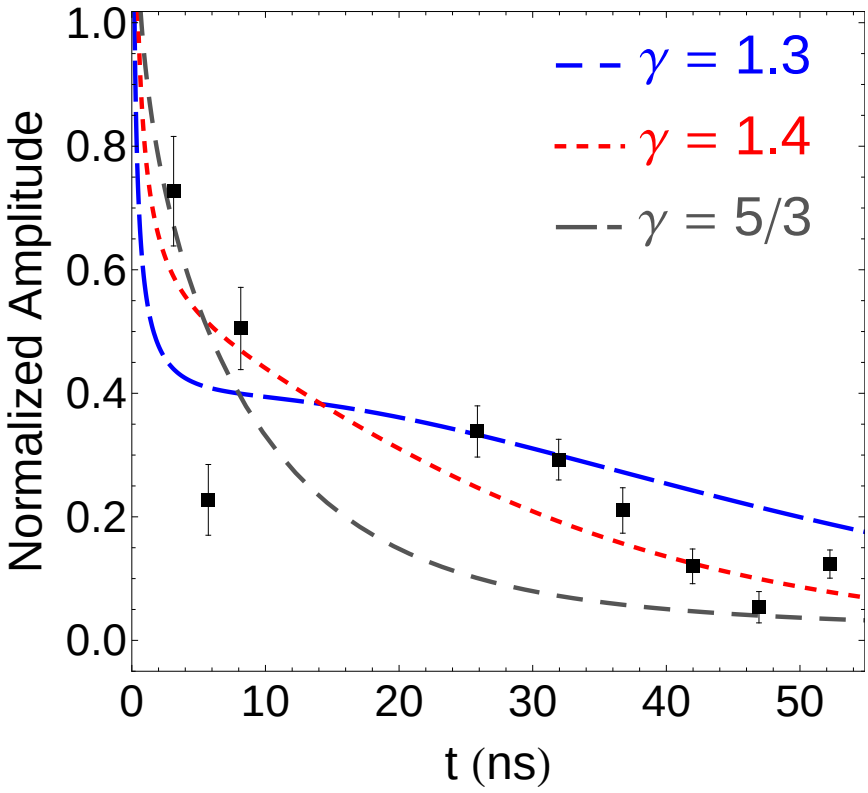

Figure 5.38: Plot of the normalized amplitude versus time for blast wave modulations with wavenumber $k = 17$ mm^{-1} in argon. Shown together are the functions of the form $\sim Bt^{s(t)}$ fit to the data for various γ's.

therefore, may not be the same throughout the blast wave evolution. With a wavenumber of $k = 17$ mm^{-1}, these blast waves exhibit a decay rate that implies a polytropic index in the range of 1.3 and 1.4. Shown in Fig. (5.38) are the data for the blast waves in argon with this particular modulation. Again, the amplitudes follow the curve for $\gamma = 1.3$ at earlier times eventually falling off and lying in between the curves for $\gamma = 1.3$ and 1.4. With the shorter wavelength perturbation of $k = 22$ mm^{-1}, the data matches very closely with

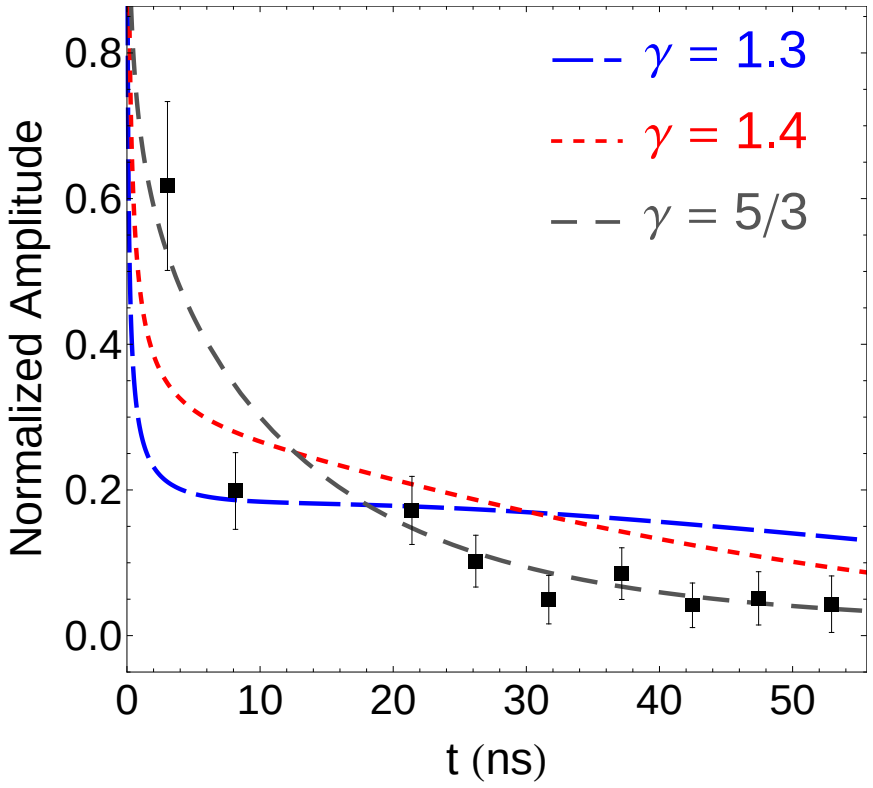

Figure 5.39: Plot of the normalized amplitude versus time for blast wave modulations with wavenumber $k = 22$ mm^{-1} in argon. Shown together are the functions of the form $\sim Bt^{s(t)}$ fit to the data for various γ's.

the curve for a polytropic index of $\gamma = 5/3$ suggesting an adiabatic or nearly adiabatic blast wave, a result that would be unlikely given the conditions of the experiment. One possible explanation for this behavior is that the shorter wavelength perturbations have been damped out too much during the blast wave's expansion thus making the analysis more difficult. In Ryu and Vishniac's theoretical analysis [23], the imaginary component of the temporal exponent describes the rate at which the perturbations oscillate with the higher

k's oscillating faster. It is possible that the high wavenumber perturbations has damped out enough from the faster oscillation rate.

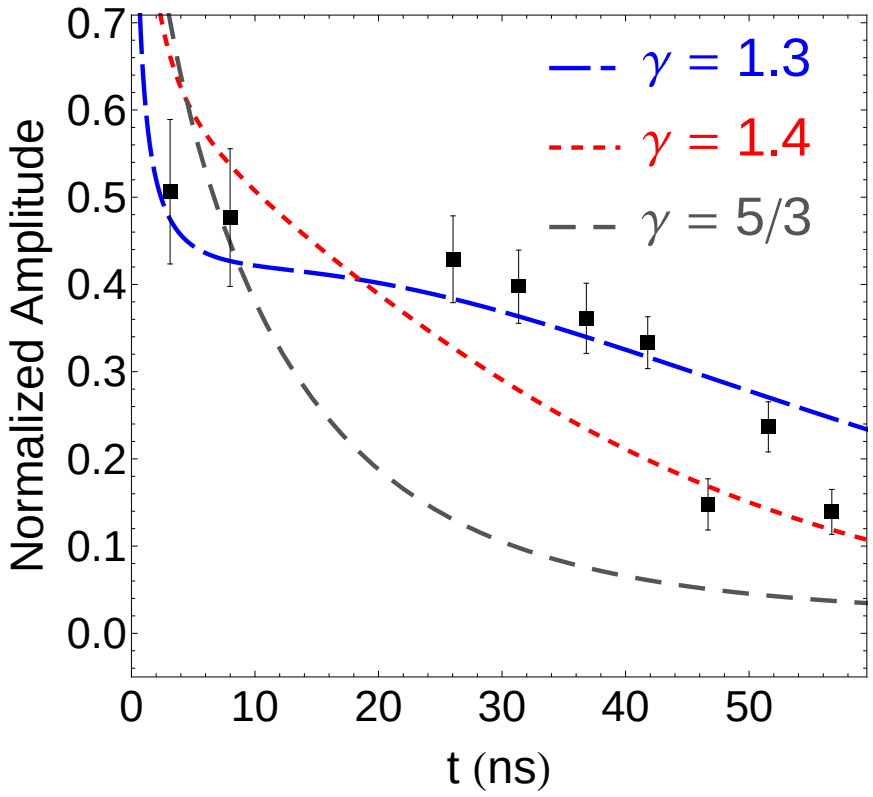

Figure 5.40: Plot of the normalized amplitude versus time for blast wave modulations with wavenumber $k = 14$ mm^{-1} in krypton. Shown together are the functions of the form $\sim Bt^{s(t)}$ fit to the data for various γ's.

The results for krypton blast waves with modulation wavenumbers $k =$ 14 and 17 mm^{-1} closely fits the curve for a polytropic index of $\gamma = 1.3$. Similar to the results in argon, Fig. (5.40) shows that for $k = 14$ mm^{-1}, the perturbation amplitudes on these blast waves initially decay consistent with polytropic index of $\gamma = 1.3$ until ~40 ns, after which the data points lie more

closely to the $\gamma = 1.4$ curve. As discussed perviously, this may be due to the blast wave experiencing less radiative losses at later times. Like argon, the

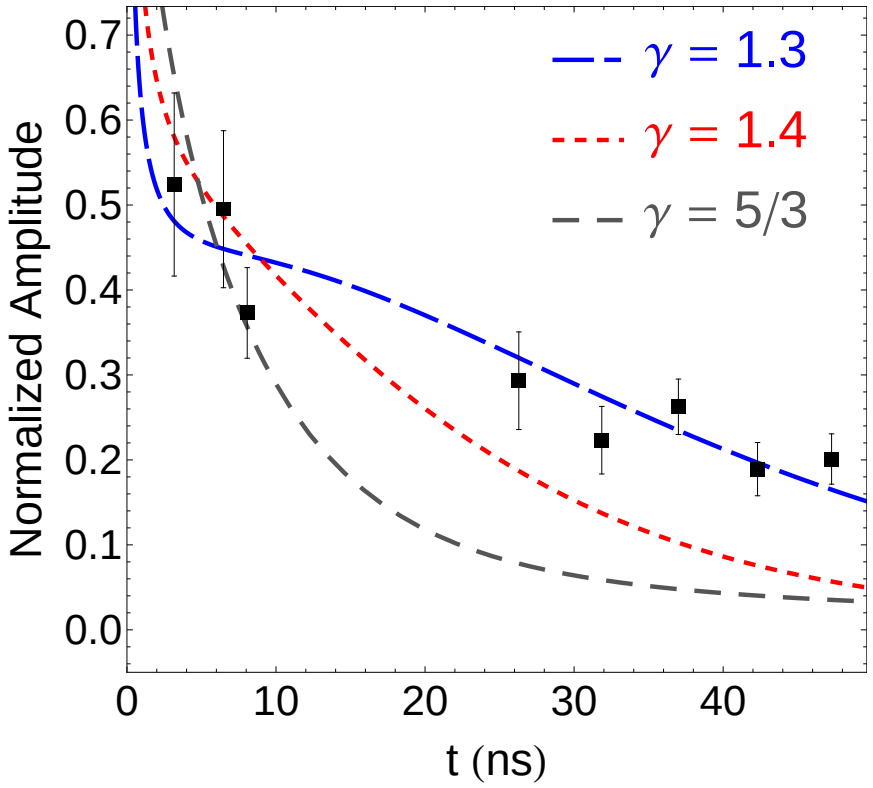

Figure 5.41: Plot of the normalized amplitude versus time for blast wave modulations with wavenumber $k = 17$ mm^{-1} in krypton. Shown together are the functions of the form $\sim Bt^{s(t)}$ fit to the data for various γ's.

data for $k = 22$ mm^{-1} in krypton seem to suggest that the short wavelength perturbations have largely damped out and follow closely with the curve for $\gamma = 5/3$ for most of the data points. Within error, however, are several points that do follow the curve for $\gamma = 1.3$.

Interpretation of the data from nitrogen was more complicated since we

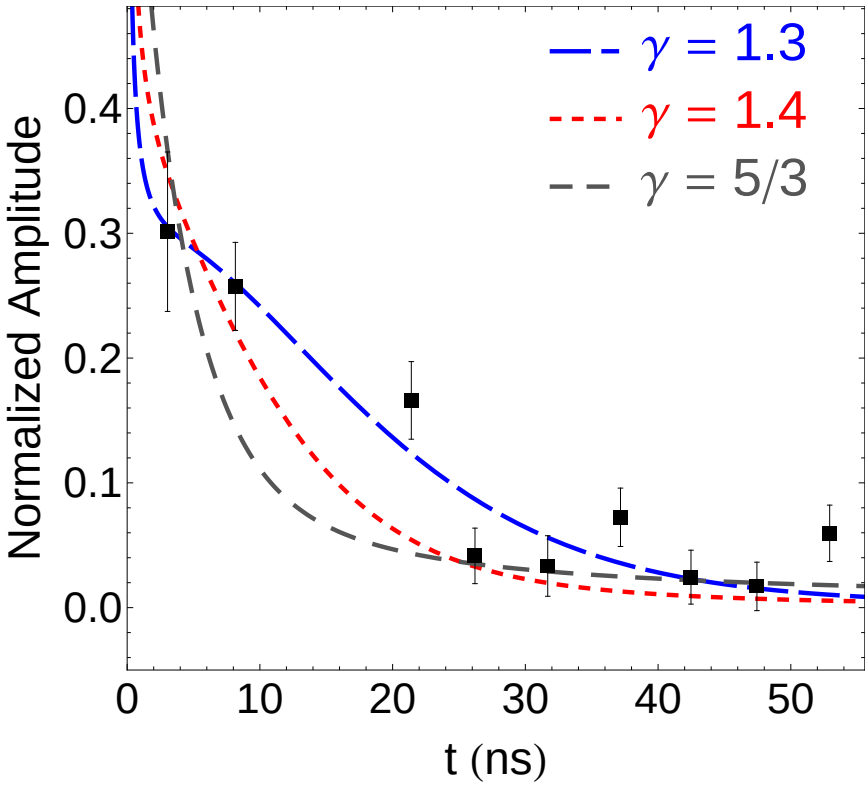

Figure 5.42: Plot of the normalized amplitude versus time for blast wave modulations with wavenumber $k = 22$ mm^{-1} in krypton. Shown together are the functions of the form $\sim Bt^{s(t)}$ fit to the data for various γ's.

did not have an experimentally derived value for the polytropic index unlike for argon and krypton. The $k = 14$ modulation wavenumber data follow the theoretical curves for $\gamma = 1.3$ and 1.4, the latter being the value for a purely adiabatic diatomic gas. For the high wavenumber of $k = 22$ mm^{-1}, the data follows most closely with the curve for $\gamma = 1.4$ (Fig. (5.44), consistent with that of an adiabatic blast wave traveling in a diatomic gas. This is unlikely the case and the high polytropic index value may be due to the same reasons

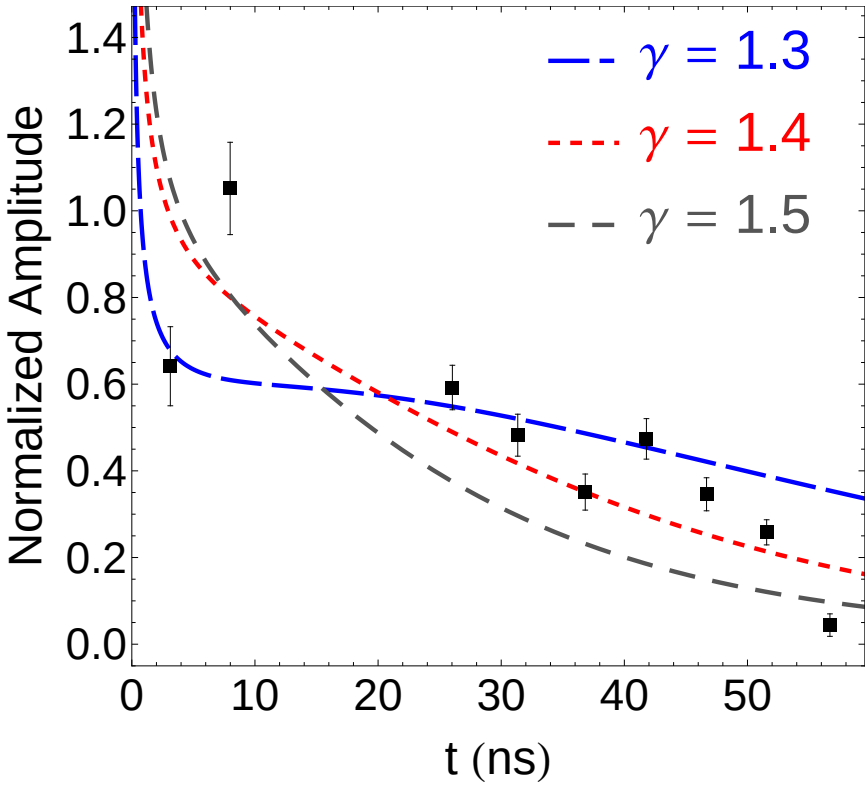

Figure 5.43: Plot of the normalized amplitude versus time for blast wave modulations with wavenumber $k = 14$ mm^{-1} in nitrogen. Shown together are the functions of the form $\sim Bt^{s(t)}$ fit to the data for various γ's.

as is for argon and krypton for this wavenumber.

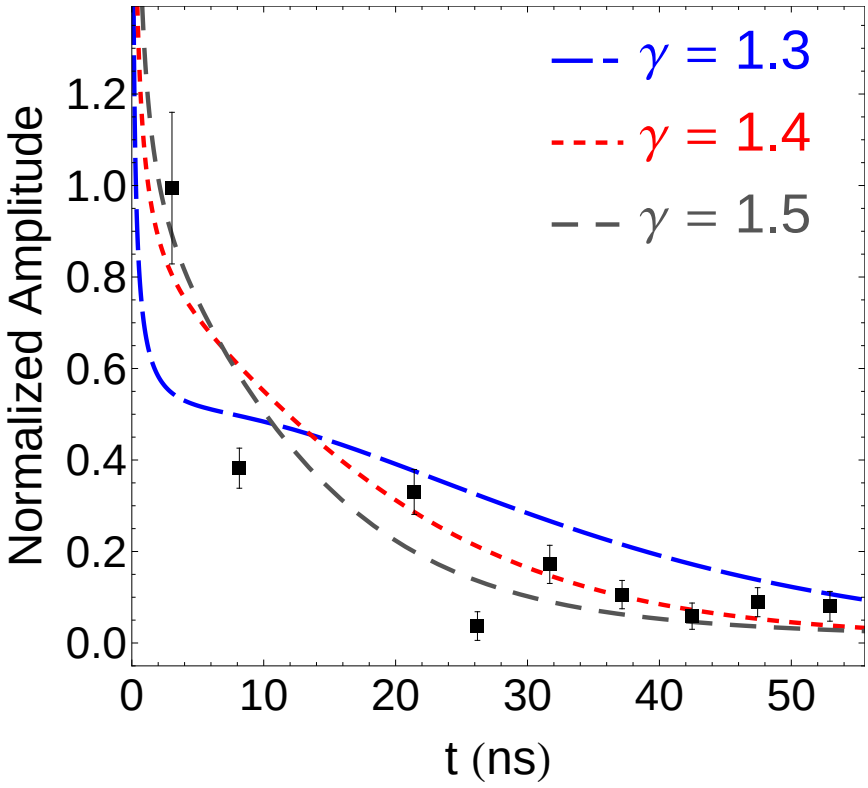

Figure 5.44: Plot of the normalized amplitude versus time for blast wave modulations with wavenumber $k = 22$ mm^{-1} in nitrogen. Shown together are the functions of the form $\sim Bt^{s(t)}$ fit to the data for various γ's.

5.6 Conclusions

The evolution a high Mach number blast wave is strongly affected by the amount of radiative losses it experiences as it expands. When a blast wave loses energy by radiation, its motion will be slower than that of its adiabatic counterpart and will expand will a lower deceleration parameter. We have shown that our blast waves are indeed radiative, first by measuring its trajectory and noting that its deceleration parameter is lower. The energy

lost by a strongly radiative blast wave is reabsorbed by the upstream medium and manifests itself in the form of a radiative precursor where the material upstream is ionized and is observed in the electron density measurements made by interferometric techniques. In addition, we have found that if the upstream material is not optically thin and certain conditions are met, the radiation from the blast wave will form a radiative heat wave that can ultimately give birth to a secondary shock ahead of the main shock front. This has been reported on previously in other experiments [44] and was observed in some of our experiments as well.

Lastly, radiative blast waves are important in experiments relating to astrophysical systems because of its susceptibility to hydrodynamic instabilities. As a blast wave experiences energy loss by radiation, its shock front becomes thinner and more compressible, ultimately leading to unstable behavior. In particular, we performed experiments to observe the time evolution of perturbations induced on the blast wave surface and compared it to theory proposed by Vihsniac et al. [23]. The evolution of these perturbations are largely affected by the polytropic index of the gas and the wavelength of the perturbation. In our experiments, we have shown evidence of the decay in the perturbation amplitudes and compared it to theory. Our results show that a single polytropic index is not applicable to the entire duration of the blast wave's motion. A blast wave may be radiative in at earlier times but may experience a higher effective polytropic index as it expands and cools.

Chapter 6

Conclusion

6.1 Summary

The primary objective of this work has been to produce strongly radiating blast waves as it relates to astrophysical phenomena. Specifically, our experiments centered around the behavior of hydrodynamic instabilities and its possible contribution to stellar formation. We achieved this by producing blast waves using cluster gas sources and modifying the medium prior to the onset of the main heating pulse. By destroying clusters at periodic locations with a second beam beforehand, the main heating beam is variably absorbed by the clusters and consequently a modulation is imprinted in the subsequent blast wave.

By tracking the modulations on the blast wave surface, we were able to make comparisons of these perturbations to that of accepted astrophysical theory. Our results show that the amplitudes decay within agreement with theory for the different gases and for the different modulation frequency. Our results show that the evolution of these perturbations, however, are not consistent by a single polytropic index throughout its lifetime but varies. In the early radiative phase, a blast wave undergoes energy loss by radiation. Eventually,

though, the blast wave may recover some of this energy from the upstream preheated ionized material as it expands. We have observed this to be the case in our analysis of the perturbations.

6.2 Future Work

There are many ways this work can be extended by future efforts. I will discuss three specific possible directions.

6.2.1 Diagnostics

Our primary diagnostics in this work were schlieren or interferometric images. To adequately study these blast waves require images at various time delays. We achieved this by use of a probe beam that was delayed relative to the main pulse by means of an optical rail. Since the time frame we are interested in are in the 10's to 100's of nanoseconds and limited physically by laboratory space, we employed multipass delay stages to accomodate our needs. One possible way to bypass this limiation is through electronic means using a pockel cell and an optical cavity where a probe beam can pass back and forth until the beam is desired for use as a probe. This method would allow for precise electronic timing of the probe pulse and many more images at the desired delays.

Another improvement in tracking the blast wave would be to use a streak camera that can continuously record its motion. This method, used in a previous experiment [51], would allow the possibility to observe the os-

cillatory nature of the Vishniac overstability mechanism. The drawbacks to this, however, are that a streak camera only provides one spatial dimension for observation and requires a probe beam that is intense and long enough to be recorded.

6.2.2 Secondary Shock Formation

A detailed investigation of the secondary shock formation in strongly radiative blast waves is another direction. We observed this in experiments with krypton but was limited to a localized region. Our numerical simulations hints at this phenomena being sensitive to the local gas density. This work can be extended by examining other high Z cluster sources and different backing pressures to observe any trends in the formation of this secondary shock.

6.2.3 Instability Growth and Different Wavenumbers

Further experiments on the Vishiniac overstability can be extended to include more wavenumbers and various other high Z gases. The behavior of these instabilities are mainly affected by the polytropic index of the gas and the wavelength of the particular perturbation. Exploring more modulation frequencies and using other high Z gases would be an effective way to investigate futher the Vishniac mechanism.

References

[1] H. Takabe, "Astrophysics with Intense and Ultra-Intense Lasers," Progress of Theoretical Physics Supplement **143**, 202 (2001)

[2] D. Ryutov, R. P. Drake, J. Kane, E. Liang, L. A. Remington, and W. M. Wood-Vasey, "Similarity Criteria for the Laboratory Simulation of Supernova Hydrodynamics," The Astrophysical Journal **518**, 821 (1999)

[3] D. Strickland and G. Mourou, "Compression of Amplified Chirped Optical Pusles," Optics Communications **56**, 3 (1985)

[4] R. P. Drake, *High-Energy-Density Physics, Fundamentals, Inertial Fusion, and Experimental Astrophysics*. Berlin, Germany: Springer-Verlag Berlin (2006)

[5] Ya. B. Zel'dovich and' Yu. P.Raizer, *Physics of Shock Waves and High-Temperature Hydrodynamic Phenomena*. Mineola, New York: Dover Publications, Inc., (2002).

[6] L. E. Reichl, *A Modern Course in Statistical Physics*. 2nd Edition. New York, New York: John Wiley and Sons, Inc. (1998)

[7] L. D. Landau and E. M. Lifshitz, *Fluid Mechanics*. New York: Academic Press (1966)

[8] C. F. McKee and J. P. Ostriker, "A Theory of the Interstellar Medium: Three Components Regulated by Supernova Explosions in an Inhomogeneous Substrate," The Astrophysical Journal **218**, 148 (1977)

[9] D. F. Cioffi, C. F. McKee, E. Bertshinger, "Dynamics of Radiative Supernova Remnants," The Astrophysical Journal **334**, 252 (1988)

[10] E. Liang and K. Keilty, "An Analytic Approximation to Radiative Blast Wave Evolution," The Astrophysical Journal **533**, 890 (2000)

[11] K. A. Keilty, E. P. Liang, T. Ditmire, B. A. Remington, K. Shigemori, and A. M. Rubenchik, "Modeling of Laser-Generated Radiative Blast Waves," The Astrophysical Journal **538**, 645 (2000)

[12] E. Cohen, T. Piran, and R. Sari, "Fluid Dynamics of Semiradiative Blast Waves," The Astrophysical Journal **509**, 717 (1998)

[13] L. D. Landau and E. M. Lifshitz, *The Classical Theory of Fields* Reading, Massachusetts: Addison-Wesley, (1962)

[14] T. Ditmire, K. Shigemori, B. A. Remington, K. Estabrook, and R. A. Smith, "The Production of Strong Blast Waves Through Intense Laser Irradiation of Atomic Cluster," The Astrophysical Journal Supplement Series **127**, 299 (2000)

[15] R. A. Chevalier, "The Interaction of Supernova with the Interstellar Medium," Annual Review of Astronomy and Astrophysics **15**, 175 (1977)

[16] R. S. Sutherland and M. A. Dopita, "Cooling Functions For Low-Density Astrophysical Plasmas," The Astrophysical Journal Supplement Series **88**, 253 (1993)

[17] U. Hwang, R. Petre, and J. P. Hughes, "The X-Ray Line Emission from the Supernova Remnant W49B," The Astrophysical Journal, **532**, 970 (2000)

[18] K. J. Borkowski, J. M. Blondin, and R. McCray, "X-Rays from the Impact of SN 1987A with its Circumstellar Ring," The Astrophysical Journal **477**, 281 (1997)

[19] J. P. Ostriker and L. L. Cowie, "Galaxy Formation in an Intergalactic Medium Dominated by Explosions," The Astrophysical Journal **243**, L127 (1981)

[20] L. I. Sedov, *Similarity and Dimensional Methods in Mechanics*. 10th Edition. Boca Raton, FL: CRC Press, Inc. (1993)

[21] E. T. Vishniac, "The Dynamic and Gravitational Instabilities of Spherical Shocks," The Astrophysical Journal **274**, 152

[22] M.-M. MacLow and M. L. Norman, "Nonlinear Growth of Dynamical Overstabilities in Blast Waves," The Astrophysical Journal **407**, 207 (1993)

[23] E. Ryu and E. T. Vishniac, "The Growth of Linear Perturbations of Adiabatic Shock Waves," The Astrophysical Journal **313**, 820 (1987)

[24] D. Ryutov, T. Ditmire, J. Edwards, G. Glendinning, B. Remington, K. Shigemori, "Simple Theory of a Blast Wave for Gases with the Adiabatic Index Close to one" 41st Annual Meeting of the American Physical Society, Seattle, Washington, November 18 1999

[25] J. Grun, J. Stamper, C. Manka, J. Resnick, R. Burris, J. Crawford, and B. H. Ripin, "Instabiliy of Taylor-Sedov Blast Waves Propagating through a Uniform Gas," Physical Review Letters **66** 2738 (1991)

[26] A. D. Edens, *Experimental Study of the Hydrodynamics of High Mach Number Blast Waves*. Ph.D. Thesis. The Univeristy of Texas at Austin, TX (2005)

[27] A. D. Edens, T. Ditmire, J. F. Hansen, M. J. Edwards, R. G. Adams, P. Rambo, L. Ruggles, I. C. Smith, and J. L. Porter, "Study of high Mach Number Laser Driven Blast Waves," Physics of Plasmas **11**, 11 (2004)

[28] A. D. Edens, T. Ditmire, J. F. Hansen, M. J. Hansen, M. J. Edwards, R. G. Adams, P. K. Rambo, L. Ruggles, I. C. Smith, and J. L. Porter, "Measurement of the Decay Rate of Single-Frequency Perturbations on Blast Waves," Physical Review Letters **95**, 244503 (2005)

[29] R. W. Boyd, *Nonlinear Optics*. 2nd Edition San Diego, CA: Academic Press (2003)

[30] J. Osterhoff, D. R. Symes, A. D. Edens, and T. Ditmire, "Ultra High Intensity Laser Launched Radiative Shock Waves Related to Supernova

Remnant Formation," Quantum Electronics and Laser Science Conference (2005)

[31] T. Ditmire, T. Donnelly, A. M. Rubenchik, R. W. Falcone, and M. D. Perry, "Interaction of Intense Laser Pulses with Atomic Clusters," Physical Review A **53**, 3379 (1996)

[32] T. Ditmire, R. A. Smith, J. W. G. Tisch, and M. H. R. Hutchinson, "High Intensity Laser Absorption by Gases of Atomic Clusters," Physical Review Letters **78**, 3121 (1997)

[33] T. Ditmire, E. Springate, J. W. Tisch, Y. L Shao, M. B. Mason, N. Hay, J. P Marangos, and M. H. R. Hutchinson, "Explosion of Atomic Clusters Heated by High-Intensity Femtosecond Laser Pulses," Physical Review A **57**, 369 (1998)

[34] O. F. Hagena and W. Obert, "Cluster Formation in Expanding Supersonic Jets: Effect of Pressure, Temperature, Nozzle Size, and Test Gas," The Journal of Chemical Physics **56**, 1793 (1972)

[35] F. Dorchies, F. Blasco, T. Caillaud, J. Stevefelt, C. Stenz, A. S. Boldarev, and V. A. Gasilov, "Spatial Distribution of Cluster Size and Density in Supersonic Jets as Targets for Intense Laser Pulses," Physical Review A **68**, 023201 (2003)

[36] R. A. Smith, T. Ditmire, and J. W. G. Tisch, "Characterization of a

Cryogenically Cooled High-Pressure Gas Jet for Laser/Cluster Interaction Experiments," Review of Scientific Instruments **69**, 3798 (1998)

[37] I. H. Hutchinson, *Principles of Plasma Diagnostics*. 2nd Edition. Cambridge, UK: Cambridge University Press (2002)

[38] M. Takeda, H. Ina, and S. Kobayashi, "Fourier-Transform Method of Fringe-Pattern Analysis for Computer-Based Topography and Interferometry," Journal of the Optical Society of America **72** 156 (1982)

[39] K. Shigemori, T. Ditmire, B. A. Remington, V. Yanovsky, D. Ryutov, K. G. Estabrook, M. J. Edwards, A. J. MacKinnon, A. M. Rubenchik, K. A. Keilty, and E. Liang, "Developing a Radiative Shock Experiment Relevant to Astrophysics," The Astrophysical Journal **533**, L159 (2000)

[40] T. Ditmire, K. Shigemori, B. A. Remington, K. Estabrook, and R. A. Smith, "The Production of Strong Blast Waves Through Intense Laser Irradiation of Atomic Clusters," The Astrophysical Journal Supplement Series **127**, 299 (2000)

[41] M. J. Edwards, A. J. MacKinnon, J. Zweiback, K. Shigemori, D. Ryutov, A. M. Rubenchik, K. A. Keilty, E. Liang, B. A. Remington, and T. Ditmire, "Investigation of Ultrafast Laser-Driven Radiative Blast Waves," Physical Review Letters **87**, 085004 (2001)

[42] J. Zweiback and T. Ditmire, "Femtosecond Laser Energy Deposition in

Strongly Absorbing Cluster Gases Diagnosed by Blast Wave Trajectory Analysis," Physics of Plasmas **8**, 4545 (2001)

[43] A. S. Moore, J. Lazarus, M. Hohenberger, j. S. Roinson, E. T. Grumbrell, M. Dunne, and R. A. Smith, "Investigating the Astrophysical Applicability of Radiative and Non-Radiative Blast Wave Structure in Cluster Media," Astrophysics and Space Science **307**, 139 (2007)

[44] J. F. Hansen, M. J. Edwards, D. H. Froula, G. Gregori, A. D. Edens, and T. Ditmire, "Laboratory Observation of Secondary Shock Formation Ahead of a Strongly Radiative Blast Wave," Physics of Plasmas **13**, 022105 (2006)

[45] J. F. Hansen, M. J. Edwards, D. H. Froula, A. D. Edens, G. Gregori, and T. Ditmire, "Secondary Shock Formation in Xenon-Nitrogen Mixtures," Physics of Plasmas **13**, 11201 (2006)

[46] G. I. Barenblatt, *Similarity, Self-Similarity and Intermediate Asymptotics*, New York, NY: Consultants Bureau (1979)

[47] P. Reinicke and J. Meyer-ter-Vehn, "The Point Explosion with Heat Conduction," Physics of Fluids A **3**, 1807 (1991)

[48] R. Rodriquez, J. M. Gil, G. Espinosa, R. Florido, J. G. Rubiano, M. A. Mendoza, P. Martel, E. Minguez, D. R. Symes, M. Hohenberger, and R. A. Smith, "Determination and Analysis of Plasma Parameters for Sim-

ulations of Radiative Blast Waves Launched in Clusters of Xenon and Krypton," Plasma Physics and Controlled Fusion **54**, 045012 (2012)

[49] D. R. Symes, A. J. Comley, J. W. G. Tisch, and R. A. Smith, "Modification of Laser Energy Deposition in a Gas of Deuterium Clusters," Applied Physics Letters **80**, 4112 (2002)

[50] A. S. moore, D. R. Symes, and R. A. Smith, "Tailored Blast Wave Formation: Developing Experiments Pertinent to Laboratory Astrophysics," Physics of Plasmas **12**, 052707 (2005)

[51] A. S. moore, E. T. Gumbrell, J. Lazarus, M. Hohenberger, J. S. Robinson, R. A. Smith, T. J. A. Plant, D. R. Symes, and M. Dunne, "Full-Trajectory Diagnosis of Laser-Driven Radiative Blast Waves in Search of Thermal Plasma Instabilities," Physical Review Letters **100**, 055001 (2008)